NTNU

Norwegian University of
Science and Technology

Numerical Modelling of Debris Flow Hazards using Computational Fluid Dynamics

Bradley Clark

Geotechnics and Geohazards
Submission date: June 2018
Supervisor: Vikas Kumar Singh Thakur, IBM
Co-supervisor: Petter Fornes, IBM

Norwegian University of Science and Technology
Department of Civil and Environmental Engineering

NORWEGIAN UNIVERSITY OF SCIENCE AND TECHNOLOGY
DEPARTMENT OF CIVIL AND TRANSPORT ENGINEERING

Report Title:	Date: **11.06.2018**	
Numerical Modelling of Debris Flow Hazards using Computational Fluid Dynamics	Number of pages (incl. appendices): **157**	
	Master Thesis	x
Name: Bradley Clark		
Professor in charge/supervisor: Vikas Thakur, IBM		
Other external professional contacts/supervisors: Petter Fornes, IBM/NGI		

Abstract:
Debris flows are a natural hazard phenomenon that occur periodically in steep mountainous terrain and are typically triggered by heavy precipitation events. The flows are a highly mobile poorly graded mass of soil, rock, water, and debris and are a major risk to infrastructure and human life. The ability to model the behaviour and to predict event inundation and severity are critical to understanding the impact of debris flows. Currently, empirical relationships and depth-averaged numerical models help govern mitigation design, but continued computational developments are making it less and less time consuming to model these events in three dimensions and in full physical detail.

The use of computational fluid dynamics (CFD) can help capture detailed flow dynamics and full 3-dimensional debris flow inundation behaviour. The open-source CFD code REEF3D was used to back analyze laboratory flume tests to validate the use of CFD and non-Newtonian fluid rheologies to model debris flows. A sensitivity analysis of the flume components was performed to analyze the flume geometry and its effects on flow behaviour. Channel width reduction in the confined portion of the flume, the cylindrical pillar in the flow path, and the unconfined deposition area all had a significant influence on the flow simulation. A low yield stress was required to reproduce the liquefied behaviour of the flume testing material pre-release. Final calibration showed a good match using the Bingham rheology model, but unlike the flume model, the numerical model did not show a single surge of all the material. Instead a thin layer of material flowed at a slower rate along the slope interface – which appears to be a limitation within numerical model. The use of CFD and non-Newtonian fluid rheologies is a promising development for modelling the detailed behaviour of debris flow hazards.

Keywords:

1. Debris Flow
2. Numerical Modelling
3. CFD
4. Non-Newtonian Rheology
5. REEF3D

NTNU
Faculty of Engineering Science and Technology
Institute of Civil and Environmental Engineering

MASTER'S DEGREE THESIS

Spring 2018
for

Student: Bradley Clark

Numerical Modelling of Debris Flow Hazards using Computational Fluid Dynamics

BACKGROUND

Debris flow hazards are a periodic and destructive process that effect communities and infrastructure in mountainous regions worldwide. The ability to model the behaviour and impact of debris flows and to predict event inundation and severity are critical to building safe infrastructure that will minimize risk to human life. Traditionally, empirical formulations and depth-averaged numerical models have been used to predict velocity and runout to help guide design. Presently, modern computational infrastructure allows for the opportunity to model the detailed flow dynamics and full 3-dimensional inundation behaviour by using computational fluid dynamics (CFD).

TASK

Use the CFD code REEF3D to model experimental flume testing performed at NTNU in 2017 using non-Newtonian fluid rheologies.

TASK DESCRIPTION

Laboratory flume testing was performed in 2017 at NTNU. Instrumentation was used to measure the progression of flow thickness and pillar forces during testing. Flow runout length was measured after each test and impact velocity was found based on video records. The REEF3D code will be used to calibrate the experimental data to a numerical model using the Herschel-Bulkley and/or Bingham rheologies. REEF3D is an open-source CFD code currently in development at NTNU by the Marine Civil Engineering group. The software solves the Navier-Stokes equations in three-dimensions.

SUBTASKS

- Perform a literature review on debris flow hazards.
- Desk study of some selected flume tests to simulate the mobility of debris flows performed at NTNU in 2017.
- Investigate the applicability of non-Newtonian fluid rheologies on the mobility of debris flows.
- Describe the CFD code REEF3D that will be used to model debris flow testing.
- Conduct a sensitivity analysis on material properties and individual flume components to test how they influence flow behaviour and results.

PROFESSOR IN CHARGE:

Vikas Thakur

ABSTRACT

Debris flows are a natural hazard phenomenon that occur periodically in steep mountainous terrain and are typically triggered by heavy precipitation events. The flows are a highly mobile poorly graded mass of soil, rock, water, and debris and are a major risk to infrastructure and human life. The ability to model the behaviour and to predict event inundation and severity are critical to understanding the impact of debris flows. Currently, empirical relationships and depth-averaged numerical models help govern mitigation design, but continued computational developments are making it less and less time consuming to model these events in three dimensions and in full physical detail.

The use of computational fluid dynamics (CFD) can help capture detailed flow dynamics and full 3-dimensional debris flow inundation behaviour. The open-source CFD code REEF3D was used to back analyze laboratory flume tests to validate the use of CFD and non-Newtonian fluid rheologies to model debris flows. A sensitivity analysis of the flume components was performed to analyze the flume geometry and its effects on flow behaviour. Channel width reduction in the confined portion of the flume, the cylindrical pillar in the flow path, and the unconfined deposition area all had a significant influence on the flow simulation. A low yield stress was required to reproduce the liquefied behaviour of the flume testing material pre-release. Final calibration showed a good match using the Bingham rheology model, but unlike the flume model, the numerical model did not show a single surge of all the material. Instead a thin layer of material flowed at a slower rate along the slope interface – which appears to be a limitation within numerical model. The use of CFD and non-Newtonian fluid rheologies is a promising development for modelling the detailed behaviour of debris flow hazards.

PREFACE

This thesis is submitted in partial fulfillment of the requirement for a Master's Degree (MSc) in Geotechnics and Geohazards at the department of Civil and Transport Engineering, Norwegian University of Science and Technology (NTNU). It was carried out in the spring semester of 2018.

I would like to thank Vikas Thakur for taking me on and helping me find a project that was tailored to my interests. Special thanks to Petter Fornes for all the guidance and help with the numerical modelling, and the feedback on the results and reporting. Thanks to Arun Kamath for the help troubleshooting in REEF3D.

I am thankful for the support from my family and friends during my time at NTNU. Special thanks to my wife for flying across the world with me to help take this challenge on – and to Henrik for taking it easy on me after long days.

CONTENTS

LIST OF FIGURES

LIST OF TABLES

LIST OF SYMBOLS

A	Area of erodible material (channel)	V	Final debris flow magnitude
c	Cohesion	$V_{initial}$	Initial failure mass magnitude
C_s	Solids concentration	V_{point}	Point mass magnitude
C_u	Coefficient of Uniformity	w	Water content
d	Flow thickness	x, y, z	Cartesian coordinate system
f	Friction coefficient	Y	Channel debris yield rate
F_{MAX}	Maximum impact force	β	Slope angle
F_{pillar}	Pillar force	$\dot{\gamma}$	Shear rate
g	Gravitational constant	η	Plastic viscosity
H	Initiation Height	μ	Apparent viscosity
I_{DF}	Intensity index	ξ	Turbulence parameter
K	Consistency parameter	ρ	Fluid density (bulk)
L	Runout length	ρ_s	Solid density
L_i	Channel reach (i) length	σ'	Effective stress
n	Flow index	σ	Total stress
p	pressure	τ	Shear stress (basal resistance)
Q	Average flow discharge	τ_y	Yield shear stress
R	Resistance coefficient	ϕ	Internal friction angle
S	Surface	ϕ_b	Basal friction angle
t	Time	υ	Kinematic viscosity
u	Pore fluid pressure	υ_o	Maximum kinematic viscosity
v	Flow velocity	υ_t	Eddy viscosity
v_f	Impact velocity (pillar)		

1 INTRODUCTION

1.1 DEBRIS FLOW HAZARDS

Debris flows are a rapid mass movement of soil, rock, water, and debris material. They occur periodically in steep mountainous terrain and are channelized within drainage paths. The periodic nature of this phenomena is often related to high rainfalls and flooding events. Debris flows may have a single or several consecutive surge events, where periodic damming and release of materials allows for consecutive events to grow in discharge; the growing discharge contributes to increased flow depth, impact loads, and the flows ability to entrain and transport bedloads downslope (Oldrich Hungr, Leroueil, & Picarelli, 2014).

The ability to model the behaviour and impact of debris flows and predict event inundation and severity are critical to building safe infrastructure that will minimize risk to human life. The design of countermeasures relies on a detailed understanding of debris flow mechanics and accurate predictive analysis of events. Traditionally, empirical relationships have helped govern mitigation design, but continued computational developments make it less and less time consuming to model these events in three dimensions numerically. Numerical modelling of debris flows can be used to estimate flow intensity parameters and can provide event visualization that make presentation and communication of these hazards more understandable (McDougall, 2016).

1.2 COMPUTATIONAL FLUID DYNAMICS

Computational fluid dynamics (CFD) is a method of taking the fundamental principles of fluid flow and the accompanying mathematical equations and replacing the integrals/partial derivatives with algebraic forms. The algebraic

forms are solved to obtain discrete values in time and space, which results in a collection of numbers within the problem domain (Anderson, 1995). The advancement of digital computing has allowed CFD to be used as a third approach in the study of fluid dynamics – the other approaches being purely experimental and theoretical (Anderson, 1995). Detailed CFD calculations are enabled using modern computing infrastructure, which can solve the governing equations of fluid behaviour over large spatial and temporal bounds.

The majority of current debris flow modelling practice utilizes depth-averaged shallow flow fluid equations to simplify problem physics. The use of CFD can help capture detailed problem physics, and the full 3-dimensional debris flow propagation behaviour (Fornes, Bihs, Thakur, & Nordal, 2017).

1.3 OBJECTIVES

The objectives of this thesis are summarized in the following list:

- Introduce debris flows and their characteristics,
- Introduce numerical modelling methodology and rheological models for debris flow hazards,
- Present the REEF3D numerical code and the non-Newtonian rheologies that can be used to represent the debris flow material,
- Model and analyze the flume testing that was performed at NTNU in 2017 using non-Newtonian fluid rheologies and the numerical code REEF3D,
- Present the numerical simulation results and report the rheological parameters that provide the best fit to experimental testing.

1.4 MODELLING LIMITATIONS

Limitations to the CFD modelling in this report are presented in the list below.

- Ongoing software development – the CFD software REEF3D was used for numerical modelling and is still in development. Numerical instabilities and limitations are expected and are further outlined following the completion of the analysis.
- Large cell count – because the modelled flows are thin, and the flume is relatively large, the numerical analysis needs a high-resolution mesh for model accuracy. The problem was first split into separate models to analyze which flume components could be removed or simplified in the final models for the sake of computational efficiency.
- Data size – data transfer from the HPC server and post-processing of the data are time consuming, so doing a rigorous calibration with a wide range of parameter values is not possible.
- Modelling times – like most landslide runout analysis software, the time it takes to complete a single simulation is long (12-30 hours per model depending on model size).
- Single-phase fluid assumption – solid and liquid phases are modelled together in a single-phase fluid rheology. The aim is to describe macroscopic behaviour and not the detailed fluid-fluid and fluid-solid interactions. This assumption is good for fine-grains in suspension, but when coarser materials are involved a two-phase description may be necessary to describe flow behaviour.
- Viscous behaviour assumption – the use of non-Newtonian fluid rheologies assume that the flow mechanics are described solely in a viscous regime. The material used in the physical flume models has the potential for both viscous and frictional behaviour, but is assumed

to be adequately described by the presented rheology model. The viscous fluid assumption is adequate under flow, but a viscous fluid will not deposit on a non-horizontal surface. The final deposition is not of a solid material, but of a viscous fluid with a very small shear rate.

1.5 REPORT STRUCTURE

The report is structured in two parts, the first part provides a literature review on debris flow hazards and a review of general runout analysis practice. The second part reviews the laboratory flume testing, numerical modelling code, simulations, discussions, and results.

Part 1: Debris Flow Hazards

Section 2: Literature Review: Debris Flow Hazards

Section 3: Runout Analysis of Debris Flow Hazards

Part 2: Physical and Numerical Modelling

Section 4: Laboratory Flume Testing

Section 5: Numerical Modelling using REEF3D

Section 6: Numerical Model Sensitivity Study

Section 7: Numerical Model Calibration

Section 8: Conclusions

Following the Sections above, the Appendices present simulation results and input code for the numerical modelling cases.

2 LITERATURE REVIEW: DEBRIS FLOW HAZARDS

2.1 BACKGROUND

A landslide is a mass movement event of earth, rock, or organic material downslope under the influence of gravity. The updated Varnes classification breakdowns landslides into 32 different types based on materials involved, movement type, and mechanisms. Material types are simplified into 3 categories: rock, debris, and earth. Each material class generalizes the materials involved, but further information on the mass movements behaviour and composition helps classify the landslide further.

The updated Varnes classification of landslide types by Oldrich Hungr et al. (2014) classifies a debris flow as the following:

> *"Very rapid to extremely rapid surging flow of saturated debris in a steep channel. Strong entrainment of material and water from the flow path".*

Debris materials can have a varying geomorphic origin and generally include a mixture of boulders, cobbles, and gravel to clay portions, along with tree and wood mulch which have accumulated in channels (Oldrich Hungr et al., 2014; VanDine, 1985).

Due to their rapid and mobile behaviour, debris flows can be extremely destructive to infrastructure. Figure 2-1 below shows the destruction caused by a debris flow in Glyssibach, Brienz, Switzerland in 2005.

Figure 2-1: Debris flow deposition and damage in Brienz, Switzerland ("Murgang am Glyssibach, Brienz.," 2005)

2.2 CLASSIFICATION

Richard M. Iverson (1997) suggests a simplified classification, where the criteria for definition is "the necessity of interacting solid and fluid forces" – this allows for a broader classification scheme, where many different types of flows are eligible to be defined as debris flows.

A more detailed classification of debris flows is provided by Takahashi (2014), who classifies debris flows in the following 3 different categories based on material sizes and distributions, interstitial fluid properties, and hydraulic flow conditions:

a) *Stony-type debris flow*, is characterized by a front in which coarser grained sediments are not supported by fluid pressure, but are controlled by grain collisions instead. Material densities range from

1.0 g/cm^3 in the more fluidized material behind the front, to 1.5 g/cm^3 in the stony forefront material (Takahashi, 2014).

b) *Turbulent-muddy-type debris flow*, generally comprised of fine ash material, are characterized by (violent) turbulent flow throughout the flow mass. The median grain-size was found to range from 0.3-1mm, with finer grain fractions (<0.1mm) accounting for 10-30%. Solids concentrations range from 35-72% by volume (Takahashi, 2014).

c) *Viscous debris flow*, is characterized by a surging behaviour in which bed entrainment is critical for progressive surge development. The viscous debris flow does not have a course-grained/boulder front like the stony-type debris flow, and there is no particle segregation during flow. Flow is comprised of a slurry material (<0.1mm) and coarser grained particles (>0.1mm) – apparent density of the flow material is approximately 1.3-1.5 g/cm^3 (Takahashi, 2014).

The term "debris flow" is used in literature and practice as a general term more in-line with the suggested classification by Richard M. Iverson (1997) – and is accompanied by information that helps describe the materials and behaviour. Generally, debris flows are a poorly sorted mixture of fluid and sediments, that typically contain more than 50% sediment by volume, and contain a particle size range from clay to boulders (Major & Pierson, 1992).

Typical material properties of debris flow masses are summarized by Richard M. Iverson (1997) in Figure 2-2 below.

Property and Unit	*Symbol*	*Typical Values*
	Solid Grain Properties	
Mass density, kg/m^3	ρ_s	2500–3000
Mean diameter, m	δ	10^{-5}–10
Friction angle, deg	ϕ_g	25–45
Restitution coefficient	e	0.1–0.5
	Pore Fluid Properties	
Mass density, kg/m^3	ρ_f	1000–1200
Viscosity, Pa s	μ	0.001–0.1
	Mixture Properties	
Solid volume fraction	υ_s	0.4–0.8
Fluid volume fraction	υ_f	0.2–0.6
Hydraulic permeability, m^2	k	10^{-13}–10^{-9}
Hydraulic conductivity, m/s	K	10^{-7}–10^{-2}
Compressive stiffness, Pa	E	10^3–10^5
Friction angle, deg	ϕ	25–45

Figure 2-2: Typical debris flow material properties (Richard M. Iverson, 1997)

2.3 PHYSICAL ENVIRONMENT

The occurrence locations and frequency of debris flows depends on several factors. VanDine (1985) describes the controlling variables as drainage area, creek profile, source of debris, and climatic conditions, based on studies on the west coast of Canada in the Southern Canadian Cordillera. The drainage area must be large enough to accumulate debris and to divert enough water into the channel to saturate it, but not so large that drainage occurs by lower gradient stream and river channels. VanDine (1985) found that the optimum size of drainage area for the study area to be 0.4 to 7.0km^2.

The source of debris comes from surrounding slopes and channel walls and beds. Shallow and deep-seated sliding mechanisms contribute material to the gullies/channels. The majority of debris is contributed by undercutting and erosion of the gully/channel walls, and provides a continuous source of materials until the failure event occurs and the debris is transported

downstream (Oldrich Hungr, 2005). Oldrich Hungr (2005) describes the source of debris as follows:

"soil blankets and veneers on steep slopes, colluvial gully fills, channel bedload material, zones of weathered or altered rocks, residual soils, headwalls and side slopes of steep gullies, talus deposits, man-made fills, and similar accumulations of unstable or erodible material"

Forested slopes can provide organic materials through tree-fall and seasonal abscission to the channels. Figure 2-3 below shows a debris flow channel comprised of materials from channel erosion.

Figure 2-3: Debris flow channel showing eroded channel along with tree-fall (Oldrich Hungr, McDougall, & Bovis, 2005)

The creek profile is comprised of three different zones: initiation, transportation and erosion, and deposition (Oldrich Hungr, 2005; VanDine,

1985). The initiation zone is the steepest of the zones (generally greater than 25°) – but not steep enough that debris will not accumulate. Oldrich Hungr (2005) states that slopes steeper than 45° generally have minimal and/or discontinuous soil cover and are not vulnerable to sliding. Confirming this statement – R. M. Iverson, Reid, and Lahusen (1997) compiled the initiation angles for various debris flow events, and the table with the results is shown in Figure 2-4 below.

Reference	Location	Slope angles (degrees)
Temple & Rapp 1972	Tanzania	28–44
O'Loughlin 1972	Southwestern British Columbia, Canada	24–48
Lumb 1975	Hong Kong	25–45
Campbell 1975	Southern California, USA	27–56
Selby 1976	New Zealand	32–34
Statham 1976	Wales	27–37
Pomeroy 1980	Pennsylvania, USA	20–40
Heller 1981	Northwestern Washington, USA	20–40
Ellen et al 1988	Northern California, USA	20–50
Pierson et al 1992	Hawaii, USA	30–60
Rickenmann & Zimmermann 1993	Switzerland	27–39

Figure 2-4: Intitiation angles measured at debris flow sites (R. M. Iverson et al., 1997)

The transportation and erosion zone is more moderate in gradient, but still steep enough to maintain the velocity of the debris flow before the depositional zone is reached. The depositional zone starts when the creek profile flattens to approximately less than 15°; VanDine (1985) found that the average fan angle was in the range of 8° to 18° for the debris flows studied. O. Hungr, Morgan, and Kellerhals (1984) suggest a range of deposition angles of 10° to 14° for unconfined failures and 8° to 12° for channelized debris flows based on experiences in coastal British Columbia, Canada. A more comprehensive inventory of debris flows was performed by Guthrie et al. (2010) in the same region; it was found that deposition occurred between 12° to 15° for

channelized debris flows, and as steep as 18° to 24° degrees for unconfined failures. The variations in the above ranges highlights the uniquity of creek profiles and depositional environments for individual events.

Confinement affects the grades of all of the zones; a fully confined creek profile allows velocities to be maintained, and may allow for gradients on the shallower side of the spectrum, while a poorly or un- confined creek profile may require steeper gradients to maintain flow velocities (VanDine, 1985).

2.4 CLIMATIC CONDITIONS

Takahashi (1981) observes that debris flows occur because of heavy rainfall events, and R. M. Iverson et al. (1997) states that most subaerial debris flows occur due to "shallow groundwater flow in response to rainfall, surface runoff, and snowmelt". Requisites for debris flow mobilization are saturation of the soil mass and sufficient pore water pressure (R. M. Iverson et al., 1997).

Climatic factors influence the occurrence and behaviour of debris flow hazards, and provide critical context for understanding the hydrological soil response and how climate-change will affect it (Wieczorek & Glade, 2005). Wieczorek and Glade (2005) summarize that there are two different climatic influences on debris flows and their occurrence: primary influences and secondary influences.

Primary climatic factors are direct triggers to debris flow events, examples of these influences are intense rain events or rapid snowmelt. Bed instability can build over the duration of a rainfall event as pore water pressures infiltrate the soil medium – the effect of the infiltration is a reduction in effective stress of soil. Loss of matric suction (change of negative pore water pressures to positive) in the unsaturated zone of the soil mass can lead to shallow failures. Increased water infiltration by rapid snowmelt can also cause the effects

outlined above. Secondary climatic factors are indirect triggers that do not cause immediate failure events – the main factor is antecedent rainfall and melting of snowpack - and the subsequent increase of pore water pressure in the soil (Wieczorek & Glade, 2005).

Rainfall thresholds can help predict and warn of impending debris flows, and is a system that has seen adoption worldwide. Regional studies are required to capture variations in morphology, geology, hydrology, and vegetation (Wieczorek & Glade, 2005).

2.5 TRIGGERING EVENTS

Oldrich Hungr (2005) states that the magnitude of the triggering event can vary considerably; the resulting debris flow can also vary largely – a small magnitude initiation event can produce a large debris flow and vice versa.

Initiation of a debris flow is summarized in the following 3 different scenarios by Takahashi (1981):

a) A landslide evolves/transforms into a debris flow
b) A natural dam in a channel/gully is breached and causes a debris flow
c) A surface water stream during an intense rainfall event causes accumulated debris to become unstable, and causes a debris flow

The process that facilitates the transformation of a landslide mass into a debris flow is undrained loading of the bedload. Rapid loading of the debris flow channel by a sliding mass causes a large increase in total stress within the sediment, which results in large excess pore pressures – Equation 1 below describes this behaviour.

$$\Delta\sigma' = 0 \rightarrow \Delta\sigma = \Delta u \quad (1)$$

Where: σ' is the effective stress

σ is the total stress

u is the pore fluid pressure

If the undrained loading is in excess of the soil strength, failure of the bed occurs. Volume reduction of the loosely packed debris mass occurs under failure (contraction). Sufficient contractive behaviour can assist a localized failure convert into a larger failure mass (Richard M. Iverson, 1997). Bed liquefaction is a common result of this unexpected undrained loading – "loose and unstable structure can collapse structurally under rapid loading", and liquefaction at the base of the of the deposit mass occurs (Sassa & Wang, 2005).

2.6 PHYSICAL BEHAVIOUR

The dynamic behaviour of debris flows is caused by fluid and solid forces working together to drive the saturated, sediment laden mass downslope. Debris flow energies evolve throughout the initiation to the depositional stage of the event, and this evolution can be described by the following conversions summarized by Richard M. Iverson (1997):

bulk gravitational potential energy

↓

bulk translational kinetic energy

↕

grain vibrational kinetic energy + fluid pressure energy

↓

heat

The conversion from potential to kinetic energy in the first stage of initiation requires an initiation event and sufficient saturation of the flow sediment. During failure of the flow mass, the loose granular mass undergoes contraction – which creates additional pore water pressure that further weakens the mass, and aids in flow behaviour (Richard M. Iverson, 1997).

After flow mass mobilization, the debris flow mass is controlled by bulk translational, grain vibrational and fluid pressure energies. Mobility is enhanced when energies are predominately in the forms of the latter two energies – both increase the movement of grains beyond each other. Deposition occurs once all forms of energy have been converted to irrecoverable forms of energy (i.e. heat). Surging behaviour can re-mobilize deposited material and bring it back into the energy evolution chain outlined above (Richard M. Iverson, 1997).

Debris flows have a characteristic dynamic surge behaviour (individual or successive) where grain segregation occurs to create a coarser sediment front, followed by a finer flow body. Segregation causes spatial variations of excess pore pressure and frictional resistance within the flow mass. The surge fronts have little excess pore pressure and have high frictional resistance; surge bodies typically have high excess pore pressure and low frictional resistance. The low-resistance liquefied body pushes the coarser surge front downstream

(Richard M. Iverson, 2005). Figure 2-5 below shows the grain-segregation and grain trajectories throughout the debris flow mass.

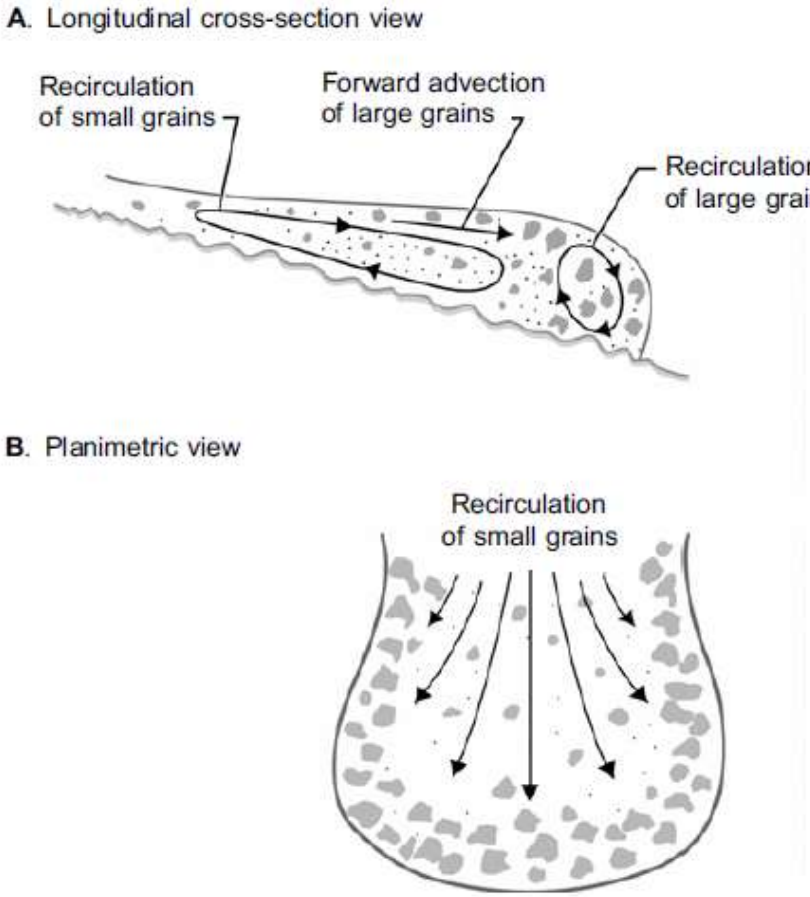

Figure 2-5: Grain-size segregation and grain trajectories in debris flow mass (Richard M. Iverson, 2005)

2.7 ENTRAINMENT

The magnitude of a debris flow is the final volume transported to the depositional zone – which can be used to scale the event and help estimate maximum discharge and runout distance (Oldrich Hungr et al., 2005). As mentioned previously, the magnitude of the initiation event and magnitude of

the debris flow can not be associated directly – rather, Oldrich Hungr et al. (2005) states that:

> *"it is the efficiency of the entrainment mechanism that primarily determines the total volume of a debris flow."*

Erosion and destabilization of the bed sediments caused by drag forces from the flowing mass, combined with bed instability, can cause a rapid growth in the events size and destructive power. Destabilization forces not only effect the bedload, but can also cause erosion and mobilization of the bed substrate. Quantifying the amount of sediment vulnerable to destabilization forces by a given debris flow is a difficult task that requires knowledge of the materials, their strength, and drainage properties (Oldrich Hungr et al., 2005). Figure 2-6 below shows a simple cross-section of a channel and the materials vulnerable to destabilization.

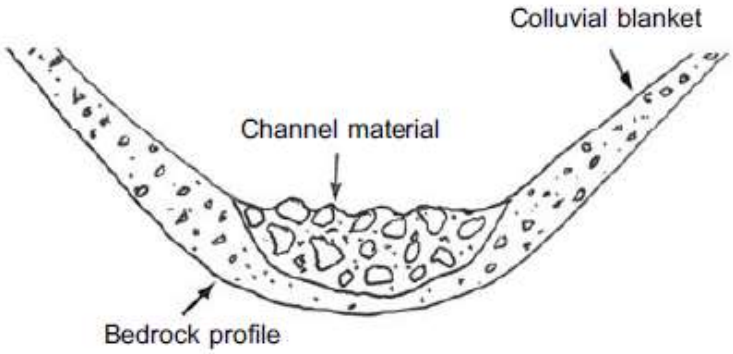

Figure 2-6: Cross section of a debris-flow channel (Oldrich Hungr et al., 2005)

The other important entrainment mechanism, channel instabilities, is caused by constant incision of the channel walls caused by erosion at the base of the channel. Oldrich Hungr et al. (2005) describe the stream banks as being in "marginal equilibrium that is easily disturbed by lowering of the bed, such as often occurs during passage of a debris-flow surge". Debris flow surges can

entrain the instabilities and cause further channel wall instabilities that can be entrained by succeeding surges.

The prediction of the magnitude of the entrainment is therefore an important step in predicting the final volume of a debris flow. O. Hungr et al. (1984) formulated a relationship between final debris flow magnitude and debris flow material sources, by proposing a channel debris yield rate – defined by the volume eroded per metre of channel length. The channel debris yield rate (Y) is calculated by finding the area of erodible material (A) in a vertical channel cross-section, and multiplying this value by the cosine of the slope angle (β) – which gives an area normal to the slope angle. The formulation of channel debris yield rate is shown in Equation 2 below:

$$Y = A \cdot \cos\beta \tag{2}$$

Different yield rates for sections of the channel with similar slope angle and erosional properties are found and multiplied by the length of the corresponding section (also known as channel reach) – giving an entrainment volume. The initial volume of the initiating landslide is included in the formulation for final magnitude, along with point sources of debris – which are localized channel instabilities that can add 10% or more volume to the debris flow (O. Hungr et al., 1984).

The final magnitude (volume in m^3) of the debris flow can be estimated by using Equation 3 proposed by Oldrich Hungr et al. (2005); O. Hungr et al. (1984) below:

$$V = V_{initial} + \sum V_{point} + \sum_{i=1}^{n} Y_i \cdot L_i \quad (3)$$

Where:

V	is the final debris flow magnitude
$V_{initial}$	is the initial failure mass magnitude
V_{point}	is the magnitude of a point mass
Y	is the channel debris yield rate
L	is the channel reach length

Equation 3 above provides a good estimate for debris flow magnitude, but in practice is difficult to use. Variability and uniquity of deposition angle, material properties, surge properties, and channel erosional properties for different locations are not directly accounted for in the formula. The nature of the channel and formulas inputs are stochastic, and require detailed data collection in the field by experienced personnel to determine representative values (Oldrich Hungr et al., 2005).

Several entrainment experiments were performed by Richard M. Iverson et al. (2010) in a large debris flow flume. It was found that rapid loading of saturated channel sediment generated excess pore pressures and helped facilitate entrainment, and that entrainment occurred because of mass movement of the debris flow sediment – not progressive scour of the bed material. Considerable entrainment was observed in the wet bed tests where large increases in pore water pressure occurred, causing liquefaction of the bed sediment and overall growth of the debris flow mass. In these cases, runout distances and flow masses both increased when compared to the dry bed sediment and control (no bed sediment) cases. Flow momentum increases in the wet bed sediment case as the resistant basal friction forces are reduced to close to zero as bed sediment mobilizes and liquefies into a flow mass that slightly lags the main

flow mass. The trailing flow mass helps facilitate the driving of the coarser flow bulb downstream as it experiences less resistant forces. The experiments by Richard M. Iverson et al. (2010) clearly display a positive feedback loop between bed wetness and mass and momentum growth of the debris flow.

2.8 HAZARD ANALYSIS

Prevention of loss and damage to infrastructure and humans due to debris flow hazards is critical to ensure safe land use. The majority of damage occurs within the depositional zone of the creek profile – these fans are also a desirable place to build because they are well drained with gentle slopes (Matthias Jakob, 2005).

Matthias Jakob (2005) breaks the debris flow hazard analysis into 6 steps, and these 6 steps are shown in Figure 2-7 below.

Step	Action
1	Debris flow hazard recognition
2	Estimation of debris flow probability
3	Estimation of debris flow magnitude and intensity
4	Production of debris flow frequency–magnitude relationships
5	Estimation design of debris flow magnitude and intensity
6	Presentation of debris flow hazards on maps and writing a debris flow hazard analysis report

Figure 2-7: Steps in debris flow hazard analysis (Matthias Jakob, 2005)

Magnitude and frequency give a basis for describing debris flows in a probabilistic manner. Magnitude refers to debris flow volume, and frequency is typically evaluated on an annual basis or on a return period required for design. Magnitude and frequency vary from location to location and are dependent on the physical environment and climatic conditions. Two basin categories are defined by Matthias Jakob (2005), and are summarized below:

i) *Supply-limited*: low frequency basins, where channels are typically filled with coarser debris, extreme climatic events trigger debris flows.

ii) *Supply-unlimited*: high frequency basin, where a constant supply of erodible material is available to the channel.

The two basin types are further summarized in Figure 2-8 below.

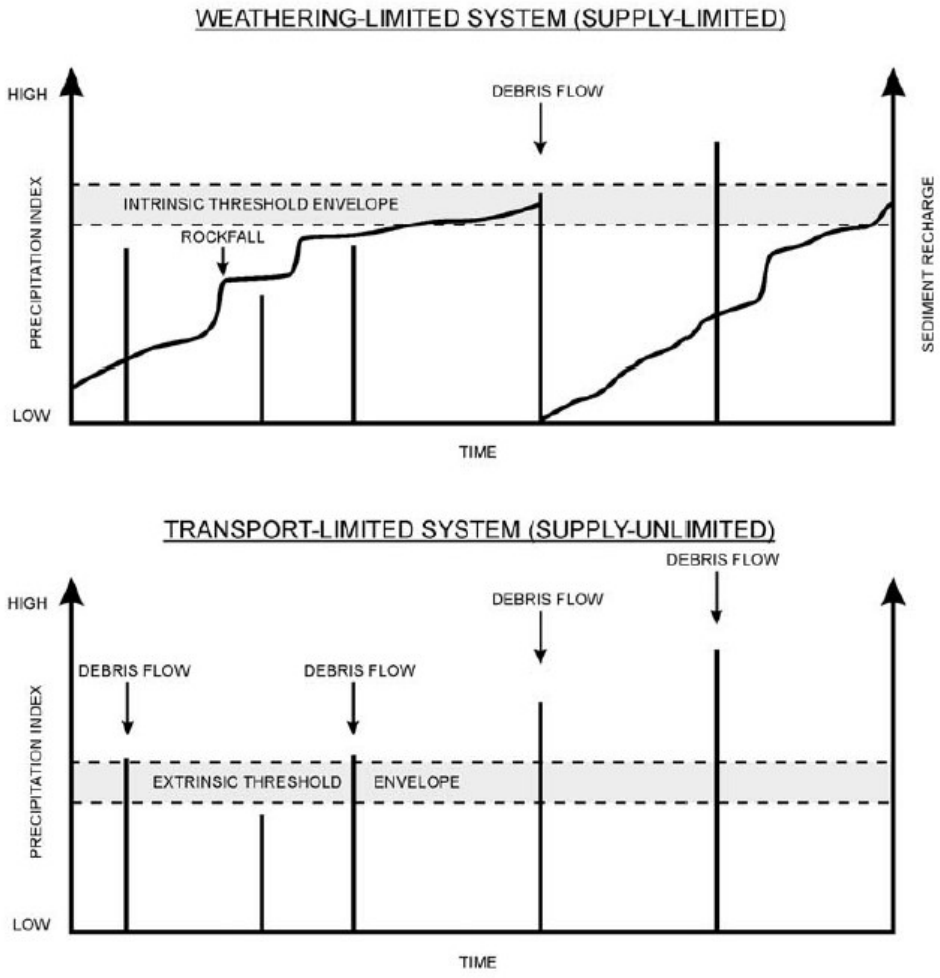

Figure 2-8: Comparison of frequency and sediment recharge for supply-limited and supply-unlimited basins (Matthias Jakob, 2005)

Frequency estimates can be difficult to obtain if the area is in a supply-limited basin. Dating methods can be used to analyze underlying fan geomorphology to attempt to find deposition relationships with depth. Debris flow magnitude (volume) can be estimated using the formulas presented in Equation 3.

Infrastructure vulnerability and potential damage can be estimated by using the debris flow intensity index proposed by M. Jakob, Stein, and Ulmi (2012) – Equation 4 below shows the intensity index and its factors.

$$I_{DF} = d \cdot v^2 \quad (4)$$

Where: I_{DF} is the intensity index

d is the maximum flow thickness

v is the maximum flow velocity

Based on the intensity index – the downstream environment can be zoned into areas based on expected damage intensity. M. Jakob et al. (2012) has correlated four different damage categories based on the intensity index – ranging from some sedimentation (low intensity) to complete destruction (high intensity).

Frequency-magnitude relationships are a critical part of hazard analysis and the resulting design of mitigation measures. Based on frequency-magnitude curves and estimated event intensity, hazard maps can be created to outline areas and their debris flow risk.

Based on risk, decisions can be made regarding infrastructure and zoning, and if additional mitigation measures are necessary.

2.9 MITIGATION MEASURES

Mitigation measures are important to reduce the risk and severity of debris flow hazards; Hübl, Fiebiger, Jakob, and Hungr (2005) describe the following types of mitigation measures that are used in practice:

i) *Active measures*: focus on mitigation of the debris flow itself.
ii) *Passive measures*: focus on potential damage that can be caused by the debris flow.

Active measures can be categorized into disposition management or event management sub-classes. Disposition management aims to reduce the probability of occurrence of debris flow events by decreasing run-off and erosion. Event management aims to influence the debris flow itself by controlling discharge and debris during an event.

Examples given by Hübl et al. (2005) of active measures are summarized below.

i) *Forest management*: decrease surface run-off by maintaining forest cover.
ii) *Soil bioengineering:* plants are used for erosion control and to govern groundwater supply; most effective when combined with event management structures.
iii) *Watershed Management:* minimize the need for protective structures by maintaining vegetation and forest cover, effectively reducing natural hazard magnitude.
iv) *Drainage:* drain water from hillsides/wet areas – preventing the build-up of pore pressures.

v) *Toe slope stabilization:* reduce bank erosion by stabilizing toes using longitudinal support structures; and reduce bed erosion by stabilizing toes with traverse support structures.

vi) *Bypass:* avoid excessive sediment entrainment by limiting channel reaches available to a debris flow event.

vii) *Water retention:* flood control dams can be installed to limit the amount of water available to certain channel reaches.

viii) *Permanent debris deposition:* dams are built to prevent debris flows from reaching high-consequence areas – measure is largely ineffective today as it has proven to have negative effects on stream erosion and stream ecology.

ix) *Temporary debris deposition:* addressing issues with permanent deposition, temporary deposition aims to allow smaller particles to pass through the dam structure – while retaining larger boulders.

x) *Debris-flow breaker:* energy dissipation structures that can be installed on check dams, designed to slow and deposit the surge front of the debris flow – decreasing event magnitude downstream.

xi) *Deflection:* used to re-route debris flow to lower consequence areas – typically used as the last line of defense against debris flows to remove any remaining risk.

xii) *Wood debris rake:* designed to separate wood/organics from soil – constructed in combination with other structures.

Figure 2-9 and Figure 2-10 below show a couple examples of event management structures installed in debris flow prone channels.

Figure 2-9: Sectional barrier with fins/beams in Maerzenbach, Tyrol, Austria (Hübl et al., 2005)

Figure 2-10: Sectional barrier with fins in Fong-Chiu, Nan-Tou County, Taiwan (Hübl et al., 2005)

Passive debris flow measures can be categorized into preventative management and event response. Preventative management aims to reduce the potential of infrastructure and human loss by hazard mapping and land-use zoning – by identifying areas of risk, they can be avoided. Event response measures involve the closure of roads, warning systems and evacuation of areas of risk, and/or the dispatch of technical assistance (Hübl et al., 2005).

Modern day channel management utilizes multiple of the listed active measures to provide stability and energy dissipation for sufficient reduction of event magnitude and occurrence. Effective mitigation strategies use both active and passive measures to control the influence and reduce the risk of a debris flow event.

3 RUNOUT ANALYSIS OF DEBRIS FLOW HAZARDS

3.1 INTRODUCTION

Landslide runout analysis is a valuable tool used to analyze the behaviour of landslides post-mobilization. Simulation of previous landslide events, along with the forecasting of future events can be modelled to estimate their behaviour and impact. This is especially true in the case of debris flows, where modelling is utilized in risk assessment, design of mitigation structures, and evaluation of inundation areas.

McDougall (2016) states that there are two main methods of modelling that are used for predicting landslide runout:

(i) empirical-statistical methods
(ii) analytical methods

3.2 EMPIRICAL-STATISTICAL METHOD

The most common empirical-statistical methods relating to landslides are simple geometry or energy relationships which describe the correlation between the initiation height and final deposition location and size.

Rough hazard areas can be found by using the travel distance and event magnitude – "Fahrböshung" (angle of reach) is a commonly used empirical method that measures the angle between the crest of the initiation volume and the tip of the deposited volume (Rickenmann, 2005). With a large event database, statistical correlations can be made to use in a quantitative risk assessment. The design of mitigation structures can be tailored to exceedance probabilities to ensure that future flow events have a low probability of impacting infrastructure or persons downstream (McDougall, 2016). An

example of how the "Fahrböshung" method can be used in quantitative risk assessment is shown in Figure 3-1 below.

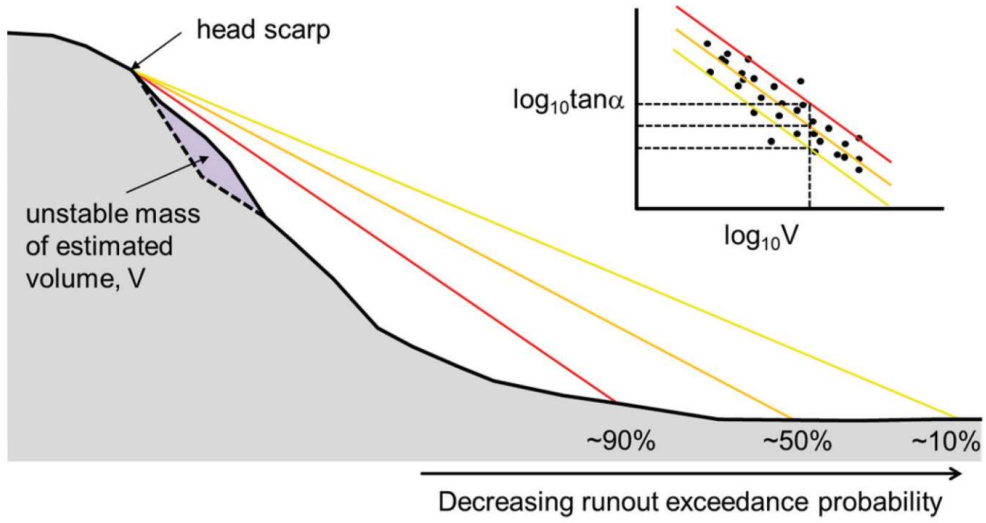

Figure 3-1: "Fahrböshung" method showing a correlation between mass volume and angle of reach. Collected data is analyzed statistical to find exceedance probabilities. (McDougall, 2016)

Simple conservation of energy principles can be used to predict runout distances, or back calculate resistance coefficients. Assuming no additional entrainment, Richard M. Iverson (1997) summarizes the pre- and post mobilization relationship between initiation height and deposition length in Equation 5 below:

$$\frac{1}{R} = \frac{L}{H} \tag{5}$$

Where: R is the resistance coefficient

L is the runout length

H is the initiation height

Potential energy can be compared to final energy at deposition, but energy losses along the flow path can be hard to quantify – and results from Richard M. Iverson (1997) found that the debris flow saturation and mass affect runout distance, and these considerations are difficult to implicitly include in the simple energy equations.

Empirical relationships help provide approximations of runout distance, and if a large enough database can be collected from past events, can provide a good basis for further statistical analysis. Internal flow behaviour is not directly considered, so a detailed understanding of the complex behaviour of landslides is not required, but this simplification can leave potential gaps in the analysis that can have negative repercussions when using an entirely empirical approach.

3.3 NUMERICAL MODELLING

Numerical modelling methods can help provide more detailed information that can not be obtained from empirical-statistical methods – numerical methods can provide detailed flow properties such as: debris flow depth, velocity, and impact forces. Results can be presented using time-lapse videos or animations which help provide with visualization of the event (McDougall, 2016). The most complete description of flow behaviour can be described by continuum based models which solve mass and momentum equations at time steps within the flow mass (McDougall, 2016; Rickenmann, 2005).

Numerical modelling uses a combined approach of the two methods, which can be called “semi-empirical”; in this method empirical relationships can help determine and calibrate the material parameters needed to satisfy the numerical conditions and behaviour (McDougall, 2016). The relationship

between the methods and how they relate for landslide modelling is shown in Figure 3-2 below.

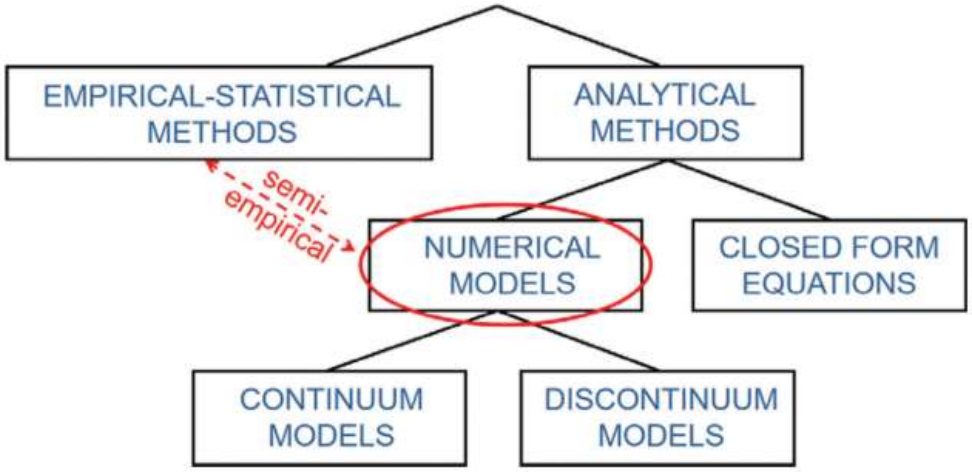

Figure 3-2: Numerical modelling using a semi-empirical approach to combine empirical-statistical and analytical methods. (McDougall, 2016)

Debris flow modelling uses modified hydrodynamic modelling methods to model flow – and provide "the most sophisticated tool for practical forecasts of debris flow runout and inundation limits" (Richard M. Iverson, 1997). Modifications can be made so equations include entrainment, internal stresses, and rheology variations (Oldrich Hungr, 2009; McDougall, 2016). Micro-mechanics of the flow motion are not analyzed, instead debris flow simulation models consider the solid-fluid mixture as a homogenous fluid – and the behaviour of this fluid is modified through use of rheological models (Oldrich Hungr, 1995, 2009; Rickenmann, 2005). Several rheological models exist and generally through proper calibration techniques can results in a good match to dynamic flow behaviour. An example of a time-lapse of a numerical model, DAN3D, used to simulate debris flow behaviour is shown in Figure 3-3 below.

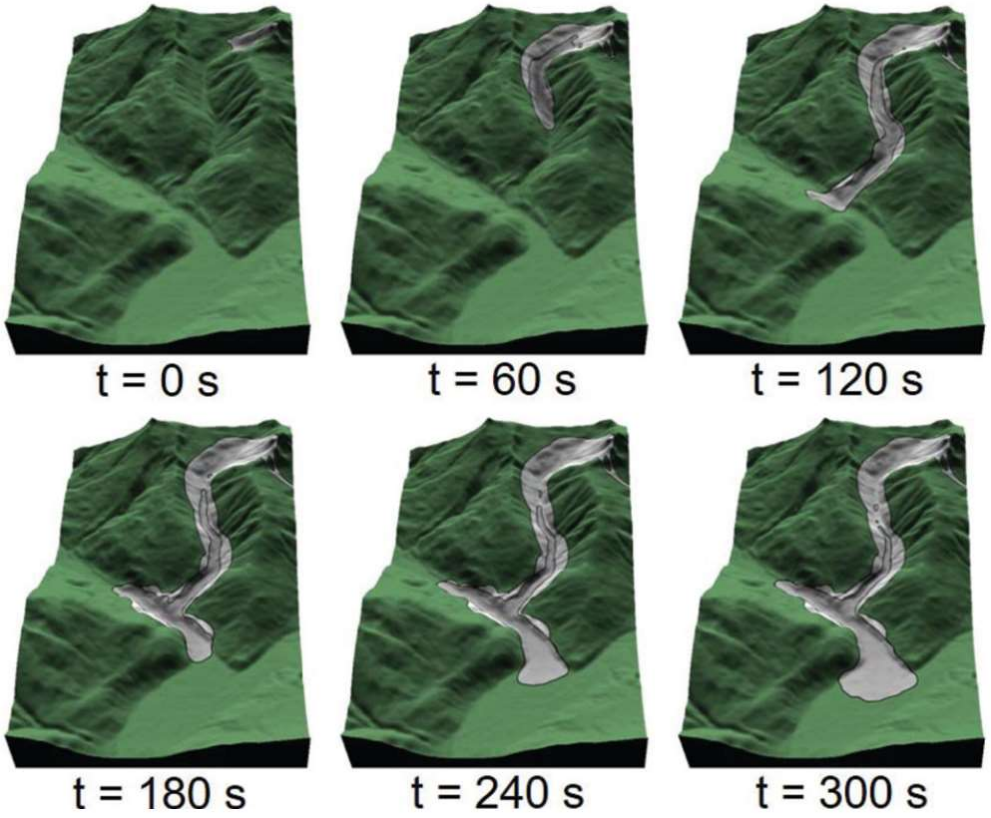

Figure 3-3: 2010 Mount Meager debris flow event modeled in DAN3D continuum software (McDougall, 2016)

The advancement of computational power and efficiency has seen numerical modelling of complex geotechnical problems become frequent in educational and work environments. Continued research activities, simulations, back-analyses, and laboratory work is required to hone the numerical tools into a reliable method for "predictions of velocities and runout distances for practical uses in hazard assessment and mitigation" (Oldrich Hungr, 2009). McDougall (2016) states that the largest challenge is "the selection of model input parameters within a framework that is suited to quantitative risk assessment".

3.3.1 RHEOLOGICAL MODELS

The complex and heterogeneous nature of debris flows is hard to model at a microscopic level with current numerical practice. Small-scale mechanical effects which vary with location and time, such as flow segregation, variations in pore fluid pressure, particle collision and alignment, cannot be described adequately by rheology definitions (Richard M. Iverson, 2003). Instead, debris flow dynamics are summarized in an equivalent fluid framework to describe the flow behaviour of a single-phase fluid, while not attempting to describe detailed fluid-solid and solid-solid interactions (Oldrich Hungr, 1995). Shear resistance (basal resistance) is a function of rheological parameters that are determined through calibration – or in the case of non-Newtonian rheologies, calibration and/or laboratory testing. Back-analysis of rheological parameters is performed by matching landslide properties (boundary, distribution, velocity, and event duration) to simulation results (Oldrich Hungr, 2009).

A summary of common rheological models used for debris flow modelling are outlined in the sections below:

3.3.1.1 Frictional

Frictional rheology is the simplest model, where shear resistance is controlled by one parameter and includes pore pressure effects (McDougall, 2016; Savage & Hutter, 1989). Equation 6 below shows the shear stress relationship for the frictional rheology model.

$$\tau = \sigma \cdot \tan \varphi_b \quad (6)$$

Where: σ is the bed normal effective stress

φ_b is the bulk basal friction angle

3.3.1.2 Voellmy

The Voellmy model was initially formulated to model snow-avalanche behaviour (Voellmy, 1955), but has since been modified to model landslide behaviour (Körner, 1976). The Voellmy rheology is presented in Equation 7 below.

$$\tau = \sigma f + \frac{\rho g v^2}{\xi} \quad (7)$$

Where: σ is the normal stress

f is the friction coeffcient

ρ is the fluid density

g is the gravitational constant

v is the velocity

ξ is the turbulence parameter

The friction coefficient (f) is equivalent to the frictional parameter used in the fricitional rheology ($\tan \varphi_b$) (McDougall, 2016).

3.3.1.3 Bingham

The Bingham plastic rheology model represents the simplest non-Newtonian yield stress fluid (Bingham, 1916). The Bingham model is shown in Equation 8 below.

$$\tau = \tau_y + \eta\dot{\gamma} \tag{8}$$

Where: τ_y is the yield shear stress

η is the plastic viscosity

$\dot{\gamma}$ is the shear rate

Bingham behaviour is characterized by a constant viscosity value once the yield stress has been exceeded.

3.3.1.4 Herschel-Bulkley

The Herschel-Bulkley rheological model has evolved from the Bingham model to include a power law variant to account for more complex behaviour in the form of shear thickening and shear thinning (Herschel & Bulkley, 1926). The rheological model is shown in the Equation 9 below.

$$\tau(\dot{\gamma}) = \tau_y + \kappa\dot{\gamma}^n \tag{9}$$

Where: τ_y is the yield shear stress

K is the consistency parameter

$\dot{\gamma}$ is the shear rate

n is the flow index

When n>1 shear thickening behaviour is observed, n<1 shear thinning behaviour is observed, and n=1 the Herschel-Bulkley model becomes the

Bingham model. The consistency parameter (K) is equivalent to the plastic viscosity parameter (η) in the Bingham model.

The coulomb viscous model can be integrated into the Herschel-Bulkley/Bingham models to describe the frictional behaviour of a granular flow (S. W. Johnson, Lee, Pyrz, & Thompson, 1970; Moriguchi, Borja, Yashima, & Sawada, 2009) – the yield stress parameter can be replaced by the following formula (Equation 10):

$$\tau_y = \sigma_n \cdot \tan\varphi + c \qquad (10)$$

Where: σ_n is the normal stress

φ is the internal friction angle

c is the cohesion

Figure 3-4 below shows the different behaviour of the Herschel-Bulkley model based on the flow index value.

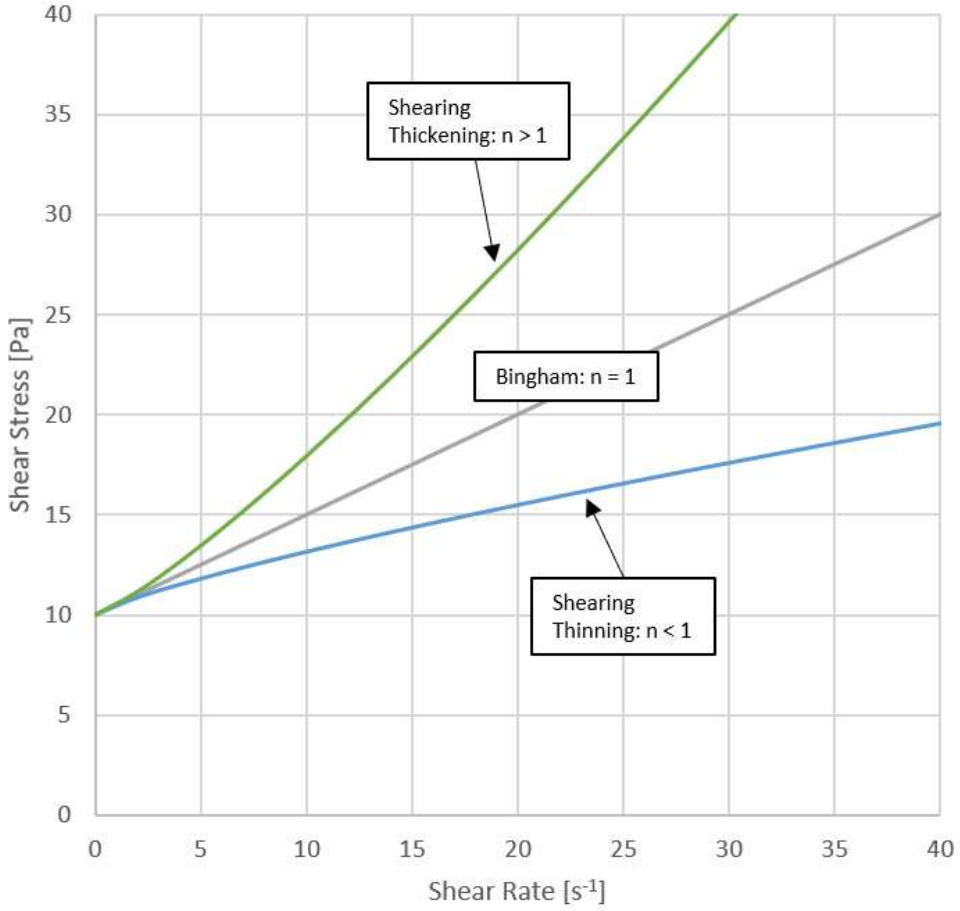

Figure 3-4: Herschel-Bulkley and Bingham models

4 LABORATORY FLUME TESTING

4.1 BACKGROUND

Flume modelling was performed by NTNU Ph.D. candidate Ashenafi Lulseged Yifru in March and June of 2017. A total of 9 tests were performed, of which 3 different groups of solid volumes were used (3 tests per group). The flow mass is mixed in a box prior to release to blend and liquefy the material. Flow velocity, maximum flow heights (upstream and downstream), impact forces, and flow runout were all measured for each of the flume tests. All raw data from the flume instrumentation and laboratory testing of the flow mixtures was provided for analysis.

The laboratory flume is 9m long and is comprised of a runout channel and deposition area. A slope angle of 23° (Runout1) transitions into a slope of 14° (Runout2) and is followed by the deposition area which is sloped 2°. At the transition between Runout1 and Runout2 the channel width reduces from 0.6m to 0.3m; the flume further widens to 2.5m in the deposition area. A circular pillar with a load cell (S2M Force Transducer) is located before the transition between runout and deposition and measures initial impact and residual forces during the tests. There are two flow height sensors which continually measure the flow thickness during the simulation – an upstream sensor is located 0.6m before the force transducer and the downstream sensor is located 0.4m after the flume transitions into the deposition area. Three cameras record the tests, and provide imaging of the final deposit geometry after the flow has ceased (Yifru, Pradhan, Thakur, & Nordal, 2017). The geometry of the flume and locations of the instrumentation is shown in Figure 4-1 below.

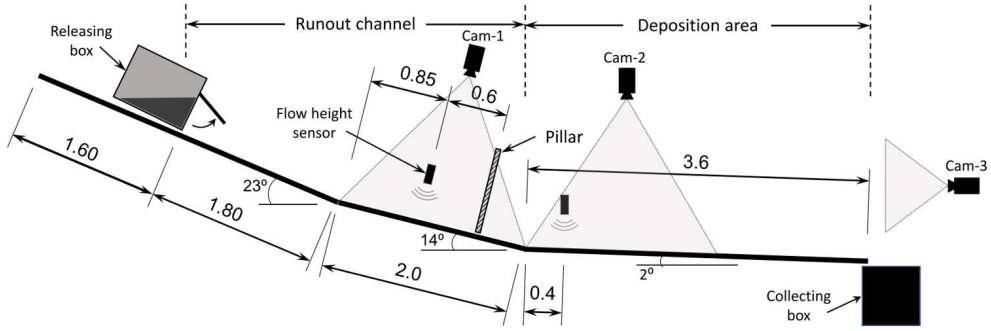

Figure 4-1: Debris flow flume at NTNU laboratory (all measurements are in metres) (Yifru et al., 2017)

4.2 MATERIAL PROPERTIES

The grain-size distribution for the debris material used in testing is shown in Figure 4-2 below.

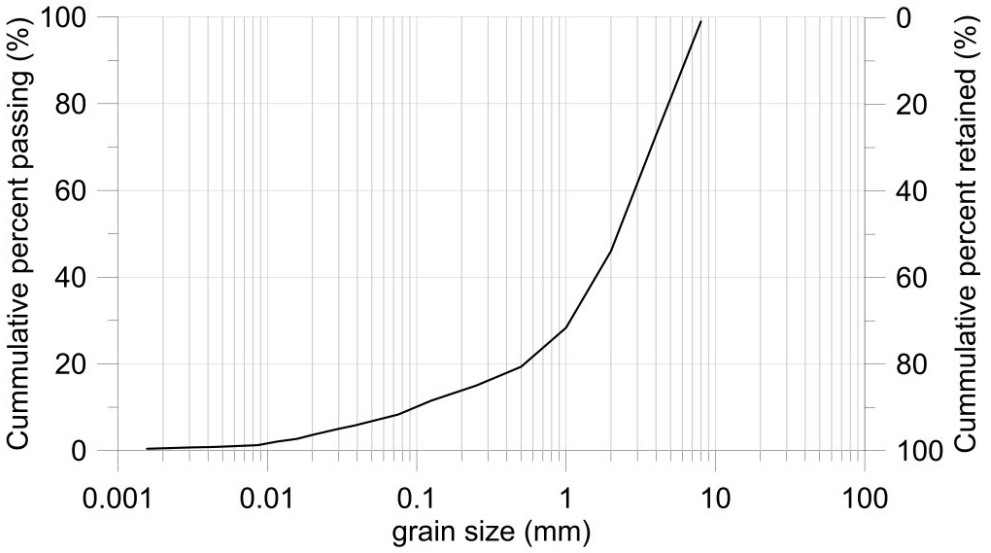

Figure 4-2: Grain-size distribution for the debris material (Yifru et al., 2017)

From the grain-size distribution, the following parameters were found:

$$d_{max} = 8.0mm$$

$$d_{60} = 2.9mm$$

$$d_{50} = 2.2mm$$

$$d_{10} = 0.1mm$$

$$Coefficient\ of\ Uniformity = C_u = \frac{d_{60}}{d_{10}} = 29$$

Based on the above coefficient of uniformity, the material can be classified as well-graded ($C_u > 15$). Solids concentration for each of the 9 tests was kept constant at 60% ($C_s = 60\%$), and the solid density for the debris material is 2720 kg/m^3 ($\rho_s = 2720\ kg/m^3$). The pre-test water content for all the tests was 11% ($w = 11\%$). The tested material is best characterized as a well-graded sandy/gravelly soil with a fines content (<0.04mm) of approximately 8%.

No direct measurements of rheologic parameters were performed and the validity of the rheological models was not supported with laboratory tests.

4.3 Results and Discussion

The pre-test measurements for the amount of water and debris material mixed is shown in Table 4.1 below.

Table 4.1: Pre-test measured solid and water mass values

Test	Date	Solid Mass (kg)	Water Mass (kg)	Total Volume (lt)	Solids Concentration (C_s) (%)
P1	30/06/2017	40.0	10.0	24.7	60.0
P2	30/06/2017	40.0	10.0	24.7	60.0
P3	30/06/2017	40.0	10.0	24.7	60.0
P4-2	07/03/2017	60.0	14.5	36.6	60.0
P5	07/03/2017	60.0	14.5	36.6	60.0
P6	07/03/2017	60.0	14.5	36.6	60.0
P7	07/03/2017	80.0	20.0	49.4	60.0
P8	07/03/2017	80.0	20.0	49.4	60.0
P9	07/03/2017	80.0	20.0	49.4	60.0

The measured material parameters post-test, along with the calculated flow densities is presented in Table 4.2 below.

Table 4.2: Post-test material properties

Test	Total Volume in Box (lt)	Net Volume of Flow (lt)	Actual Solids Concentration (C_s) (%)	Bulk Density of Flow (ρ) (kg/m^3)
P1	6.2	18.5	53.6	1922.4
P2	4.4	20.3	55.7	1958.2
P3	5.5	19.2	54.6	1938.6
P4-2	8.2	28.3	55.5	1954.8
P5	5.4	31.1	57.4	1988.0
P6	4.3	32.3	58.1	1999.6
P7	9.2	40.2	55.6	1955.5
P8	10.6	38.8	54.7	1941.6
P9	9.1	40.3	55.6	1955.9

Testing results are presented in Table 4.3 below.

Table 4.3: Results of debris flow tests

Test	Avg. Velocity (v_f) (m/s)	Max Flow Height - Upstream (mm)	Avg. Discharge at Impact (m^3/s)	Force (N)	Runout (cm)
P1	2.7	16.5	0.013	13.8	243
P2	2.7	19.2	0.016	16.2	198
P3	2.6	20.0	0.015	17.8	184
P4-2	2.4	23.7	0.017	17.1	185
P5	2.5	35.1	0.026	28.3	150
P6	2.5	21.4	0.016	21.2	167
P7	2.9	31.5	0.028	28.2	232
P8	2.6	32.0	0.025	29.2	223
P9	2.2	30.6	0.020	26.4	210

Impact velocity and runout of the flow did not vary with volume, so both values were averaged across all tests. The mean and standard deviation values used to target calibration of velocity and runout are shown in Table 4.4 below.

Table 4.4: Velocity and runout calibration values

	Mean	Std. Dev.
Velocity (v_f) (m/s)	2.57	0.20
Runout (cm)	199.1	29.0

The relationship between upstream flow thickness and the net flow volume can be summarized by an increase in flow thickness with volume; this correlation is shown in Figure 4-3 below.

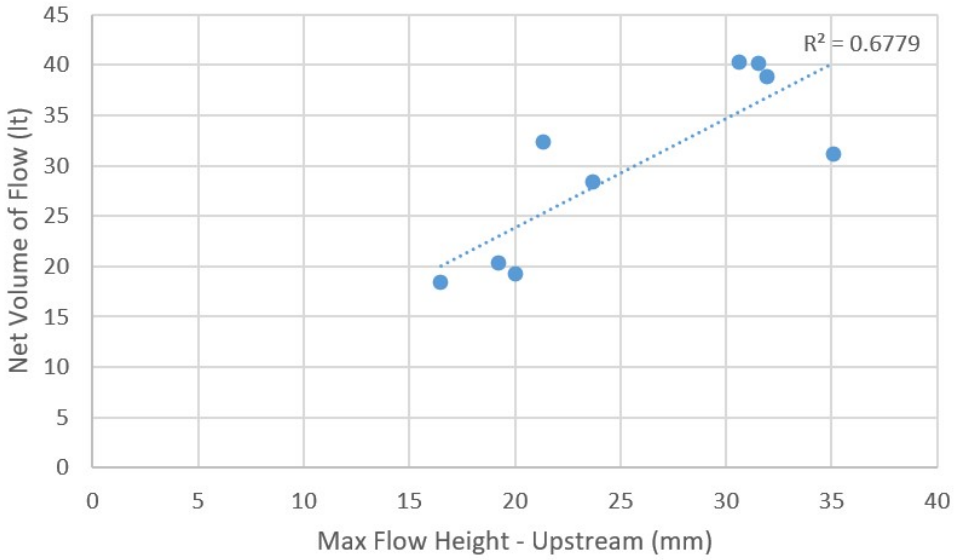

Figure 4-3: Volume vs. Upstream flow height

Yifru et al. (2017) presented a correlation between force measurements and flow discharge for the 9 flume tests – this correlation is presented in Equation 11 below.

$$F_{MAX} = 1100 \cdot Q \tag{11}$$

Where: F_{MAX} is the maximum pillar force

Q is the average flow discharge

The correlation coefficient shown above ($\alpha = 1100 Ns/m^3$) varies based on flume geometry and environmental factors. This relationship plotted for the physical testing data is shown in Figure 4-4 below.

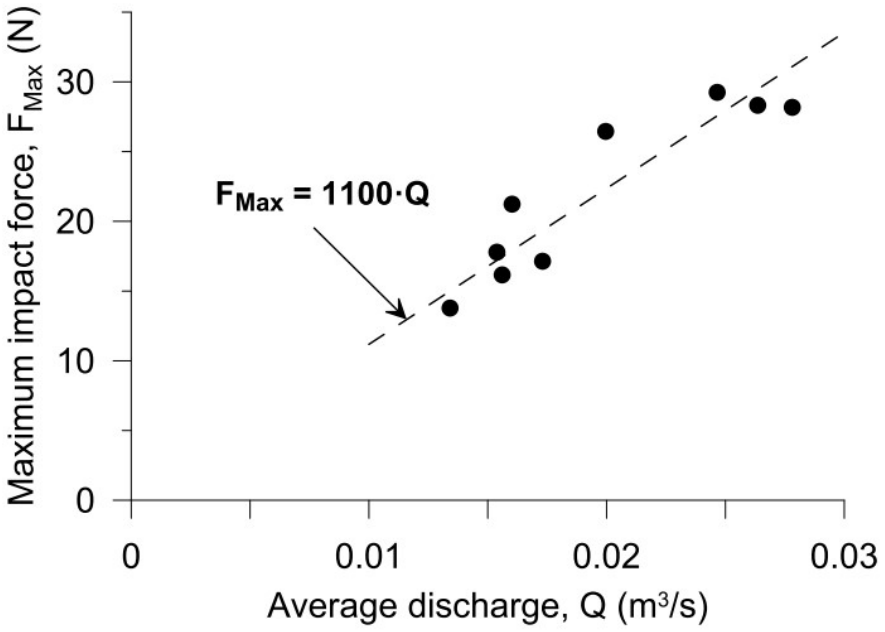

Figure 4-4: Force and discharge relationship for experimental data

Since the numerical model geometry is a good match to the flume geometry, this same relationship was used to calculate force measurements from the flow parameters that the CFD simulation outputs – and helps provide a direct correlation between the flow properties and force measurements found in the flume testing. Flow discharge (Q) is calculated in the same way for flume testing as it is for the numerical model – the flow thickness is assumed to be constant over the flume width based on the centreline value and the velocity value is based on the flow front value. Flow thickness in the flume testing was measured 60cm before the force transducer based on sensor location and was assumed to be equivalent to the value at impact.

Laboratory Flume Testing

5 NUMERICAL MODELLING USING REEF3D

5.1 BACKGROUND

REEF3D is an open-source numerical code designed to model fluid behaviour in three dimensions using computational fluid dynamics (CFD). DiveMESH is an open-source meshing code used to create a grid from the geometry input file. The finite difference method (FDM) is used to solve the Navier-Stokes equations numerically. REEF3D is run remotely utilizing the High-Performance Computing (HPC) network provided by UNINETT Sigma2 AS[1] – who manages the computational science infrastructure for Norway. The REEF3D code is in early development, and updates for improved numerical stability and capabilities, along with bug fixes were provided throughout modelling. REEF3D version 180513 and DiveMESH version 170513 was used for all final numerical simulations. 8 nodes of 32 processors each were used for simulations – in total 256 processors were used for CFD simulations.

The main modification to hydrodynamic modelling to simulate debris flows is the use of different rheological models that change the way the material flows under shear stress.

5.2 FINITE DIFFERENCE METHOD

The Finite Difference Method (FDM) is a numerical method in which differential operators are replaced with discrete difference relationships which approximate the derivatives (R. W. Johnson, 2016). Most commonly Taylor's series expansions are used to represent the derivatives. A regularly spaced grid is created over the problem space (structured or unstructured) – and the

[1] https://www.sigma2.no/content/about-sigma2

discrete difference relationships are used for value approximation. Higher-order solutions allow for better accuracy – but the resulting cost is the requirement for more grid points which increases computational time (Anderson, 1995).

5.3 GOVERNING EQUATIONS

The governing equations used in REEF3D are described in detail by Bihs, Kamath, Alagan Chella, Aggarwal, and Arntsen (2016) – a brief summary of equations and discretization methods are outlined in the sections below.

5.3.1 NAVIER-STOKES EQUATION

Fluid flow is modelled as viscous and incompressible, and is described by using “the three-dimensional Reynolds-Averaged Navier-Stokes equations (RANS), which are solved together with the continuity equation for prescribing momentum and mass conservation” (Bihs et al., 2016). The governing equations described by Bihs et al. (2016) are shown in Equation 12 (conservation of mass) and Equation 13 (RANS) below.

$$\frac{\partial u_i}{\partial x_i} = 0 \tag{12}$$

$$\frac{\partial u_i}{\partial t} + u_j \frac{\partial u_i}{\partial x_j} = \frac{1}{\rho}\frac{\partial p}{\partial x_i} + \frac{\partial}{\partial x_j}\left[(\upsilon + \upsilon_t)\left(\frac{\partial u_i}{\partial x_j} + \frac{\partial u_j}{\partial x_i}\right)\right] + g_i \tag{13}$$

Where:

u	is the velocity averaged over time
ρ	is the fluid density
p	is the pressure
υ	is the kinematic viscosity
υ_t	is the eddy viscosity
g	is the acceleration due to gravity

The 5th-order Weighted Essentially Non-Oscillatory (WENO) finite difference scheme described by Jiang and Shu (1996) is used to discretize the RANS equations in space and the 3rd-order Total Variation Diminishing (TVD) Runge-Kutta (RK) described by Shu and Osher (1988) in time.

5.3.2 LEVEL-SET METHOD

The level-set method introduced by Osher and Sethian (1988) is used to track and represent the free surface during the numerical simulation. The debris flow free surface is defined by the zero-level set in the smooth signed distance function shown in Equation 14 below.

$$\phi(\vec{x}, t)\begin{cases} > 0 \; if \; \vec{x} \in phase \; 1 \\ = 0 \; if \; \vec{x} \in interface \\ < 0 \; if \; \vec{x} \in phase \; 2 \end{cases} \tag{14}$$

The phase 1 material represents the debris flow material, and the phase 2 material represents air in the two-phase flow approximation. The function is coupled to the velocity term in the RANS equation using a convection equation shown below (Equation 15). The Hamilton-Jacobi WENO scheme described by Jiang and Peng (2000) is used to determine spatial discretization.

$$\frac{\partial \phi}{\partial t} + u_j \frac{\partial \phi}{\partial x_j} = 0 \tag{15}$$

5.4 NON-NEWTONIAN RHEOLOGY

5.4.1 BACKGROUND

The dynamics of debris flows can not be adequately described using traditional hydraulic or soil mechanics frameworks; instead, the field of non-Newtonian fluid mechanics can be used to describe behaviour and propagation (Coussot & Meunier, 1996). Rheological constructs aim to model macroscopic fluid behaviour, but do not "rigorously account for complex grain-grain and grain-fluid interactions that dictate the mechanics of flowing debris" (Whipple, 1997).

Debris flows can be modelled as a continuum fluid with non-Newtonian rheological behaviour, where viscous flow behaviour dominates over collisional/frictional behaviour. The Bingham-Plastic model is recognized "as one of the most versatile models for simulating granular flow behavior" (Moriguchi et al., 2009). REEF3D has implemented the Herschel-Bulkley rheology into the code to allow for the analysis of fluids that follow this type of behaviour. As outlined in Section 3.3.1.4, the flow index (n) in Herschel-Bulkley rheology can be adapted to model the Bingham-Plastic rheology ($n = 1$), or more complex shear relations such as: shear thinning behaviour ($n < 1$) or shear thickening behaviour ($n > 1$).

5.4.2 APPLICABILITY

The application of non-Newtonian fluid rheologies depends on the dominant mechanism controlling the flow behaviour. The mode of shear resistance and momentum transport in debris flows depends on shear rate and grain-size distribution – especially fine-grained sediment quantities. Several studies have attempted to quantify the limits of the above dependencies to provide classification of flow behaviour types (Coussot, 1992, 1994; Coussot & Meunier, 1996; Richard M. Iverson, 1993, 1997; Major & Pierson, 1992; Pierson & Costa, 1987; Whipple, 1997).

Based on grain size distribution and deformation rate the dominant forces can be inertial, viscous, or frictional – or a combination/transition of forces during the flow process (Lorenzini & Mazza, 2004). Pierson and Costa (1987) summarize the forces, flow behaviour, and grain support mechanisms as follows:

> *"Rate-independent frictional and viscous forces dominate at lower velocities and in finer grained mixtures; rate-dependent inertial forces dominate at higher velocities and in coarser grained mixtures. As velocity increases, grain-support mechanisms change from low-energy varieties (buoyancy, cohesion, structural support) to progressively higher energy mechanisms (turbulence, dispersive stress, fluidization)."*

Pierson and Costa (1987) proposed a rheological classification based on sediment concentration and flow velocity, and summarize the forces that dominate within the fluid-grain mixture based on the classification. Figure 5-1 below shows the rheological classification.

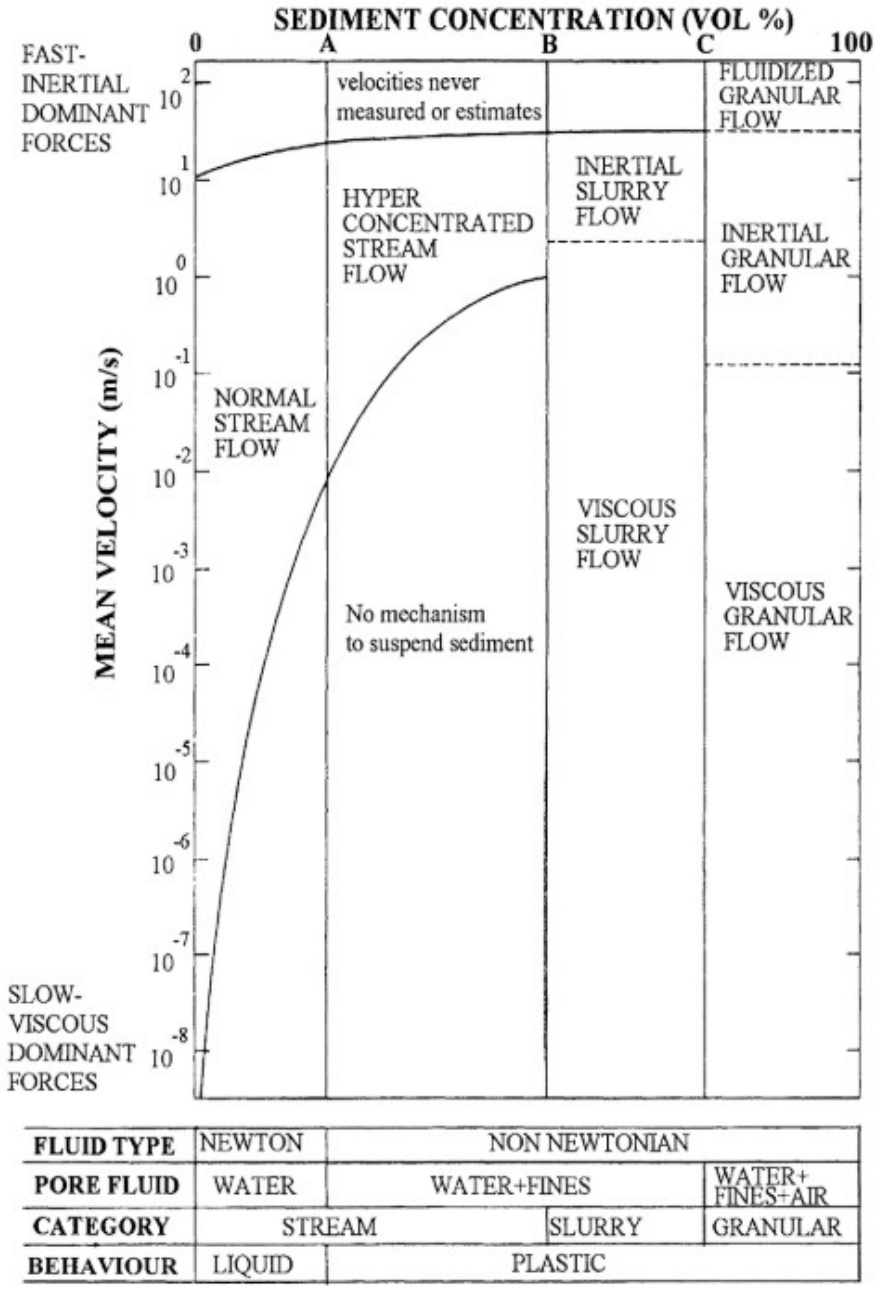

Figure 5-1: Rheological classification by Pierson and Costa (1987)

Based on the classification by Pierson and Costa (1987), the flow material used in the flume tests would plot below (but near) the horizontal boundary between viscous slurry flow and inertial slurry flow (between the vertical

boundaries of B and C). Based on the reported test velocities by Yifru et al. (2017) – it is expected that viscous flow would dominate behaviour, with the possibility of inertial flow behaviour having a larger effect at higher velocities. The rheological classification by Pierson and Costa (1987) does not directly take into account fine-grained sediment quantities.

Although an exact minimum fines content for viscous behaviour is unclear, Coussot (1992, 1994) suggests a minimum value of 10% of the material being of 0.04mm diameter or less for viscous flow behaviour to be dominant – regardless of maximum particle size. Whipple (1997) suggests an approximate minimum value of 15% silt and 1-2% clay – for use of the Bingham rheology model confidently. Kaitna, Rickenmann, and Schatzmann (2007) showed a successful interpretation with a debris flow material containing 9% of total particles less then 0.04mm. The experimental data from the flume testing at NTNU shows approximately 8% of total particles less then 0.04mm. The experimental material will be modelled with the assumption of viscous behaviour (and non-Newtonian fluid rheology), but it is possible there is also frictional/collisional behaviour acting within the flow mass and influencing the results.

Final deposition of a yield-stress fluid can be hard to determine, since once the yield stress is exceeded, the viscous fluid will flow. The fluid will not stop on non-horizontal surfaces and the deposition is not of a solid material, but a very slowly flowing fluid.

5.4.3 INTEGRATION INTO REEF3D

Rheological parameters are defined by the user in the REEF3D code. The apparent viscosity (μ) is determined using the shear stress and shear rate relationship presented in the Herschel-Bulkley equation (Equation 9), and is summarized in Equation 16 below:

$$\mu = \frac{\tau}{\dot{\gamma}} = \frac{\tau_y}{\dot{\gamma}} + K \cdot \dot{\gamma}^{n-1} \tag{16}$$

Kinematic viscosity ($\upsilon = \mu/\rho$) is the input required for the RANS equation – and is "determined locally for each cell every time step since it varies spatially and temporally" (Fornes et al., 2017). To avoid numerical problems when the shear rate is small (and the apparent viscosity value is infinite), a maximum kinematic viscosity value is used (υ_o) instead. The resulting kinematic viscosity input for all shear rates is shown in Equation 17 below:

$$\upsilon = min\begin{Bmatrix} \upsilon_o, \\ \left(\frac{\tau_y}{\dot{\gamma}} + K \cdot \dot{\gamma}^{n-1}\right)/\rho \end{Bmatrix} \tag{17}$$

The scalar shear rate magnitude ($\dot{\gamma}$) is determined from the following shear rate tensor in Equation 18 below (Fornes et al., 2017):

$$\dot{\gamma} = \sqrt{\frac{1}{2}\sum_{i=1}^{3}\sum_{j=1}^{3}\dot{\gamma}_{ij}\dot{\gamma}_{ij}} \tag{18}$$

5.5 SIMULATION PROCEDURE

A short summary of the simulation procedure is outlined in the list below – a more detailed procedure and definition of model input functions are provided in the manuals for REEF3D[2] and DiveMESH[3].

- Model geometry (cartesian coordinates) and cell size are determined and an input file for DiveMESH is created.
- DiveMESH is run to create grid files for geometry.
- An input file for REEF3D is created with a set of functions that define the model parameters and detailed numerical methods, along with requested output data.
- REEF3D is run to simulate the CFD problem defined by the problem inputs.

[2] REEF3D manual: https://reef3d.files.wordpress.com/2018/01/reef3d-userguide_18-01.pdf
[3] DiveMESH manual: https://reef3d.files.wordpress.com/2018/01/divemesh-userguide_18-01.pdf

5.6 MESH SENSITIVITY STUDY

5.6.1 PURPOSE

A mesh sensitivity study was performed using 5 different cell sizes to test how well coarser cell sizes capture the behaviour of finer cell sizes. The purpose of this study is to identify a cell size that balances computational efficiency, which includes model simulation, data transfer from the HPC server, and post-processing, and still captures flow behaviour accurately.

A brief discussion is included with the results to detail the ideal cell size going forward.

5.6.2 MODEL SET-UP

A simplified flume that resembles the testing flume presented in later sections was used to analyze fluid behaviour with different cell sizes. The channel width is constant along the entire flume, there is no cylindrical pillar where the force transducer would be, and there is no additional width in the deposition area. The flow material used in the mesh sensitivity study uses the properties of water. Figure 5-2 below shows the geometry and properties for model.

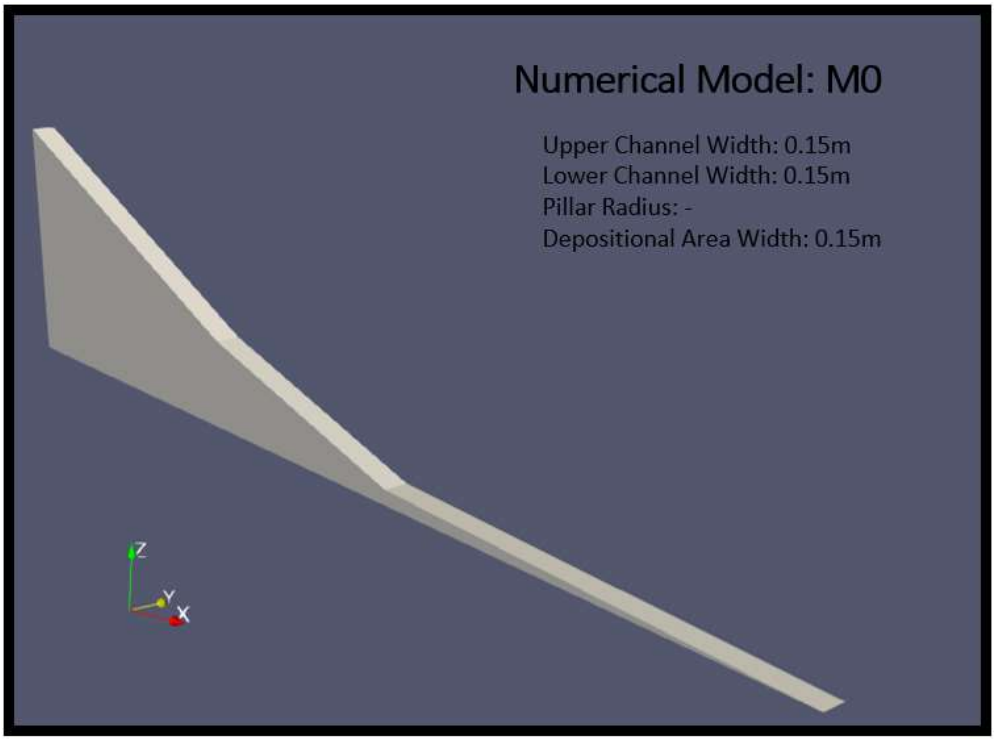

Figure 5-2: Numerical Model: M0

Cell sizes of 0.0010, 0.0025, 0.005, 0.0075, and 0.0100 were tested to test how the change in cell size effects the simulated free surface (height and location). The approximate cell counts for each of the listed cell sizes are shown for the model in Table 5.1 below.

Table 5.1: Cell counts for analysis models

Cell Size (m)	Total Cells
0.0010	2,040,000,000
0.0025	130,560,000
0.0050	16,320,000
0.0075	4,835,556
0.0100	2,040,000

5.6.3 RESULTS AND DISCUSSION

The cell size of 0.0010m was too computationally intensive – and the HPC could not initialize computations due memory exceedance caused by the number of cells in the model. For the other cases the free surface at y = 0.01m was compared to analyze the modeled flow heights and flow front as the simulation progressed. Figure 5-3 below shows the free surface of the flow from 0.3 to 1.5 seconds, in 0.3 second intervals.

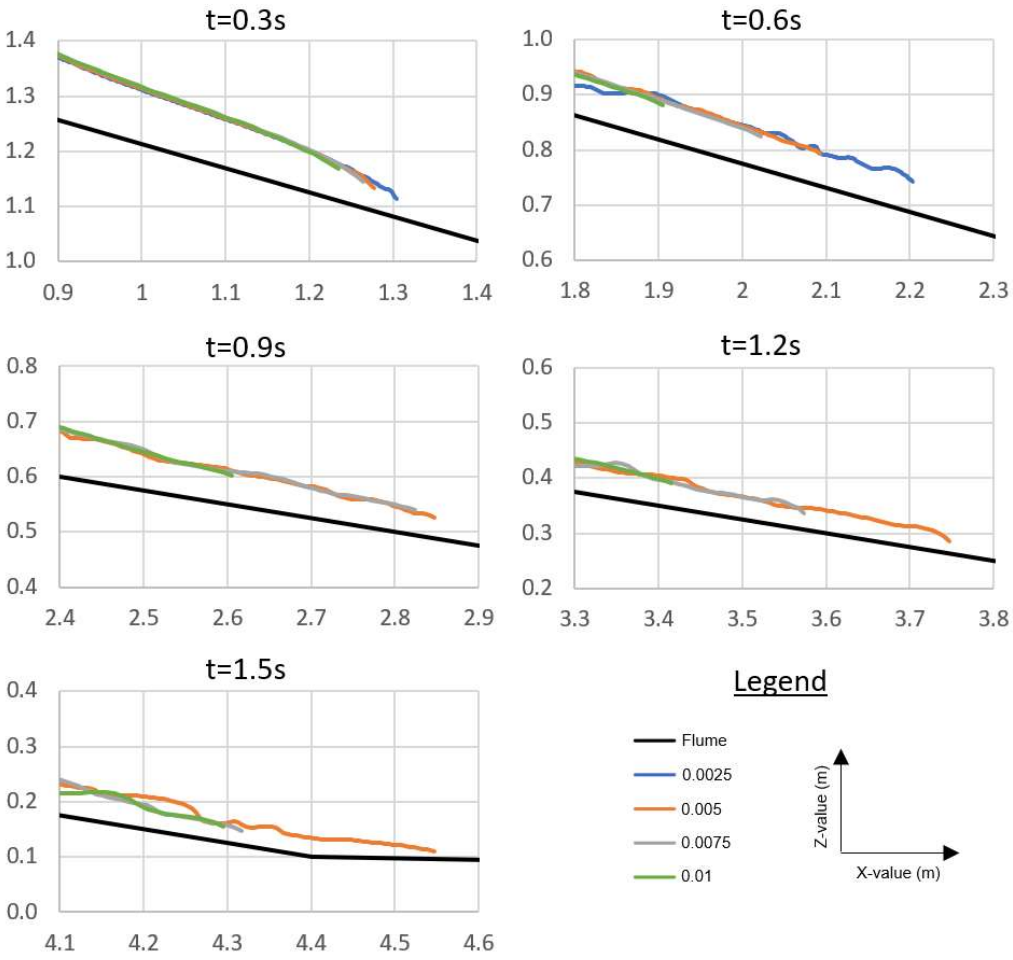

Figure 5-3: Free surface time progression for different cell sizes

The model for the cell size of 0.0025m could be initialized but had numerical issues that could not be resolved at 0.6 seconds of run-time. The free surface at 0.6 seconds clearly shows that the 0.0025m case models spatial variation in flow height the best and models the flow front the most accurately.

Free surface height is modeled well by the 0.0050m, 0.0075m, and 0.0100m cell sizes, but do not have the spatial resolution of the 0.0025m shown at 0.6 seconds. As expected, spatial resolution is reduced as cell size increases.

The coarser cell sizes do not model the flow front as accurately as the 0.0025m cell size at 0.3 and 0.6 seconds. The flow front in the 0.6 second case shows the 0.005m cell value lags the 0.0025m cell size by approximately 10cm, while the 0.0075m and 0.0100m cell sizes lag the 0.0025m case by approximately 20cm and 30cm respectively. As the flow progresses, the flow front can be compared to the 0.0050m cell case. Each of the remaining time intervals shows these coarser meshes unable to model the flow front as accurately as the 0.0050m cell size case. At 1.5 seconds, the 0.0075m and 0.0100m cell size cases are lagging the 0.0050m case by approximately 25cm.

The cell sizes of 0.0075m and 0.0100m are the most computational efficient model but sacrifice accurate representation of the free surface. The cell size of 0.0050m offers the best balance between accurate simulation of the free surface location when compared to the two coarser cell sizes while still being computational efficient. Although the 0.0025m cell size case showed the most accurate free surface representation at 0.3 and 0.6 seconds, simulation time and data files produced by this case were very large, combined with numerical issues make it an unrealistic cell size for further use.

For all the following numerical models, a cell size of 0.0050m was used unless stated otherwise.

6 NUMERICAL MODEL SENSITIVITY STUDY

6.1 BACKGROUND

Rheological and geometry sensitivity studies were performed to analyze the effects of individual values and flume components on modelling results. An increase in model complexity represents an increase in computational resources and run-time, increase in post-processing time, and a greater likelihood of grid and computational errors. To reduce the effect of these factors to a minimum, different numerical models were run to test the influence of different model properties on the results. The individual numerical models also provide insights into debris flow behaviour in a real-world environment, and how material and channel properties can affect flows.

The objective of these individual models is to create a final model that combines computational efficiency and accuracy for final calibration of rheological parameters. The final optimized model and its properties are presented in Section 7.0 following the sensitivity study.

Results and discussion are presented together for each of the individual models and a summary of the major findings in the sensitivity study is presented after presenting all the models and their results.

6.1.1 GENERAL MODEL PARAMETERS AND SET-UP

Models are built in a cartesian coordinate system, the axis and coordinate system shown with an example model is shown in Figure 6-1 below.

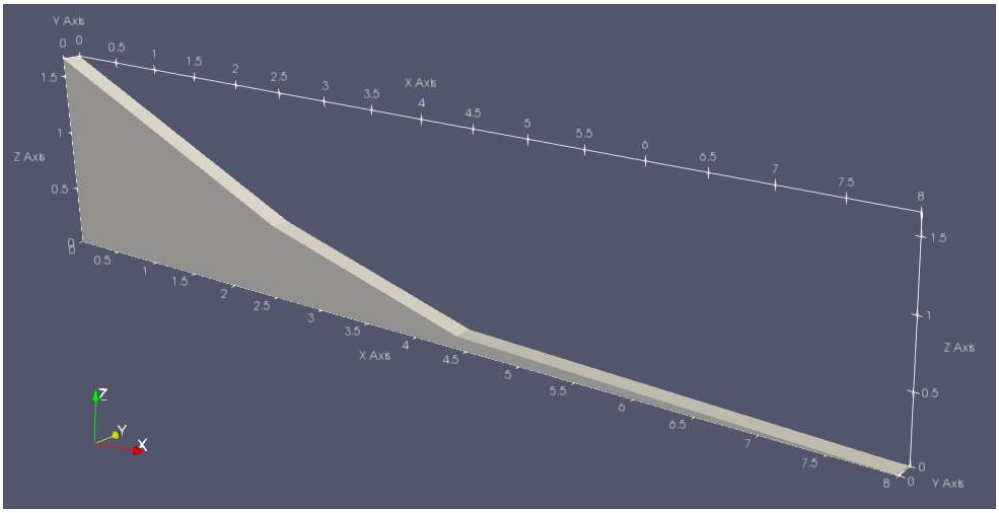

Figure 6-1: Example model with cartesian grid

All 3-D models are built as half-flume models where y=0 acts as a symmetry plane in the numerical code. Based on the 0.005m cell size, a numerical flume geometry was made to best match the laboratory flume. A cross section of the numerical model compared to the laboratory model is shown in Figure 6-2 below.

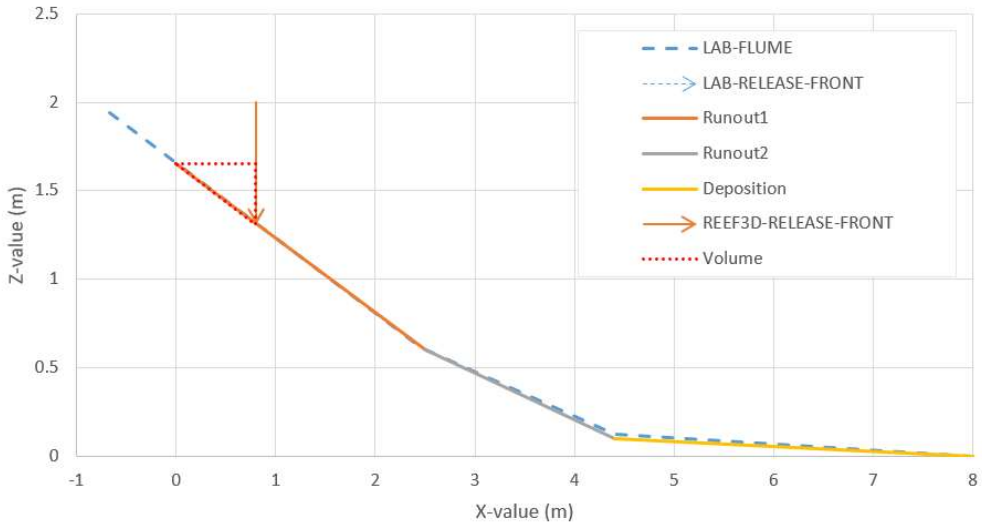

Figure 6-2: Comparison of Lab flume geometry to numerical model geometry

A summary of the 4 different models in the sensitivity study are shown in Table 6.1 below.

Table 6.1: List of numerical models

Numerical Model		Change in Channel Width	Upper Channel Width (m)	Lower Channel Width (m)	Pillar	Pillar Width (m)	Deposition Area	Deposition Area Width (m)
3-D	M1	×	0.15		×		✓	0.15
	M2	✓	0.30	0.15	×	-	×	-
	M3	×	0.15		✓	0.035	✓	0.15
	M4	×	0.15		×	-	✓	0.60

Results in numerical models M2, M3, and M4 are compared to results in the base case established in model M1.

6.1.2 MATERIAL PROPERTIES

A bulk density of 1957 kg/m^3 was used for all flow simulations based off an average of the individual bulk densities measured for the 9 individual tests. An average fluid volume of 30.4L based from physical modelling tests P4-2, P5, and P6 was used for all numerical simulations.

6.1.3 POST PROCESSING AND DATA ANALYSIS

Paraview 5.5.0 is open-source visualization software that was used to process and export CFD data from the simulations. Velocity and flow thickness measurements in the CFD simulations are found by sampling a section normal to the flow direction and perpendicular to the flume surface at the locations of the sensors and pillar at every time step. The properties at the node points

along the section are exported and processed to find the flow velocity and thickness at each time-step.

Flow thickness in the CFD simulations is found by taking the exported dataset and analyzing the individual ϕ values for each point record. The ϕ value equal to 0 represents the free surface – as outlined in the level set method in Section 5.3.2. The transition between positive and negative ϕ value is identified, and a linear interpolation is performed to find the location of the free surface. The free surface is found at the pillar and sensor locations, and the thickness normal to the flume is calculated based on the coordinate data.

Velocity was found by Yifru et al. (2017) in the physical testing by analyzing the flume experiment video to manually track velocity values prior to impact of the pillar. This method is harder to perform for each CFD simulation since time steps are typically 0.2 seconds in length, and this method is time consuming and subjective, so it is best to come up with an objective velocity measurement from the simulation node data that best matches this.

To find the best match to the spatial velocity estimates done in the physical testing, the velocity profile of the flow mass was analyzed to find which node data best matches the general behaviour of the fluid mass. There is a large velocity variation between the flume interface and the fluid core in the simulation node data. A cross-section of a flowing mass is shown in Figure 6-3 below showing the spatial variation in velocity of the flowing mass.

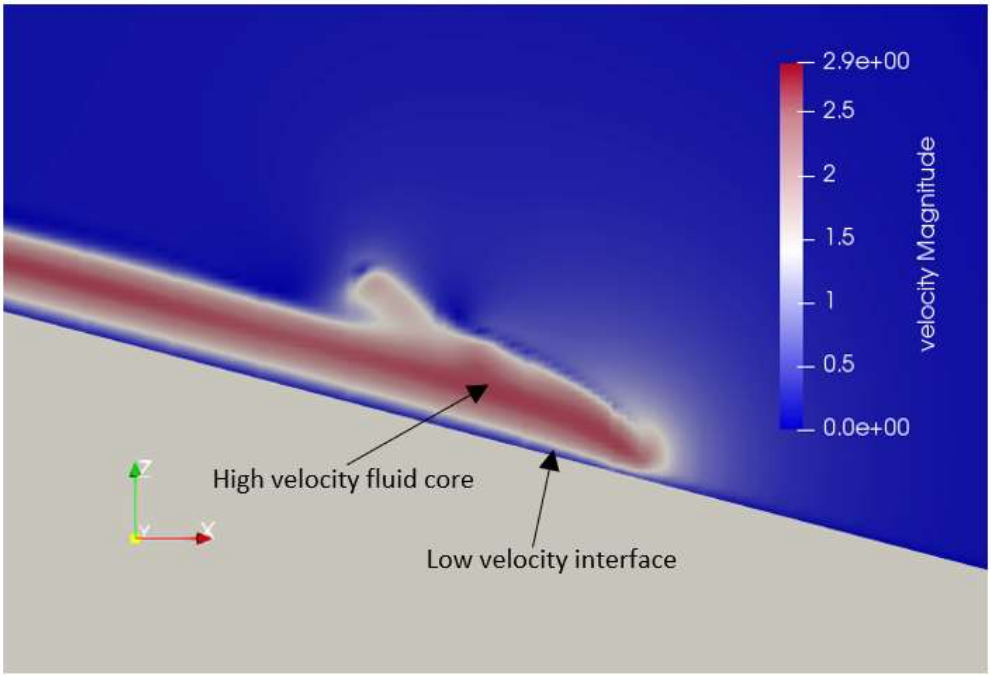

Figure 6-3: Spatial velocity of flowing fluid mass

The fluid mass was tracked between the Sensor-1 and pillar location in the same way that was done in the physical experiment to find an approximate fluid mass velocity. This approximate fluid velocity was compared to the fluid node data, and it was found taking an average of the entire fluid column while only excluding the velocity at the interface node (which is near zero) gave a good representation of the velocity behaviour of the flow front. The results from this analysis are shown in Table 6.2 below.

Table 6.2: Velocity measurements from manual tracking vs. node data

Manual Flow Tracking (Velocity at Pillar)		Comment
v (m/s)	2.07	-
Node data from Pillar Location		Comment
v_{MAX} (m/s)	2.78	Maximum velocity (single node)
v_{AVG} (m/s)	1.77	Average velocity of entire fluid column
v_{AVG-1} (m/s)	**2.06**	**Average velocity, excluding interface value**

Detailed model set-up and results for the numerical models is presented in the sections below.

The magnitude of flow height at the upstream and downstream locations is more important then calibrating the exact flow timing to the physical modelling data. The aim of the flow height progression plots presented in the following sections are to show the change of magnitude with time compared to the magnitudes of the physical testing data. The simulation times appear to reach the flow sensors sooner then the physical testing, but the videos of the physical testing show flow behaviour more like that of the simulated tests then the timing data. There is no time and video sync, so it is hard to subjectively adjust the physical testing time data to better represent the true timing of physical testing. Test P6 represents the most accurate timing compared to the video records.

6.2 M1: Parameter Sensitivity and Base Case

6.2.1 Purpose

Numerical model M1 was used to investigate how rheological parameters affect the flow height at upstream and downstream locations, impact velocity, and runout length. Based on results from the sensitivity study, a base case is proposed to be used for comparison to the sensitivity studies that vary flume geometry to the results presented in M1.

6.2.2 Model Set-up

The first model (M1) does not include additional width in the deposition area, flume width reduction, or the force pillar. Figure 6-4 below shows the geometry and properties for model M1.

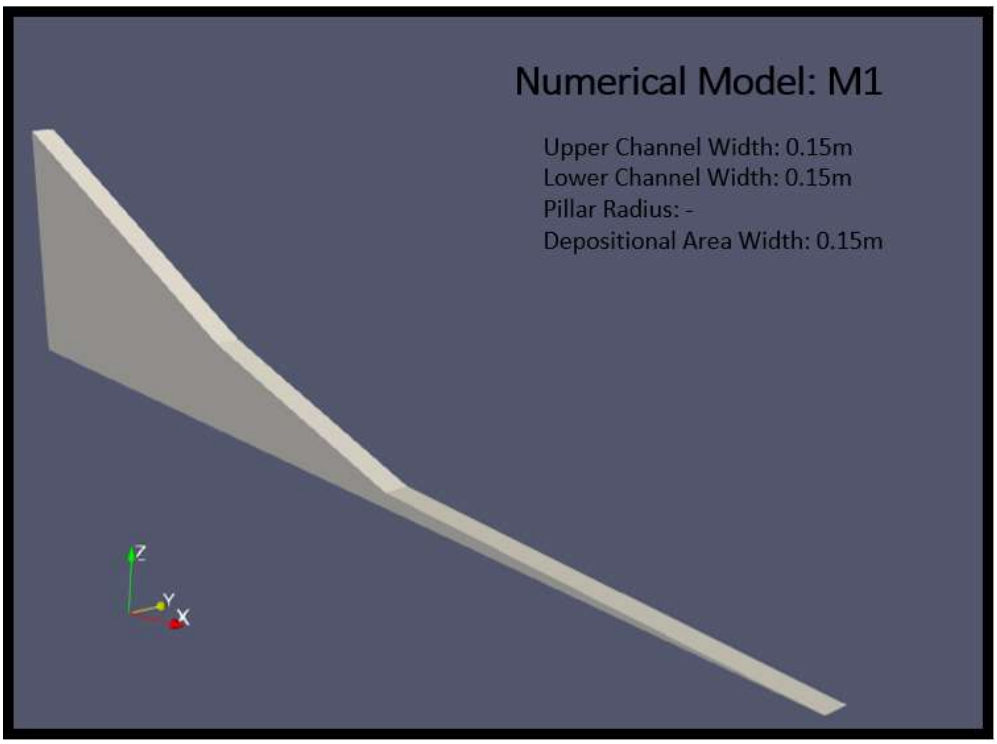

Figure 6-4: Numerical Model: M1

Herschel-Bulkley rheological parameters were varied to find the effect on the flow properties and behaviour. Initial models varied yield stress (τ_y) and kept the consistency factor (K) and flow index (n) at a value of 1. Using the lowest yield stress value (0.01Pa was used instead of 0Pa to avoid numerical issues), the consistency factor was then varied to show the change in behaviour. Finally, the flow index was reduced to show the effect of shear-thinning behaviour on the flow mass. Table 6.3 below shows the models that were run for the parameter sensitivity analysis.

Table 6.3: Rheological parameters for sensitivity analysis

Model	K [Pa·s^n]	n [-]	τ_y [Pa]
M1-1	1.0	1.0	0.01
M1-2	1.0	1.0	5.00
M1-3	1.0	1.0	10.00
M1-4	0.5	1.0	0.01
M1-5	1.5	1.0	0.01
M1-6	1.0	0.8	0.01

Figure 6-5 below shows the shear stress versus shear rate plot for the rheological parameters for the sensitivity analysis models.

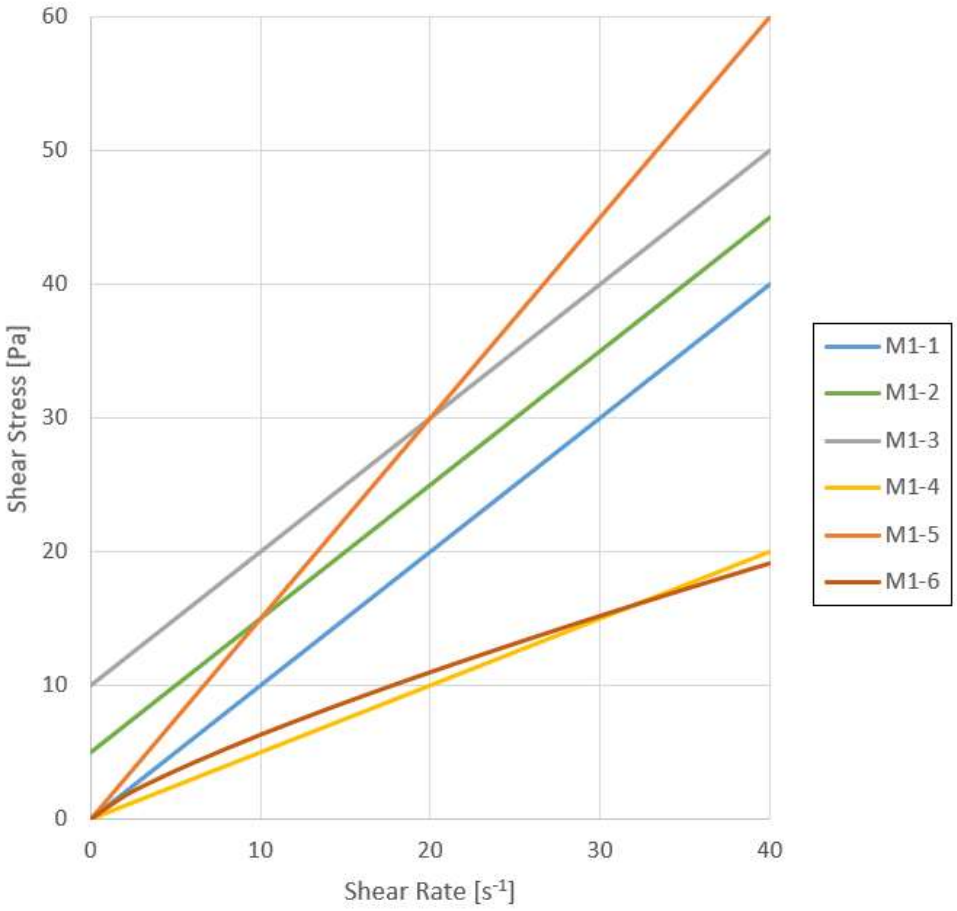

Figure 6-5: Shear stress vs. shear rate plot for sensitivity analysis models

Figure 6-6 below shows the resulting kinematic viscosity versus shear rate plot for the rheological parameters for the sensitivity analysis models.

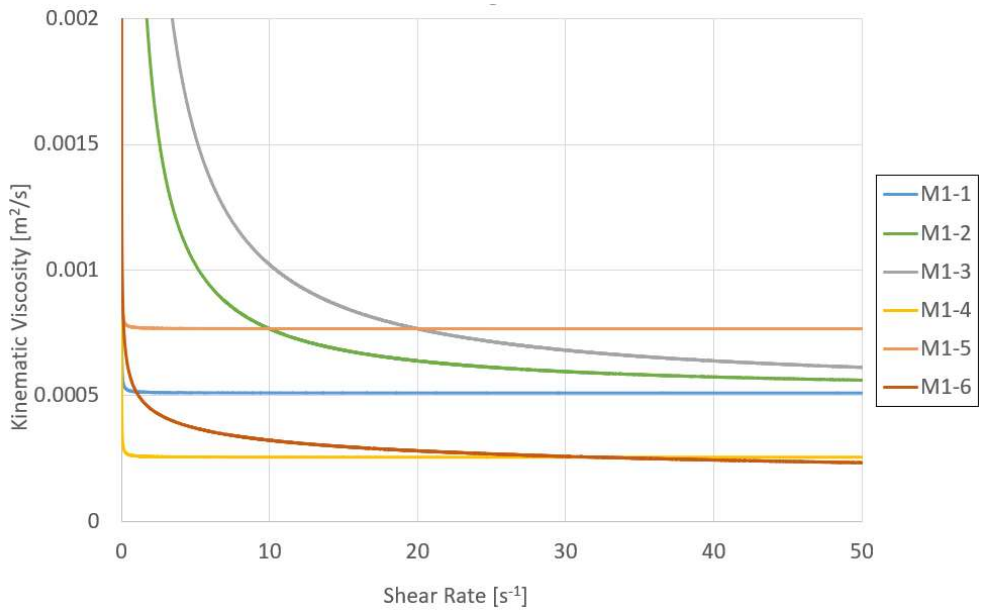

Figure 6-6: Kinematic viscosity vs. shear rate

Model M1-1 was run for 6 seconds and the remaining models were simulated for 3 seconds to reduce post-processing time – 3 seconds of data still gives the magnitude of flow thickness at the flow front and an idea of the general behaviour of the numerical model. Results were printed at a time step of 0.1 seconds for M1-1, and 0.2 seconds for the remaining models.

6.2.3 RESULTS AND DISCUSSION

The velocity at the pillar location (impact velocity) and runout length for each of parameter sensitivity cases are presented in Table 6.4 below.

Table 6.4: Velocity at impact and runout for sensitivity cases

Model	Impact Velocity (m/s)	Runout (cm)
Flume	**2.57**	**199.1**
M1-1	2.06	198.3
M1-2	1.90	128.8
M1-3	1.50	131.3
M1-4	2.53	280.3
M1-5	1.33	180.3
M1-6	2.94	298.3

Runout values are confined for the parameter sensitivity cases (0.15m width) so there is no allowance for additional flow spreading once the flow reaches the deposition area. The impact velocity in model M1-4 best matches the physical modelling average, while model M1-1 best matches the average runout value.

The flow height at the upstream flow height sensor location was extracted from the simulation data and is plotted in Figure 6-7 below.

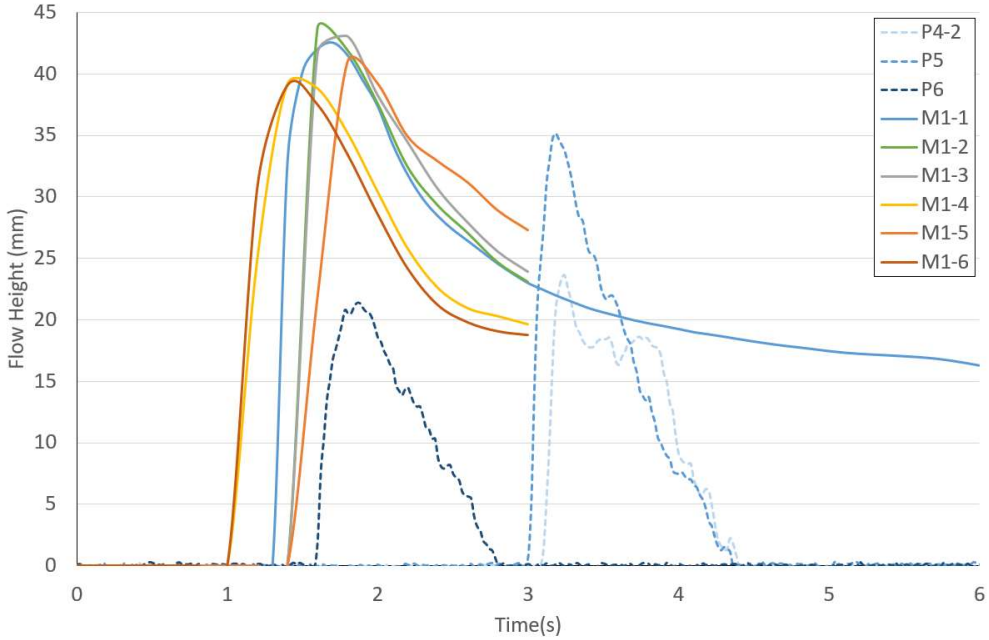

Figure 6-7: M1 - Upstream flow height

The flow height at the downstream flow height sensor location was extracted from the simulation data and is plotted in Figure 6-8 below.

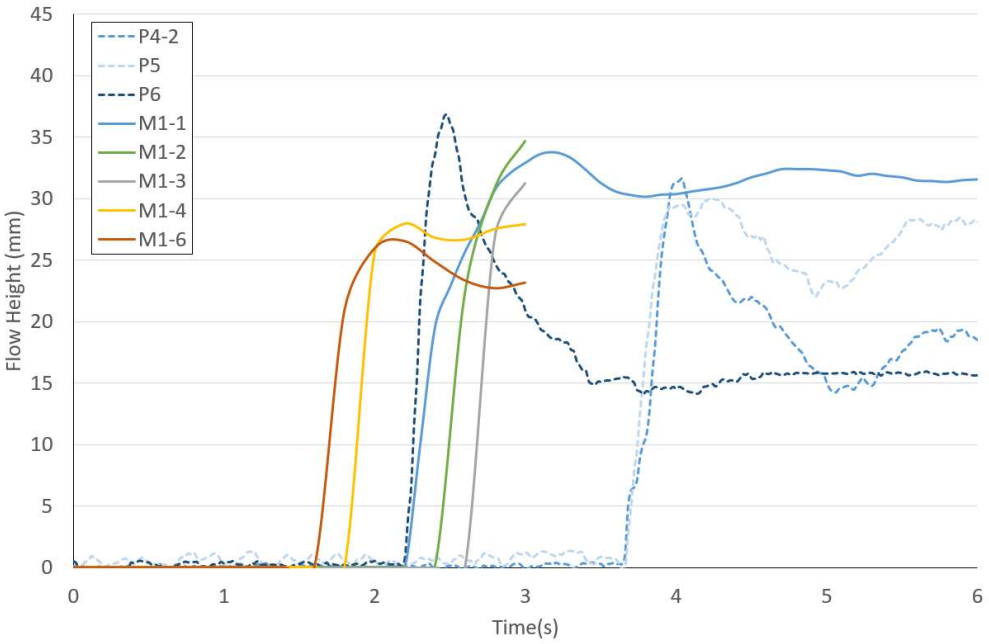

Figure 6-8: M1 - Downstream flow height

There are slight variations in upstream flow thickness, but overall the values show consistently thicker flow height by approximately 10-20mm when compared to the physical testing values (P4-2, P5, P6).

Trends in the downstream flow height data is hard to discern with only 3 seconds of data, but the flows with lower kinematic viscosity values (M1-4 and M1-6) showed thinner deposit values, while the other cases showed thicker deposit values. M1-5 is not displayed since there was no recorded flow height in the simulation at or before 3 seconds. The simulations shown in Figure 6-8 demonstrate a good match when compared to the minimum and maximum values observed in the physical testing.

Ancey (2007) describes the yield stress in a fluid mechanics framework as the shear stress required for flow of the mass – in the laboratory testing the mass was liquefied using a hand mixer, so the low values chosen for the sensitivity analysis provide an accurate starting point for the analysis. The lowest value

($\tau_y = 0.01Pa$) in M1-1 appears to show the best initial match when compared to models M1-2 and M1-3 which show slower flows with lower runout lengths.

Shear thinning behaviour in model M1-6 shows higher velocity and runout values then the physical testing. At higher shear rates ($\dot{\gamma} > \sim 30s^{-1}$), this case has the lowest kinematic viscosity value, which results in the fastest flow. Expectedly, this simulation also shows the thinnest flow thickness at both sensor locations.

Impact and residual forces could not be calculated for these simulations without a pillar in the flow path to cause a pressure differential in the node data at the pillar location.

The flow simulated by the rheological properties used in M1-4 show similar impact velocity at the pillar location, but the flow runout length is approximately 80cm longer then observed in the experimental data. The flow simulated by the rheological properties in M1-1 show almost exact runout length values compared to the flume testing, but the impact velocity is lower then what is observed in the physical testing. The rheological properties used in M1-1 will be used as a base case for the following geometry sensitivity studies to find the general effects the geometry components have on the flow behaviour.

6.3 M2: Channel Width Reduction

6.3.1 Purpose

Numerical model M2 investigates the effect on upstream flow height and impact velocity caused by the channel width reducing to half its initial width.

The physical model includes this channel width reduction, but the numerical model would be more efficient if the channel width reduction could be excluded. Including the channel width reduction increases the cell count by approximately double.

6.3.2 MODEL SET-UP

The initial width at the flow release point is 0.3m (which with the half-flume model represents the 0.6m width of the mixing box used in the physical experiment). The width reduces to 0.15m at the transition point between Runout1 and Runout2 (x = 2.5m) (see Figure 6-2 for flume geometry details). The depositional area is not included in the model to increase computational efficiency. Figure 6-9 below shows the geometry used for model M2.

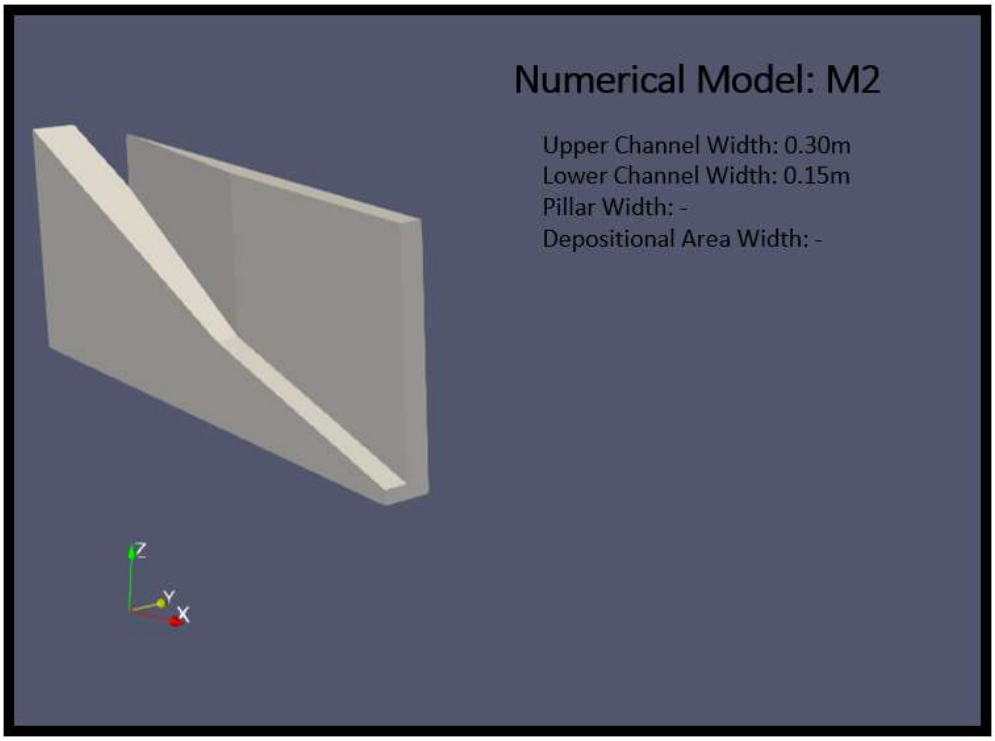

Figure 6-9: Numerical Model: M2

The resulting difference in starting geometry height caused by keeping the flow volume constant between models is 0.085m, Figure 6-10 below shows the change in start flow height caused by widening of the upper flume.

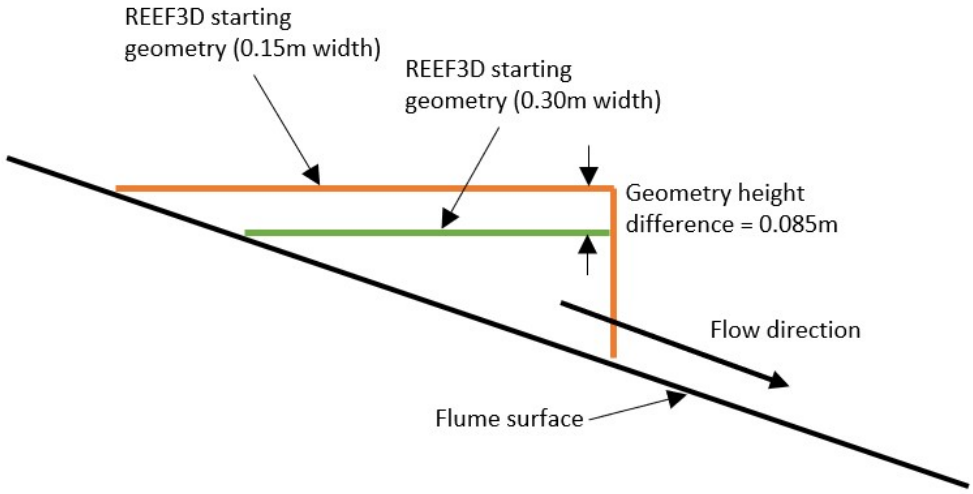

Figure 6-10: Geometry height difference caused by widening upper flume while still using the same flow volume

The results from the base case (M1-1) are presented alongside the simulation with the same rheological properties and M2 model geometry (M2-1). The rheological properties used for M2-1 are shown in Table 6.5 below.

Table 6.5: Model parameters

Model	K [Pa·s^n]	n [-]	τ_y [Pa]
M2-1	1.0	1.0	0.01

Model M2-1 was run for 4 seconds and results were printed at time steps of 0.2 seconds.

6.3.3 RESULTS AND DISCUSSION

Table 6.6 below shows the change in velocity at the pillar location (impact) caused by the reduction of the channel width in the upper flume.

Table 6.6: M2-1 Results

Model	Impact Velocity (m/s)	Runout (cm)
Flume	**2.57**	**199.1**
M1-1	2.06	198.3
M2-1	1.73	-
Change	**-0.33**	-

The upstream flow height for the base case (M1-1) and for the modified flume (M2-1) are shown in Figure 6-11 below.

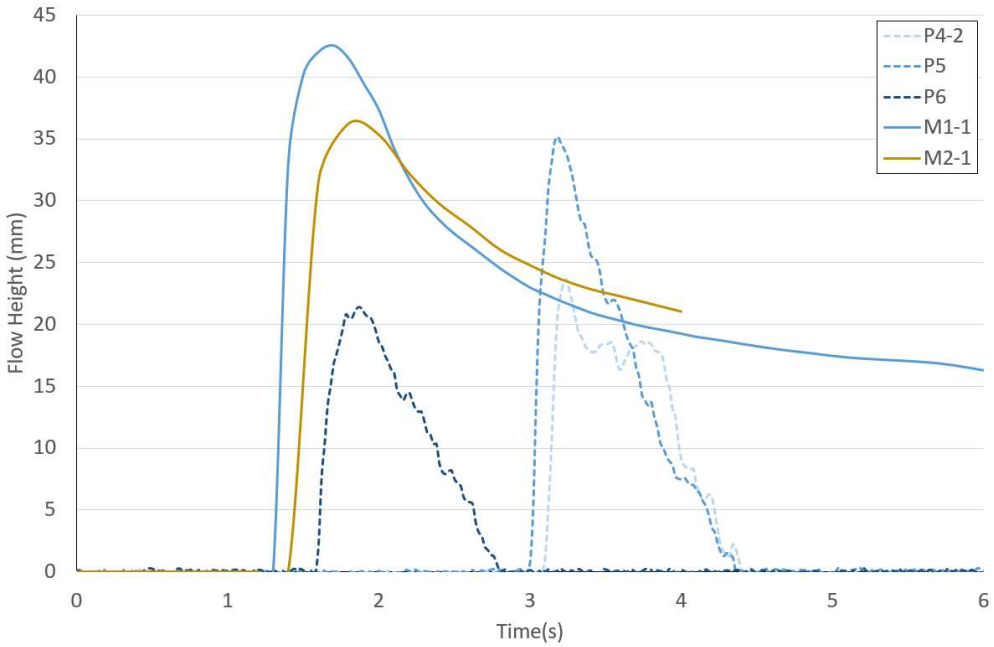

Figure 6-11: M2 - Upstream flow height

Overall, the width reduction in the upper flume causes a slight delay in flow arrival time at the upstream flow height sensor, an approximate decrease of 6-7mm in upstream flow height, and a velocity reduction of 0.33m/s at the pillar location. The inclusion of channel width reduction used in the physical modelling is important for accurate calibration of the numerical model.

6.4 M3: CYLINDRICAL PILLAR

6.4.1 PURPOSE

Model M3 includes a cylindrical pillar to represent the effect of the force transducer on the flow. The main purpose of this model is to analyze the effect of the pillar on the downstream flow height and total runout length.

6.4.2 MODEL SET-UP

The force transducer has a radius of 0.375m, but due to the mesh size of 0.005m the pillar radius was reduced to 0.35m to avoid meshing issues in the numerical model. The entire width of the flume is 0.15m, and the model includes the depositional area (albeit only 0.15m wide).

Figure 6-12 below shows the geometry for model M3.

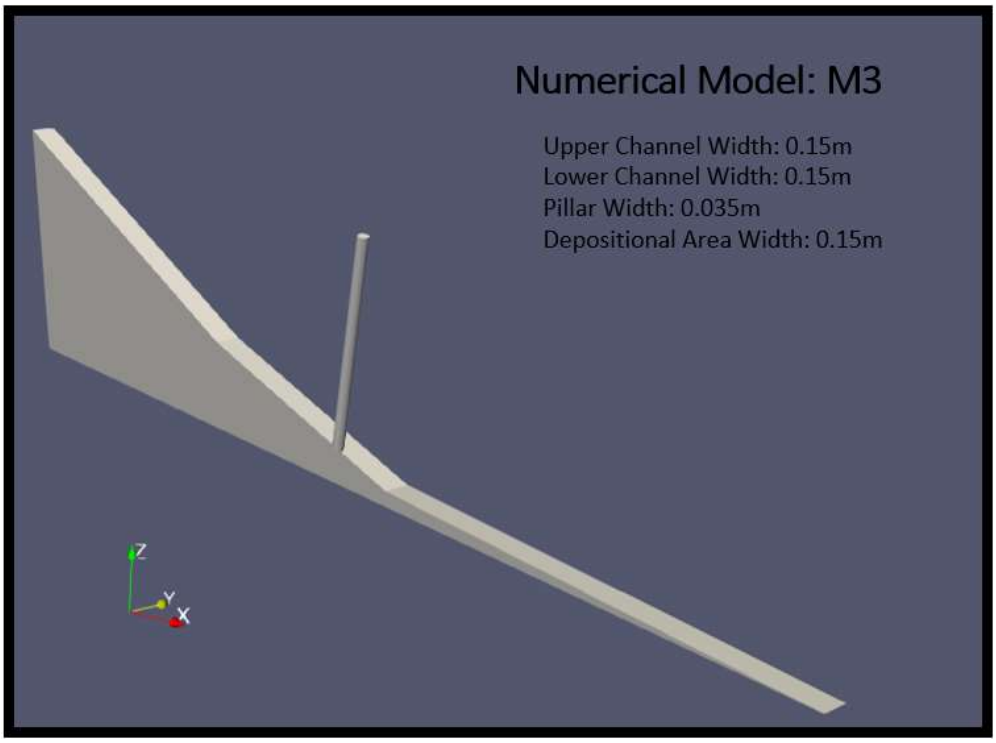

Figure 6-12: Numerical Model: M3

The results from the base case (M1-1) are presented alongside the simulation with the same rheological properties and M3 model geometry (M3-1). The rheological properties used for M3-1 are shown in Table 6.7 below.

Table 6.7: Model parameters

Model	K [Pa·s^n]	n [-]	τ_y [Pa]
M3-1	1.0	1.0	0.01

Model M3-1 was run for 6 seconds and results were printed at time steps of 0.2 seconds.

6.4.3 RESULTS AND DISCUSSION

Figure 6-13 shows the initial impact of the flow, and the flow routing caused by the pillar. The simulated flow is contoured based on velocity magnitude.

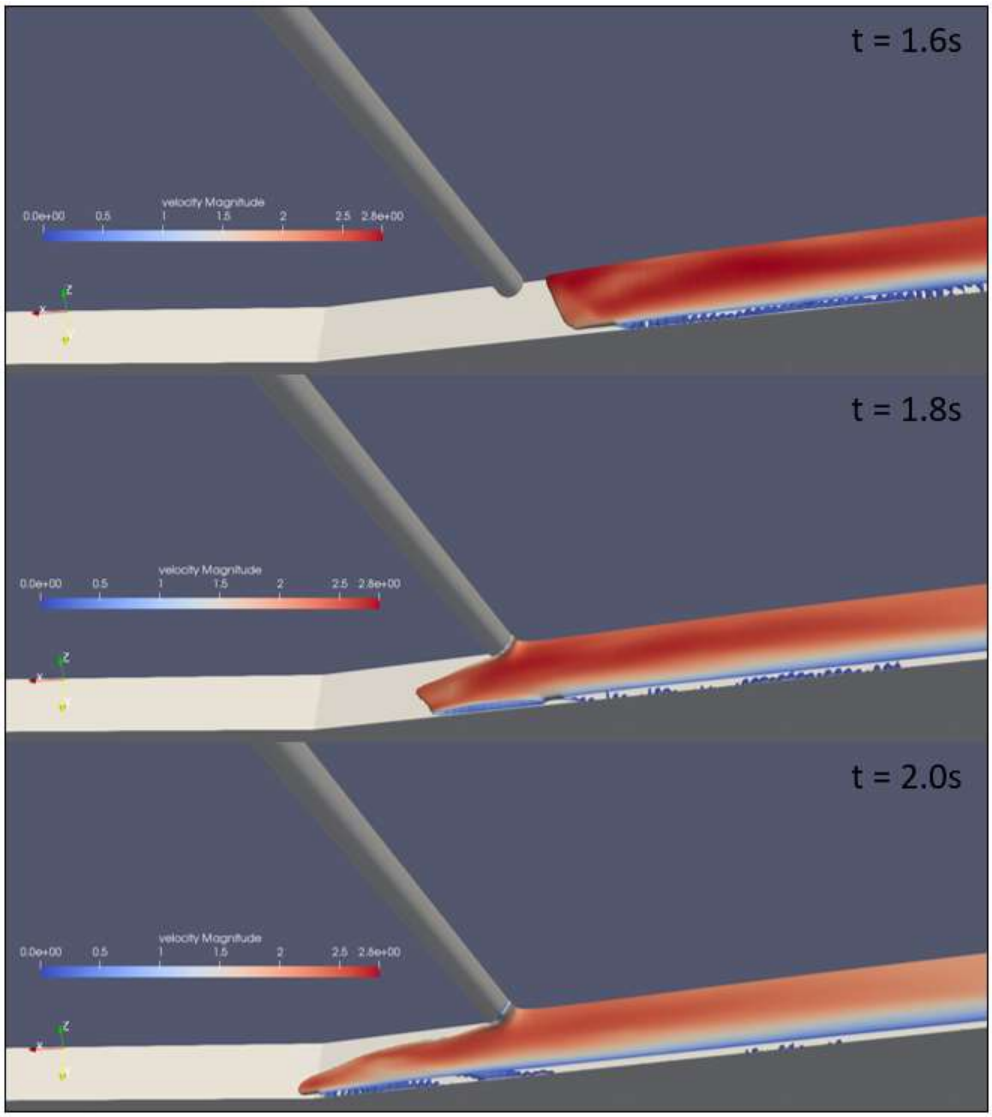

Figure 6-13: Flow impact on cylindrical pillar

The runout was measured and is reported in Table 6.8 below.

Table 6.8: M3-1 Results

Model	Impact Velocity (m/s)	Runout (cm)
Flume	**2.57**	**199.1**
M1-1	2.06	198.3
M3-1	-	70.3
Change	-	**-128.0**

The downstream flow thickness for the M1 case (M1-1) and M3 case (M3-1) are presented in Figure 6-14 below.

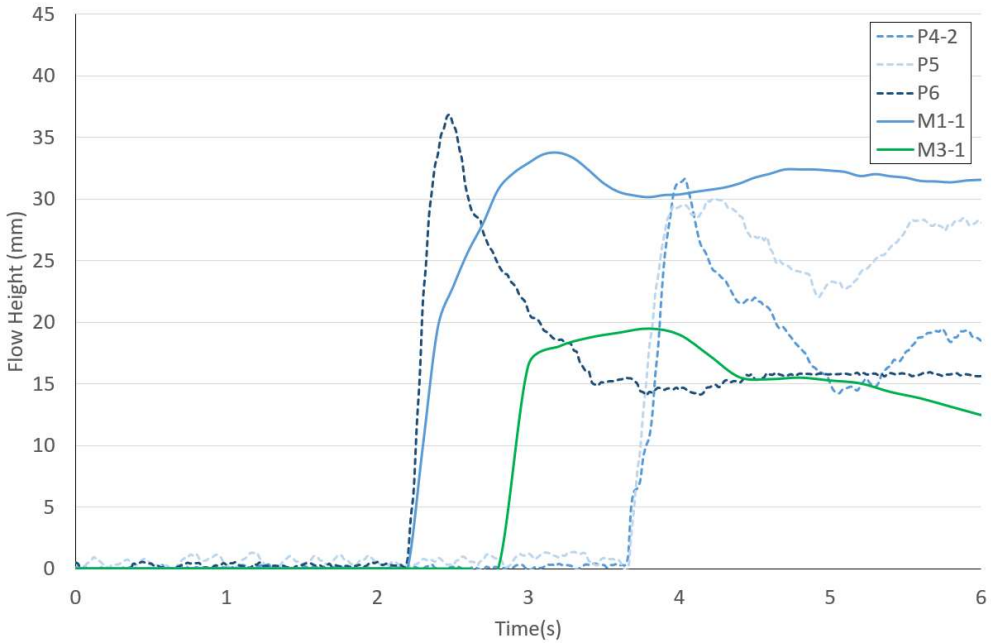

Figure 6-14: Downstream flow thickness vs. simulation time

The cylindrical pillar has a large affect on not only the flow runout, but also the downstream flow thickness magnitude and time of arrival. Runout is reduced by 128cm when compared to the base case (M1-1). Downstream flow heights reduce at the centreline because of the flow routing caused by the cylindrical pillar and more material is forced to deposit early due to energy

dissipation caused by the rigid pillar. Simulated downstream flow height in M3-1 is reduced by approximately 15mm when compared to M1-1. Downstream flow height in M3-1 do not match the physical modelling tests with the current rheological parameters.

6.5 M4: INCREASING DEPOSITION AREA WIDTH

6.5.1 PURPOSE

Model M4 has a deposition area of 0.60m to analyze the effect of spreading on the runout length. The physical model has a full width of 2.5m in the depositional area, with 1.25m on each side of the flume centreline, but none of the flume tests spread more then 0.60m on either side of centreline.

6.5.2 MODEL SET-UP

The deposition area length was reduced by 1.6m to counter the increase in cell count caused by the model width increase. The runout length for this model is 1.8m.

Figure 6-15 below shows the geometry and properties for model M4.

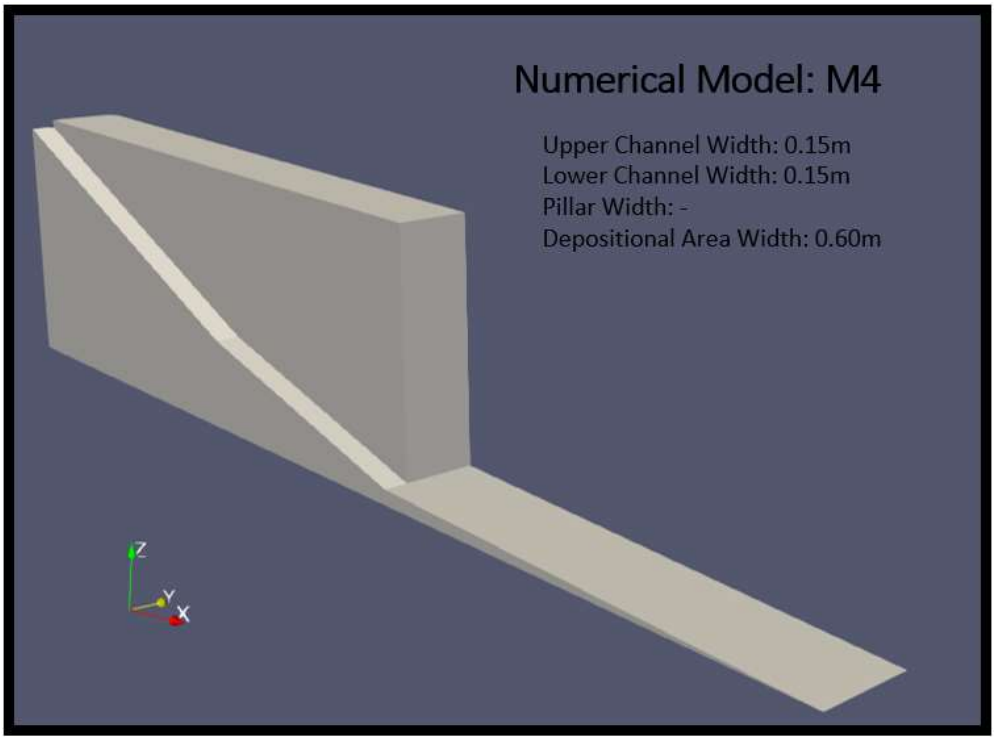

Figure 6-15: Numerical Model: M4

The results from the base case (M1-1) are presented alongside the simulation with the same rheological properties and M4 model geometry (M4-1). The rheological properties used for M4-1 are shown in Table 6.9 below.

Table 6.9: Model parameters

Model	K [Pa·s^n]	n [-]	τ_y [Pa]
M4-1	1.0	1.0	0.01

Model M4-1 was run for 6 seconds and results were printed at time steps of 0.2 seconds.

6.5.3 RESULTS AND DISCUSSION

The runout was measured and is reported in Table 6.10 below.

Table 6.10: M4-1 Results

Model	Impact Velocity (m/s)	Runout (cm)
Flume	**2.57**	**199.1**
M1-1	2.06	198.3
M4-1	-	45.3
Change	-	**-153.0**

A plot of the downstream flow thickness could not be produced because files exported from the simulation for use in post-processing software Paraview were too large and caused the software to crash. A comment on the ideal file sizes for use in Paraview is outlined in Section 8.4.

The inclusion of a wider deposition area allows the flow to enter an unconfined zone and deposit earlier. This behaviour is typical of debris flows – unconfined flows deposit earlier then confined flows.

6.6 CONCLUSIONS

A list of the major conclusions found in the sensitivity study are presented in the list below:

- Rheological Parameters:
    - In general, reduction of kinematic viscosity produces faster, thinner flows, with longer runout.
    - In the Bingham-Plastic model ($n = 1$), at high shear rates the kinematic viscosity values are constant for the range of yield stresses presented, but at low shear rates the $5Pa$ and $10Pa$ values shown higher viscosities respectively. The yield stress value of $0.01Pa$ creates a model that has approximate

Newtonian fluid behaviour (constant viscosity at all shear rates).

- Low shear stress values are required to mimic pre-mixing of flow mass before it is released into the flume (liquefied behaviour).
- The consistency parameter determines the slope of the rheological curve.
- Shear thinning behaviour ($n < 1$) is characterized by a continuous reduction in kinematic viscosity with shear rate.

- Numerical geometry:
  - Reduction of channel width in the upper flume caused changes to the flow behaviour at the upstream flow height sensor. Model M2-1 showed approximately 6-7mm reduction in flow height thickness when compared to M1-1 which had a constant 0.15m flume width. Velocity at the pillar location (impact) reduced by 0.33m/s. The channel width reduction affects the results of the laboratory tests as shown in the numerical analysis.
  - Energy dissipation caused by rigid pillar is significant to downstream flow thickness and runout length. Model M3-1 showed 128cm reduction in runout length when compared to M1-1 which had no pillar in the flow path. The inclusion of the pillar in final calibration necessary to model the downstream effects of the energy dissipation.
  - Confined flows runout further and can not provide a good calibration to unconfined deposition are in the flume geometry. The numerical model must allow flow spreading for an accurate calibration. Model M4-1 showed 153cm reduction in

runout length when compared to M1-1 which had a confined deposition area (0.15m).

All the analyzed geometry elements had a noticeable affect on the flow simulation results, and the final calibration should incorporate each of them if numerically possible. Due to the reduction in runout caused by models M3-1 and M4-1, the base case no longer provided a match in runout length when compared to the average runout length from the physical modelling results. Model M1-4 showed similar impact velocity at the pillar location, but approximately an extra 80cm of runout in the simplified M1 model when compared to the experimental data. Based on the above conclusions, the rheological properties used in M1-4 provide a good starting point for final calibration.

7 NUMERICAL MODEL CALIBRATION

7.1 PURPOSE

The findings from the previous numerical models was used to build a final model with the best balance of computational efficiency and model accuracy – this model is referred to as model M5. The rheological parameters were refined based on the results from M1, where a variation to rheological parameters was performed to find the change to flow behaviour.

As mentioned in Section 6.1.3, the plots showing flow height progression with time only aim to show the change of magnitude with time compared to the magnitudes of the physical testing data. The timing provided in the physical testing is inaccurate and does not match the video of the same testing. Experimental test P6 appears to have the best match of experimental video timing to the resulting timing data.

The pillar force will be compared to the force transducer value by integrating fluid pressure on the impact side of the pillar to find the impact force. The force and discharge relationship presented by Yifru et al. (2017), and summarized in Section 4.3, will also be compared to the calculated pillar force.

The goal of final calibration is to attempt to use the non-Newtonian rheology models to match the behaviour found in the experimental flume. The flow height progression at the upstream and downstream sensor locations, impact velocity and impact force, and the flow runout length, along with general flow behaviour were all considered for calibration of the numerical model.

7.2 MODEL SET-UP

The final numerical model includes the channel width reduction presented in M2, where the upper flume width reduces from 0.3m to 0.15m. The model also includes the pillar analyzed in model M3. Due to file size (caused by the large increase in cell count), a full 0.6m depositional area width could not be used, so instead 0.3m was used to find calibration. Depositional area length was also reduced by 0.9m (allowing for 2.3m of possible runout length) to reduce the cell count in the models.

Figure 7-1 below shows the geometry and properties for model M5.

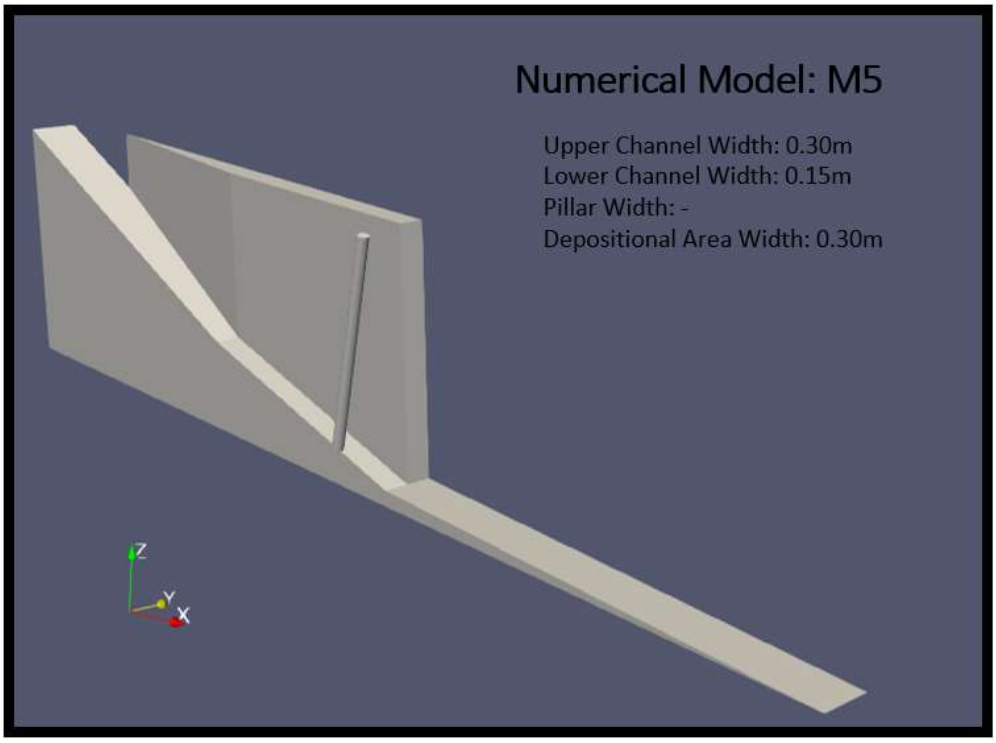

Figure 7-1: Numerical Model: M5

Based on results from the sensitivity analysis, the yield stress (τ_y) was kept at 0.01Pa for all calibration analyses. Table 7.1 below shows the parameters used in the rheology models for this analysis. Models with numerical issues that did

not produce reliable free surface data are noted and could not be analyzed further (numerical issues are discussed further in Section 8.3).

Table 7.1: Model parameters

Model	K [Pa·s^n]	n [-]	τ_y [Pa]	Numerical Issues
M5-1	0.5	1.0	0.01	×
M5-2	1.0	0.8	0.01	×
M5-3	0.3	1.0	0.01	×
M5-4	0.2	1.0	0.01	×
M5-5	0.1	1.0	0.01	✓
M5-6	1.0	0.6	0.01	✓

Simulations using the M5 geometry were run for 8 seconds and results were printed at time steps of 0.2 seconds. Simulation plots only show 6 seconds of data – which is a good representation of the flow behaviour. Runout lengths at 8 seconds match those at 6 seconds.

7.3 RESULTS

The impact velocity and runout length were measured and are reported in Table 7.2 below.

Table 7.2: M5 Results

Model	Impact Velocity (m/s)	Runout (cm)
Flume	**2.57**	**199.1**
M5-1	2.49	99.3
M5-2	2.47	81.3
M5-3	2.59	117.3
M5-4	2.67	153.3

A visualization of the impact velocity data showing the mean and standard deviation values for the flume experimental data are shown in Figure 7-2 below.

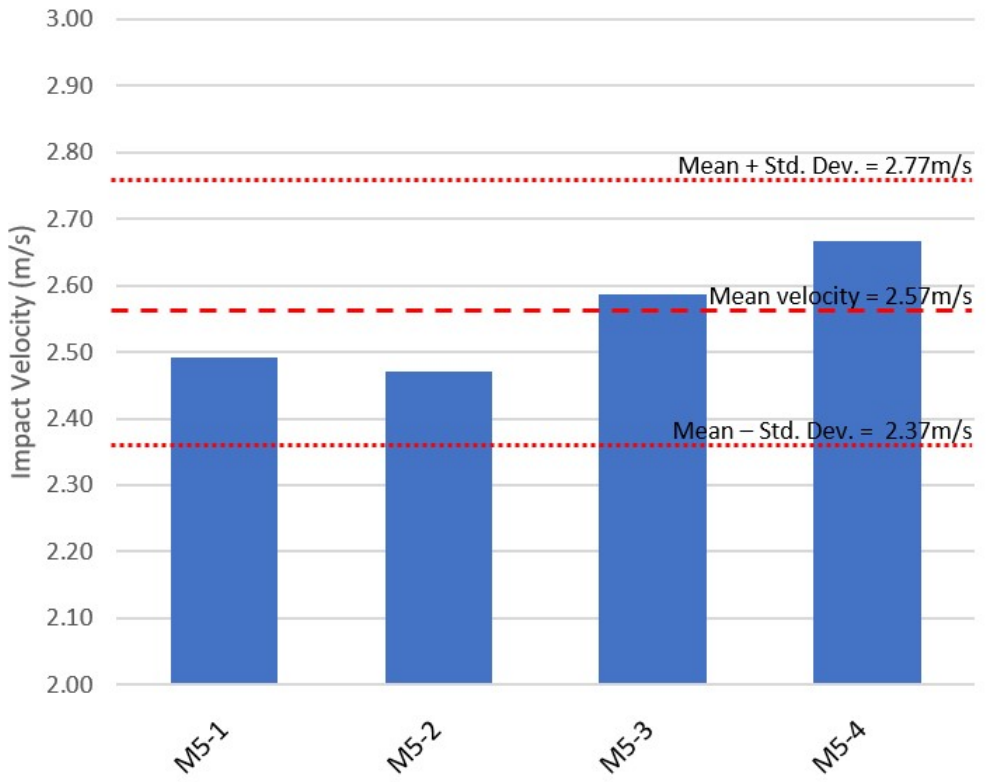

Figure 7-2: Simulation impact velocity data compared to experimental data

A visualization of the runout length data showing the mean and standard deviation values for the flume experimental data are shown in Figure 7-3 below.

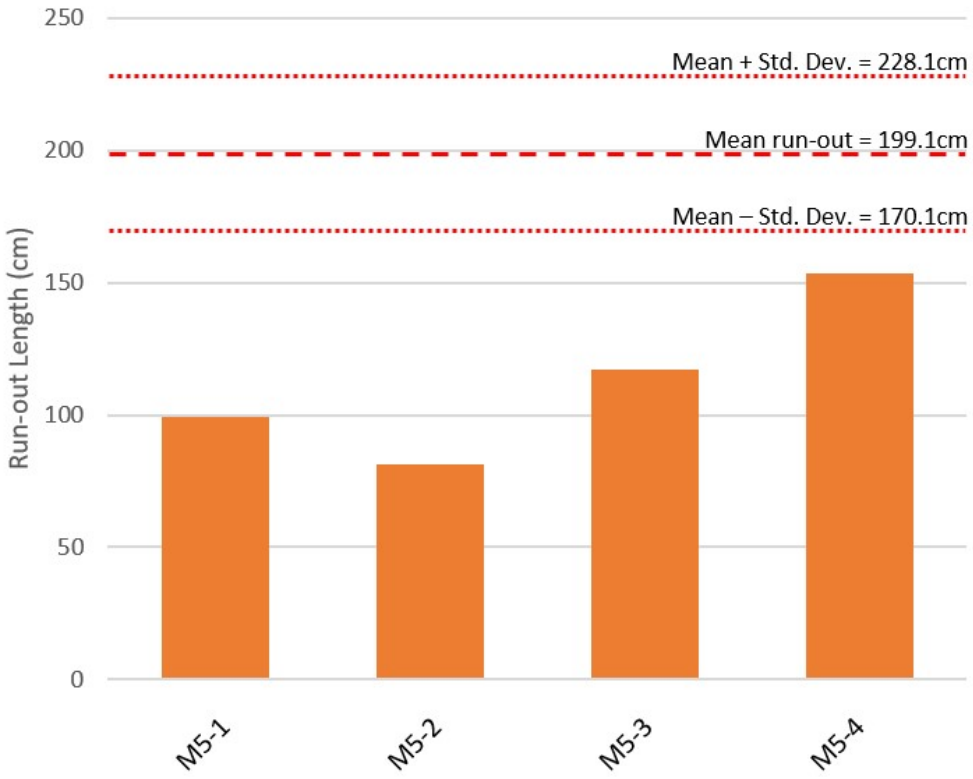

Figure 7-3: Simulation runout length data compared to experimental data

The final deposited flow volume and velocity contours at t = 8 seconds for each of the models are shown in Figure 7-4, Figure 7-5, Figure 7-6, and Figure 7-7 below.

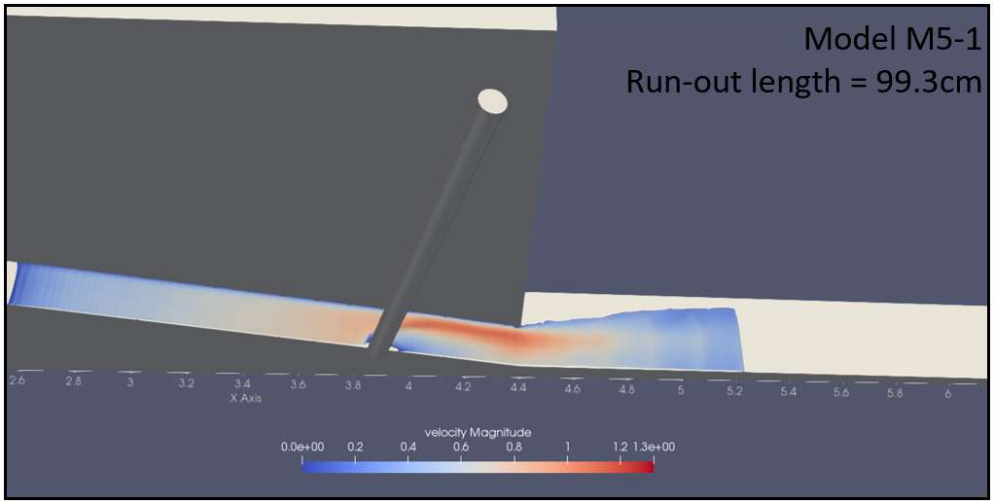

Figure 7-4: Model M5-1 runout geometry at t = 8 seconds

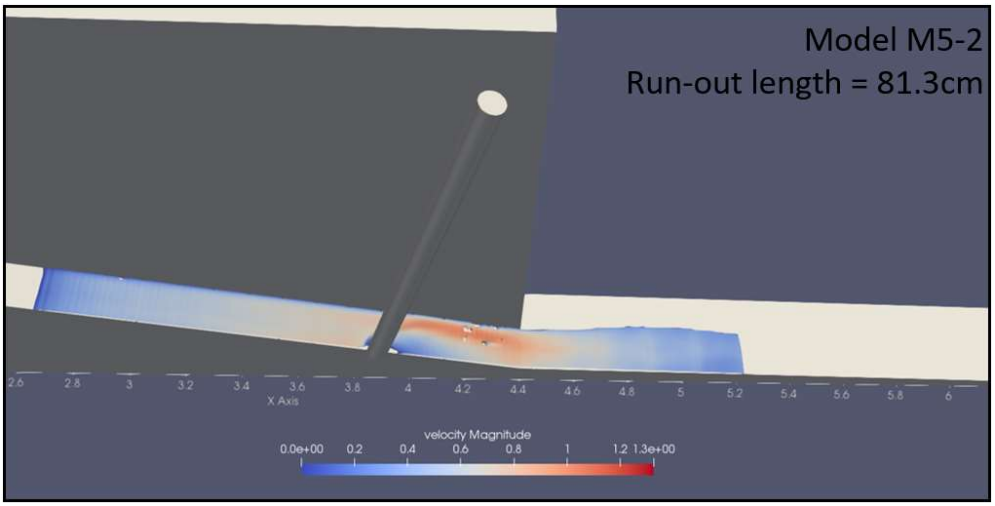

Figure 7-5: Model M5-2 runout geometry at t = 8 seconds

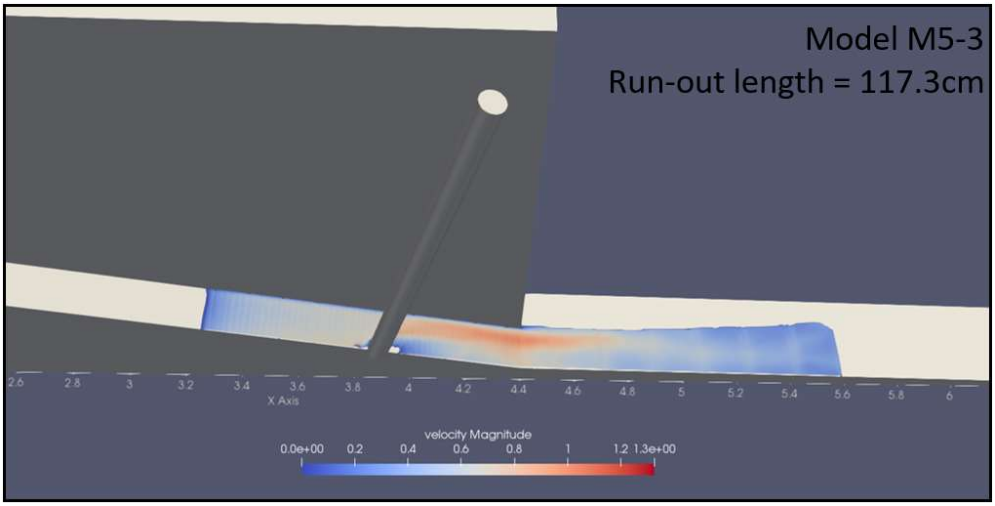

Figure 7-6: Model M5-3 runout geometry at t = 8 seconds

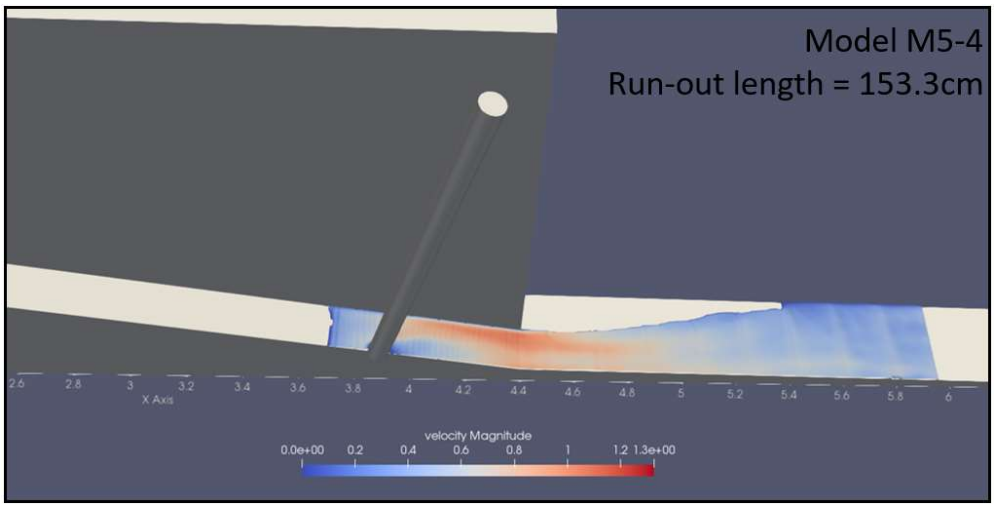

Figure 7-7: Model M5-4 runout geometry at t = 8 seconds

The upstream flow thickness for the M5 cases are presented in Figure 7-8 below.

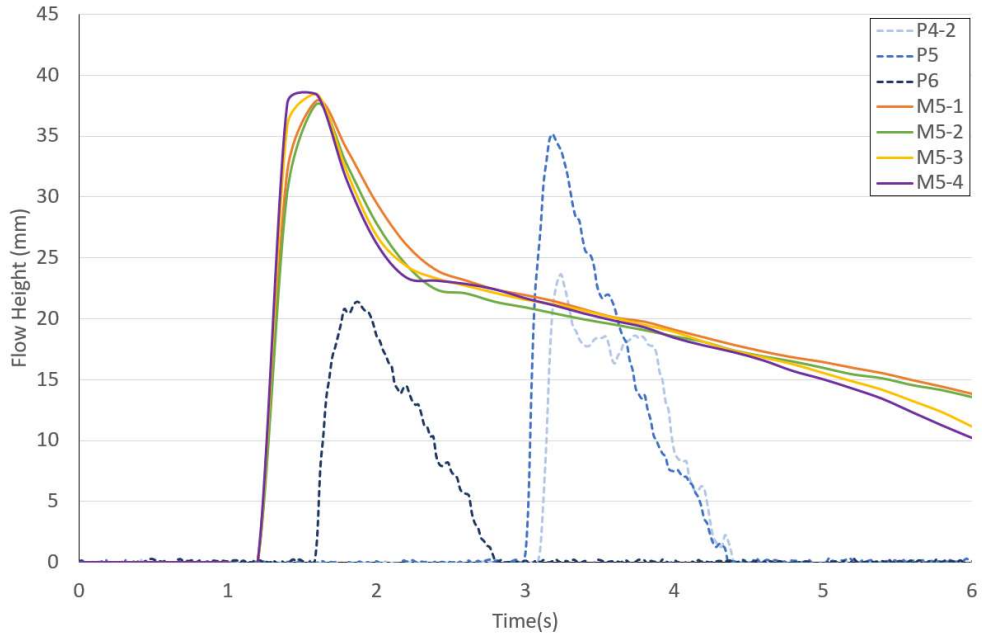

Figure 7-8: M5 - Upstream flow thickness

The downstream flow thickness for the M5 cases are presented in Figure 7-9 below.

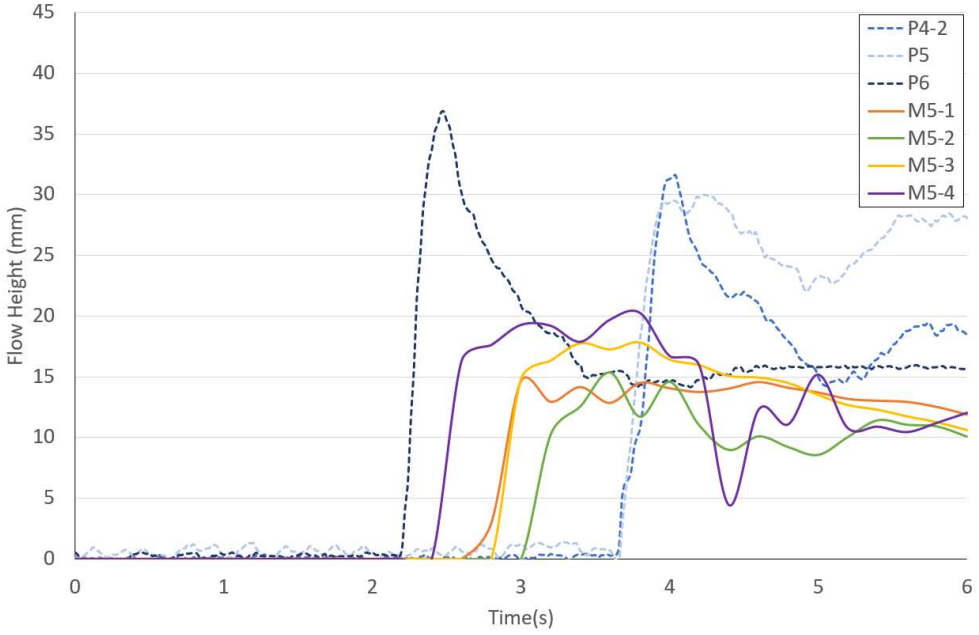

Figure 7-9: M5 - Downstream flow thickness

Pressure values were extracted from the cell nodes 1 cell distance (0.005m) in front of the cylindrical pillar (upstream side) to calculate an approximate resultant force provided by the rigid pillar. A surface integral is used to calculate the pillar force and is presented in Equation 19 below.

$$F_{pillar} = \iint_S p(r)\, dS \tag{19}$$

Where: F_{pillar} is the pillar force

$p(r)$ is the fluid node pressure acting on position vector r

S is the surface

Pillar resultant forces on the other side of the pillar were assumed to be relatively small compared to the force acting on the pillar front – and were ignored for the pillar force calculations.

The measured pillar force from the force transducer from the experimental data (P4-2, P5, P6) is shown along with the calculated pillar force from the empirical relationship proposed by Yifru et al. (2017) and the calculated pillar force based on the pressure data at the cell nodes in Figure 7-10 below.

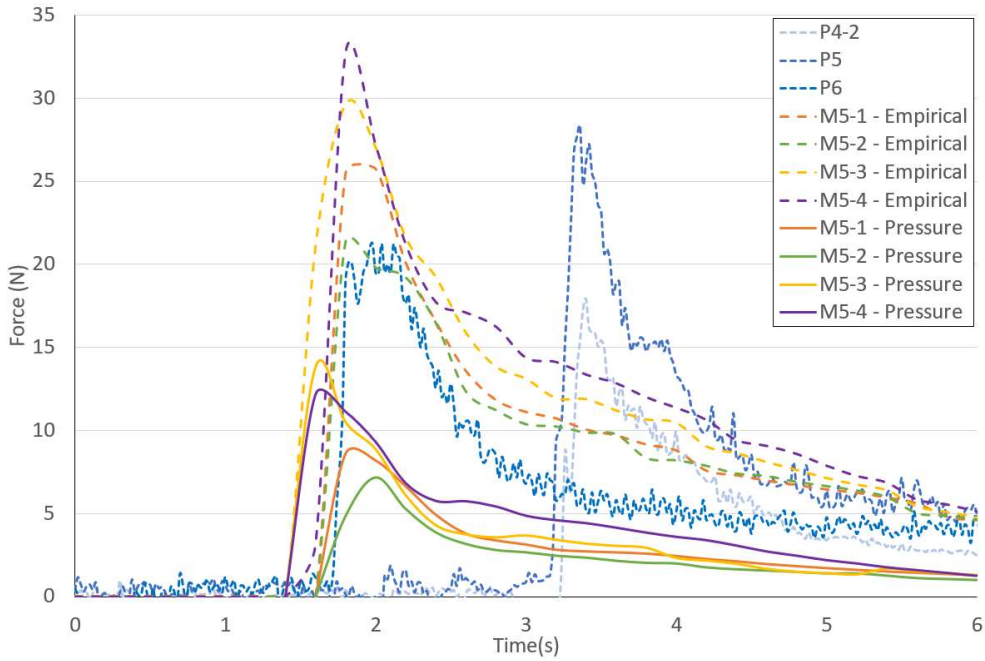

Figure 7-10: Force versus time for experimental and simulation data

The difference between the measured experimental values and the simulation values for models M5-1, M5-2, M5-3 and M5-4 are summarized in Table 7.3 below.

Table 7.3: Summary of simulation results for all models

Model	K [Pa·s^n]	n [-]	τ_y [Pa]	Peak Upstream Flow Thickness[1] (mm)	Peak Downstream Flow Thickness[1] (mm)	Impact Velocity[2] (m/s)	Run-out Length[2] (cm)	Peak Impact Force [Empirical][3] (N)	Peak Impact Force [Pressure][3] (N)
Flume	-			26.6	32.4	2.57	199	22.5	
M5-1	0.5	1.0	0.01	37.9	14.6	2.49	99.3	25.8	8.6
Difference (M5-1 - Flume)				*11.3*	*-17.8*	*-0.08*	*-99.7*	*3.3*	*-13.9*
M5-2	1.0	0.8	0.01	37.6	15.3	2.47	81.3	21.4	7.2
Difference (M5-2 - Flume)				*11.0*	*-17.1*	*-0.10*	*-117.7*	*-1.2*	*-15.3*
M5-3	0.3	1.0	0.01	38.4	17.8	2.59	117.3	29.7	13.8
Difference (M5-3 - Flume)				*11.8*	*-14.6*	*0.02*	*-81.7*	*7.2*	*-8.7*
M5-4	0.2	1.0	0.01	38.4	20.3	2.67	153.3	32.7	12.2
Difference (M5-4 - Flume)				*11.8*	*-12.1*	*0.10*	*-45.7*	*10.2*	*-10.3*

Notes:
1) Average flow thicknesses for "Flume" model are based on P4-2, P5, and P6 tests since experimental data showed that flow volume affected flow thickness.
2) Average Impact Velocity and Run-out Length for "Flume" model are based on all experimental data (9 tests) since there was no trend between flow volume and these measurements.
3) Impact force for "Flume" model is an average based on P4-2, P5, and P6 tests since the experimental data showed that flow volume affected impact force. Empirical impact force is based off of Yifru et al. (2017), and pressure impact force is based off of node data which is used to calculate the resultant force.

7.4 DISCUSSION

Flow velocities, for all the models (M5-1, M5-2, M5-3 and M5-4), at the pillar location (impact velocity) showed good calibration to the experimental data. Model M5-3 provided the best velocity match. Model M5-4 shows the flow at impact with the highest velocity, but the value is still within the mean value plus one standard deviation of the experimental tests.

Upstream flow thicknesses for the four numerical models showed similar behaviour – even considering the difference in rheological properties and subsequent kinematic viscosities. Similar results were shown in model M1, where reduction of kinematic viscosity had little affect at the upstream flow sensor. This behaviour appears to be starting geometry dependent. Although release points of the flow mass were matched, there is limitations on the starting geometry within the numerical software. The flume experiments also used a box where the mixing took place and the flow volume was released using a gate – this mechanism can not be modelled in the numerically. Figure 7-11 below shows the approximate difference in starting geometries for the numerical and physical modelling.

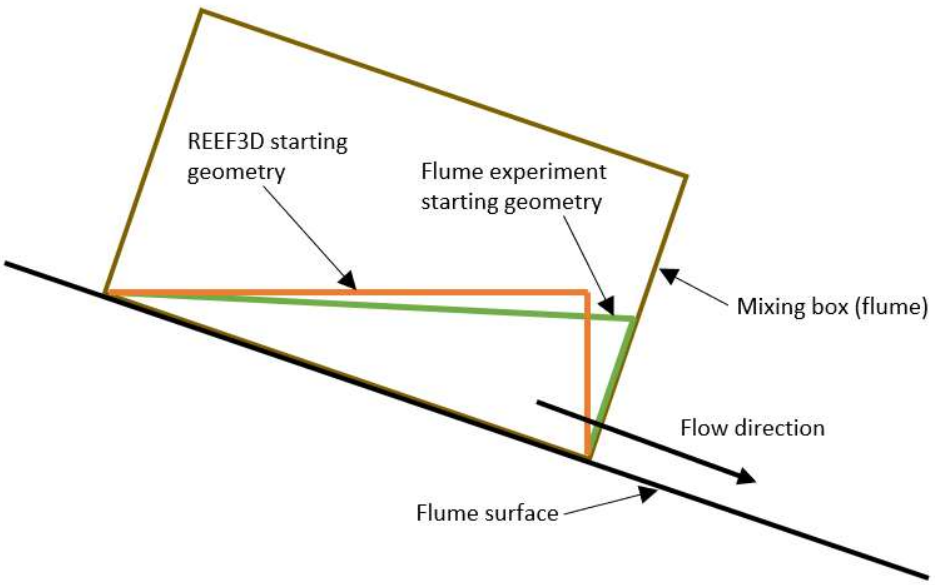

Figure 7-11: Difference in starting geometries for physical experiment and REEF3D modelling

The numerical models (M5-1, M5-2, M5-3 and M5-4) show approximately 10-12mm more upstream flow thickness at the peak value when compared to the average value from the experimental data (P4-2, P5 and P6).

The upstream flow sensors in the physical experiment record a surge of flow that completely passes the flow sensor within 1.5 seconds of the initial thickness measurement. Unlike the physical experiments, the numerical models show upstream flow thickness at the upstream sensor after the initial flow surge. A yield stress of 0.01Pa was used to attempt to fully mobilize the flow mass at the simulation start – but the flow mass does not move together like what was observed in the physical experiment. Most the flow mass in the REEF3D simulation is fully mobilized, but some material flows slower and shows a spreading behaviour from the starting geometry location. This behaviour is described in Bingham fluids by Liu and Mei (1989) who investigated the slow spreading of a Bingham fluid on an inclined plane. The tail of the free surface should continue to flatten and flow downstream over

time, but a singular surge is not created like the flume tests. The free surface approximation shows that the laboratory flow can be modelled well, but not perfectly using a non-Newtonian rheology. A more viscous material in the physical tests would match the numerical rheology behaviour better.

Figure 7-12 below shows the collapse of the initial flow geometry at simulation start – and the progression of the free surface at the material start location over the first second of the simulation. Most of the flow progresses down the flume, but there is a thin layer of approximately 10-15mm that spreads and shears at a lower rate.

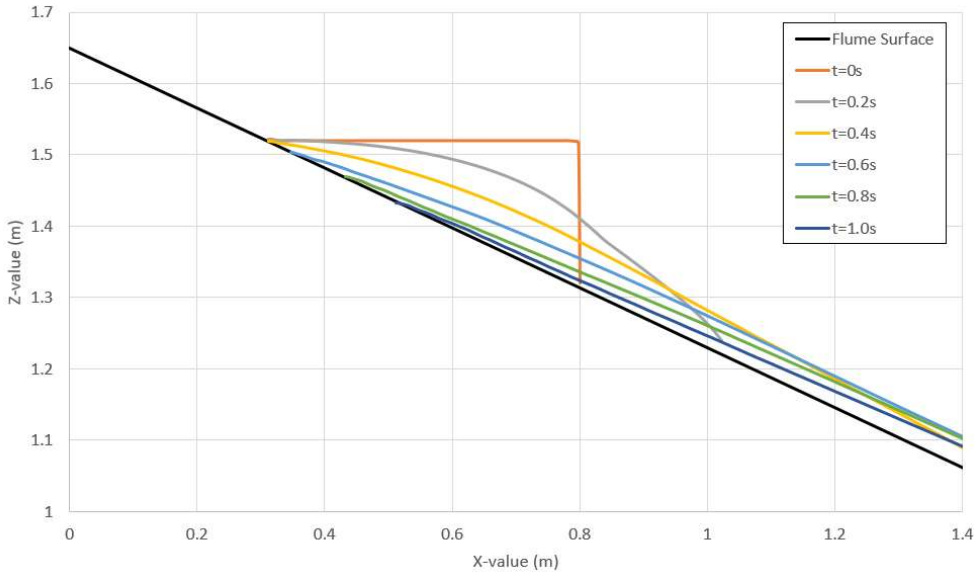

Figure 7-12: Free surface progression from t=0s to t=1.0s

This slower spreading of flow mass has an affect on all the following measurements – since not all the material is flowing down the flume together, like in the physical experiment, the momentum of the primary flow surge is reduced.

Downstream flow thickness in the M5 numerical model does not show a peak value reducing to a residual thickness value like the experimental data. Final

downstream flow thickness is approximately 10-15mm less then the values observed in the physical testing.

The impact force predicted by the empirical formula, proposed by Yifru et al. (2017) for the experimental flume, overpredicts force values based on the velocity and flow thicknesses in the numerical model. Although velocities are closely matched to the flume experiments, the flow thickness is approximately 10-20mm more – which increases the flow discharge (Q) used to calculate the force value. The force calculated from the pressure node data underpredicts the pillar force. The 0.2 second time step used in the numerical model likely can not capture the peak impact force well and the impact force would likely be higher if the pressures caused by the flow could be extracted from the pillar surface. For model M5-4, the empirical formula overpredicts the force by approximately 10N, and the pressure node data underpredicts by approximately the same amount.

The best calibration for runout length is shown by model M5-4 – but this model still shows approximately 23% less then the average runout length for all the experimental flume tests. There are large variations in runout length with the experimental flume tests, which likely shows inconsistencies with material homogeneity and laboratory procedures. Detailed deposition geometry of the experimental data was not provided to the author for analysis, but model M5-4 appears to show the best horizontal spreading match. Models M5-1, M5-2, and M5-3 do not spread horizontally in the deposition area as much as the experimental tests. Further reduction of the consistency parameter (K) or flow index (n) would reduce the kinematic viscosity and increase the runout length. But this would increase the impact velocity – potentially outside the range of observed values from the experimental data.

As mentioned previously, the timing data is hard to calibrate to because of video and instrumentation timing inconsistencies. The flume test P6 represents the best timing match between video and instrumentation data – and the model M5-4 closely matches the flow timing observed.

The best numerical model match is shown by the rheological parameters in model M5-4. The yield stress (τ_y) value of 0.01Pa is required to mobilize the flow mass instantaneously at the start of the simulation, and the consistency parameter (K) of 0.2 creates a flow that travels with similar velocity and behaviour. The flow index (n) is left at a value of 1, which models the flow mass as Bingham rheology behaviour. The impact velocity and upstream flow thickness show a good match to the experimental data. The downstream flow thickness and runout length are affected by the way the modelled non-Newtonian fluid behaves in its initial timing steps – creating a surge with less momentum then those observed in the experimental tests. The reduction in momentum has a larger influence on the runout length as less material is present in the primary surge, and the succeeding flow surges are slowed and stopped by the deposited material from the first surge.

The first 6 seconds of flow simulation, with 0.4 second time steps, for model M5-4 is shown in Appendix A. Detailed DiveMESH and REEF3D input files for models are provided in Appendix B and Appendix C respectively.

8 CONCLUSIONS

8.1 SUMMARY OF WORK COMPLETED

A detailed literature review on debris flow hazards was presented to introduce background information, including: classification, physical environment, climatic conditions, triggering events, behaviour, hazard analysis, and mitigation methods.

The results from the physical modelling that was performed at NTNU in 2017 was presented. The detailed database of results (upstream and downstream flow thicknesses, impact and residual forces, runout lengths) was used to guide numerical modelling of the debris flow tests. Numerical modelling using REEF3D was performed to model physical flume testing. Flows were simulated as a viscous single-phase fluid using Bingham and Herschel-Bulkley non-Newtonian fluid rheologies. The integration of these models and their applicability to debris flow modelling was reviewed.

A sensitivity study was performed to analyze the effect of rheological parameters and flume components on the flow behaviour. Reduction of rheological parameters (τ_y, K, n) creates faster, thinner flows. It was found that all the experimental flume components had a significant affect on the flow behaviour. Based on these findings, all the flume components were included in the final calibration, except a full width deposition area. The associated increase in cell count made the files to large to process in Paraview.

Calibration was performed on the final geometry to best match the experimental flume testing to the numerical modelling. It was found that to model the physical flume testing, a yield stress (τ_y) of 0.01Pa had to be used to mimic the liquefaction of the flow volume prior to release caused by the

hand-mixer. The consistency index (K) was reduced to a value of 0.2 while keeping the flow index (n) at 1.0 (modelling a Bingham flow) – which provided the best match to the experimental flume testing behaviour. Most of the debris flow behaviour observed in the laboratory can be modelled accurately using REEF3D and non-Newtonian fluid rheologies, but there are some limitations. The starting geometry could not be modelled the exact same as the experiment, and the initial material mobilization and primary surge magnitude does not follow the same behaviour as the flume experiment.

8.2 RECOMMENDATIONS FOR FURTHER WORK

Based on the results presented in the thesis, there is opportunity for further numerical modelling work to be performed. These include:

- Additional numerical modelling of more recent flume modelling at NTNU (2018) using REEF3D. Flow materials with higher % of fines and associated viscometer testing is available and the results from these flume tests could be modelled in REEF3D.
- Investigate alternative rheologies for flow materials that have a large granular portion and low fines content ($\mu(I)$ rheology).
- Analysis of the results produced from a simpler numerical modelling software (depth averaged shallow water equation-based software – ex. RAMMS) to the results produced from REEF3D.
- More rigorous calibration using a probabilistic framework: ex. Bayesian parameter estimation framework (Aaron, 2017).
- Investigate the free surface approximation for non-Newtonian fluids further to see if the thin layer travelling at a lower velocity is an interface or rheology effect.

- Integrate more complex starting geometries in REEF3D to better match the geometries encountered in the flume tests.

8.3 RECOMMENDATIONS FOR MODELLING WITH REEF3D

Future debris flow modelling with REEF3D numerical code should consider the following list of recommendations to reduce issues/downtime:

- The REEF3D numerical code is in early development, so bugs and numerical limitations are expected.
- A common issue encountered was disappearing free surface (and flow volume) – especially at low kinematic viscosities.
- Calibration without background viscometer testing is time consuming within the software due to time involved with computations, data file downloading from the HPC server, and post-processing – future modelling should use viscometer testing as base for calibration to reduce calibration time.
- Be aware of potential mesh issues that may be caused using “Solids” and “Objects” geometries – this behaviour seems to have been resolved with the latest releases.
- If numerically possible, attempt to model flow with 10+ cell thickness to get the most accurate internal behaviour.
- Use “wsfline” data (a section through the free surface) as a starting point to determine flow behaviour. Approximate velocities, flow thickness, and runout length can be determined from these data files and can give a general idea of flow behaviour. Because these data files are small, a print frequency of 0.01 or 0.02 seconds is recommended.

- Use “vtu” data for detailed velocity, flow thickness, and runout length data. Because these data files are large, a print frequency of 0.2 seconds (or greater) is recommended.
- Post-processing software Paraview has limitations with file size for “vtu” files – it was found that Paraview would crash when individual “vtu” file size exceeded approximately 15-20mb. File size is dependent on the total cells in the numerical models.
- If possible, attempt to get pillar surface pressure data in Paraview – this data will likely provide a more accurate representation of the impact force on the pillar then taking data 1-cell in front of the pillar.

9 LIST OF REFERENCES

Aaron, J. B. (2017). *Advancement and calibration of a 3D numerical model for landslide runout analysis.* (Text), Retrieved from https://open.library.ubc.ca/collections/24/items/1.0357191

Ancey, C. (2007). Plasticity and geophysical flows: A review. *Journal of Non-Newtonian Fluid Mechanics, 142*(1), 4-35. doi:https://doi.org/10.1016/j.jnnfm.2006.05.005

Anderson, J. D. (1995). *Computational fluid dynamics : the basics with applications*. New York: McGraw-Hill.

Bihs, H., Kamath, A., Alagan Chella, M., Aggarwal, A., & Arntsen, Ø. A. (2016). A new level set numerical wave tank with improved density interpolation for complex wave hydrodynamics. *Computers & Fluids, 140*(Supplement C), 191-208. doi:https://doi.org/10.1016/j.compfluid.2016.09.012

Bingham, E. C. (1916). *An investigation of the laws of plastic flow* (Vol. 13): US Bureau of Standards Bulletin.

Coussot, P. (1992). *Debris flow rheology - study of concentrated suspensions.* L'Institute National Polytechnique, Grenoble.

Coussot, P. (1994). Steady, laminar, flow of concentrated mud suspensions in open channel. *Journal of Hydraulic Research, 32*(4), 535-559. doi:10.1080/00221686.1994.9728354

Coussot, P., & Meunier, M. (1996). Recognition, classification and mechanical description of debris flows. *Earth-Science Reviews, 40*(3), 209-227. doi:10.1016/0012-8252(95)00065-8

Fornes, P., Bihs, H., Thakur, V., & Nordal, S. (2017). *Implementation of non-Newtonian rheology for debris flow simulation with REEF3D.* Paper presented at the 37th IAHR World Congress, Kuala Lumpur, Malaysia.

Guthrie, R., Hockin, A., Colquhoun, L., Nagy, T., Evans, S., & Ayles, C. (2010). *An examination of controls on debris flow mobility: Evidence from coastal British Columbia* (Vol. 114).

Herschel, W. H., & Bulkley, R. (1926). Konsistenzmessungen von gummi-benzollösungen. *Colloid & Polymer Science, 39*(4), 291-300.

Hübl, J., Fiebiger, G., Jakob, M., & Hungr, O. (2005). *Debris-flow mitigation measures*.

Hungr, O. (1995). A model for the runout analysis of rapid flow slides, debris flows, and avalanches. *Canadian Geotechnical Journal, 32*(4), 610-623. doi:10.1139/t95-063

Hungr, O. (2005). Classification and terminology. In *Debris-flow hazards and related phenomena* (pp. 9-23). Berlin, Heidelberg: Springer Berlin Heidelberg.

Hungr, O. (2009). Numerical modelling of the motion of rapid, flow-like landslides for hazard assessment. *KSCE Journal of Civil Engineering, 13*(4), 281-287. doi:10.1007/s12205-009-0281-7

Hungr, O., Leroueil, S., & Picarelli, L. (2014). The Varnes classification of landslide types, an update. *Landslides, 11*(2), 167-194. doi:10.1007/s10346-013-0436-y

Hungr, O., McDougall, S., & Bovis, M. (2005). Entrainment of material by debris flows. In *Debris-flow hazards and related phenomena* (pp. 135-158). Berlin, Heidelberg: Springer Berlin Heidelberg.

Hungr, O., Morgan, G. C., & Kellerhals, R. (1984). Quantitative analysis of debris torrent hazards for design of remedial measures. *Canadian Geotechnical Journal, 21*(4), 663-677. doi:10.1139/t84-073

Iverson, R. M. (1993). Differential equations governing slip-induced pore-pressure fluctuations in a water-saturated granular medium. *Mathematical Geology, 25*(8), 1027-1048. doi:10.1007/bf00911548

Iverson, R. M. (1997). The physics of debris flows. *Reviews of Geophysics, 35*(3), 245-296. doi:10.1029/97RG00426

Iverson, R. M. (2003). *The debris-flow rheology myth* (Vol. 1).

Iverson, R. M. (2005). Debris-flow mechanics. In *Debris-flow hazards and related phenomena* (pp. 105-134). Berlin, Heidelberg: Springer Berlin Heidelberg.

Iverson, R. M., Reid, M. E., & Lahusen, R. (1997). *Debris-Flow Mobilization from Landslides* (Vol. 25).

Iverson, R. M., Reid, M. E., Logan, M., LaHusen, R. G., Godt, J. W., & Griswold, J. P. (2010). Positive feedback and momentum growth during debris-flow entrainment of wet bed sediment. *4*, 116. doi:10.1038/ngeo1040

https://www.nature.com/articles/ngeo1040#supplementary-information

Jakob, M. (2005). Debris-flow hazard analysis. In *Debris-flow hazards and related phenomena* (pp. 411-443). Berlin, Heidelberg: Springer Berlin Heidelberg.

Jakob, M., Stein, D., & Ulmi, M. (2012). Vulnerability of buildings to debris flow impact. *Natural Hazards, 60*(2), 241-261. doi:10.1007/s11069-011-0007-2

Jiang, G.-S., & Peng, D. (2000). Weighted ENO Schemes for Hamilton--Jacobi Equations. *SIAM Journal on Scientific Computing, 21*(6), 2126-2143. doi:10.1137/S106482759732455X

Jiang, G.-S., & Shu, C.-W. (1996). Efficient implementation of weighted ENO schemes. *Journal of Computational Physics, 126*(1), 202-228. doi:10.1006/jcph.1996.0130

Johnson, R. W. (2016). *Handbook of fluid dynamics*. In R. W. Johnson (Ed.).

Johnson, S. W., Lee, D. G., Pyrz, A. P., & Thompson, J. E. (1970). Simulating the effects of gravitational field and atmosphere on behavior of granular media. *Journal of Spacecraft and Rockets, 7*(11), 1311-1317. doi:10.2514/3.30163

Kaitna, R., Rickenmann, D., & Schatzmann, M. (2007). Experimental study on rheologic behaviour of debris flow material. *Acta Geotechnica, 2*(2), 71-85. doi:10.1007/s11440-007-0026-z

Körner, H. J. (1976). Reichweite und Geschwindigkeit von Bergstürzen und Fließschneelawinen. *Rock mechanics, 8*(4), 225-256.

Liu, K. F., & Mei, C. C. (1989). Slow spreading of a sheet of Bingham fluid on an inclined plane. *Journal of Fluid Mechanics, 207*, 505-529. doi:10.1017/S0022112089002685

Lorenzini, G., & Mazza, N. (2004). *Debris Flow: Phenomenology and Rheological Modelling*: WIT Press.

Major, J., & Pierson, T. (1992). *Debris Flow Rheology: Experimental Analysis of Fine-Grained Slurries* (Vol. 28).

McDougall, S. (2016). 2014 Canadian Geotechnical Colloquium: Landslide runout analysis — current practice and challenges. *Canadian Geotechnical Journal, 54*(5), 605-620. doi:10.1139/cgj-2016-0104

Moriguchi, S., Borja, R. I., Yashima, A., & Sawada, K. (2009). Estimating the impact force generated by granular flow on a rigid obstruction. *Acta Geotechnica, 4*(1), 57-71. doi:10.1007/s11440-009-0084-5

Murgang am Glyssibach, Brienz. (2005, December 12, 2017). Retrieved from http://www.planat.ch/en/images-details/datum/2011/06/22/murgaenge-brienz-2005/

Osher, S., & Sethian, J. A. (1988). Fronts propagating with curvature-dependent speed: Algorithms based on Hamilton-Jacobi formulations. *Journal of Computational Physics, 79*(1), 12-49. doi:https://doi.org/10.1016/0021-9991(88)90002-2

Pierson, T. C., & Costa, J. E. (1987). A rheologic classification of subaerial sediment-water flows. *Debris flows/avalanches*, 1-12.

Rickenmann, D. (2005). Runout prediction methods. *Debris-flow hazards and related phenomena*, 305-324.

Sassa, K., & Wang, G. h. (2005). Mechanism of landslide-triggered debris flows: Liquefaction phenomena due to the undrained loading of torrent deposits. In *Debris-flow hazards and related phenomena* (pp. 81-104). Berlin, Heidelberg: Springer Berlin Heidelberg.

Savage, S. B., & Hutter, K. (1989). The motion of a finite mass of granular material down a rough incline. *Journal of Fluid Mechanics, 199*, 177-215. doi:10.1017/S0022112089000340

Shu, C.-W., & Osher, S. (1988). Efficient implementation of essentially non-oscillatory shock-capturing schemes. *Journal of Computational Physics, 77*(2), 439-471. doi:10.1016/0021-9991(88)90177-5

Takahashi, T. (1981). Debris Flow. *Annual Review of Fluid Mechanics, 13*(1), 57-77. doi:10.1146/annurev.fl.13.010181.000421

Takahashi, T. (2014). What is debris flow? In *Debris Flow: Mechanics, Prediction and Countermeasures, 2nd edition* (pp. 1-36): CRC Press.

VanDine, D. F. (1985). Debris flows and debris torrents in the Southern Canadian Cordillera. *Canadian Geotechnical Journal, 22*(1), 44-68. doi:10.1139/t85-006

Voellmy, A. (1955). Uber die zerstorungskraft von lawinen. *Bauzeitung, 73*, 159-165.

Whipple, K. X. (1997). Open-channel flow of Bingham fluids: Applications in debris-flow research. *Journal of Geology, 105*(2), 243.

Wieczorek, G. F., & Glade, T. (2005). Climatic factors influencing occurrence of debris flows. In *Debris-flow hazards and related phenomena* (pp. 325-362). Berlin, Heidelberg: Springer Berlin Heidelberg.

Yifru, A. L., Pradhan, R. N., Thakur, V., & Nordal, S. (2017). *Preliminary study of debris flow impact force on a circular pillar*.

APPENDIX A: M5-4 FLOW SIMULATION

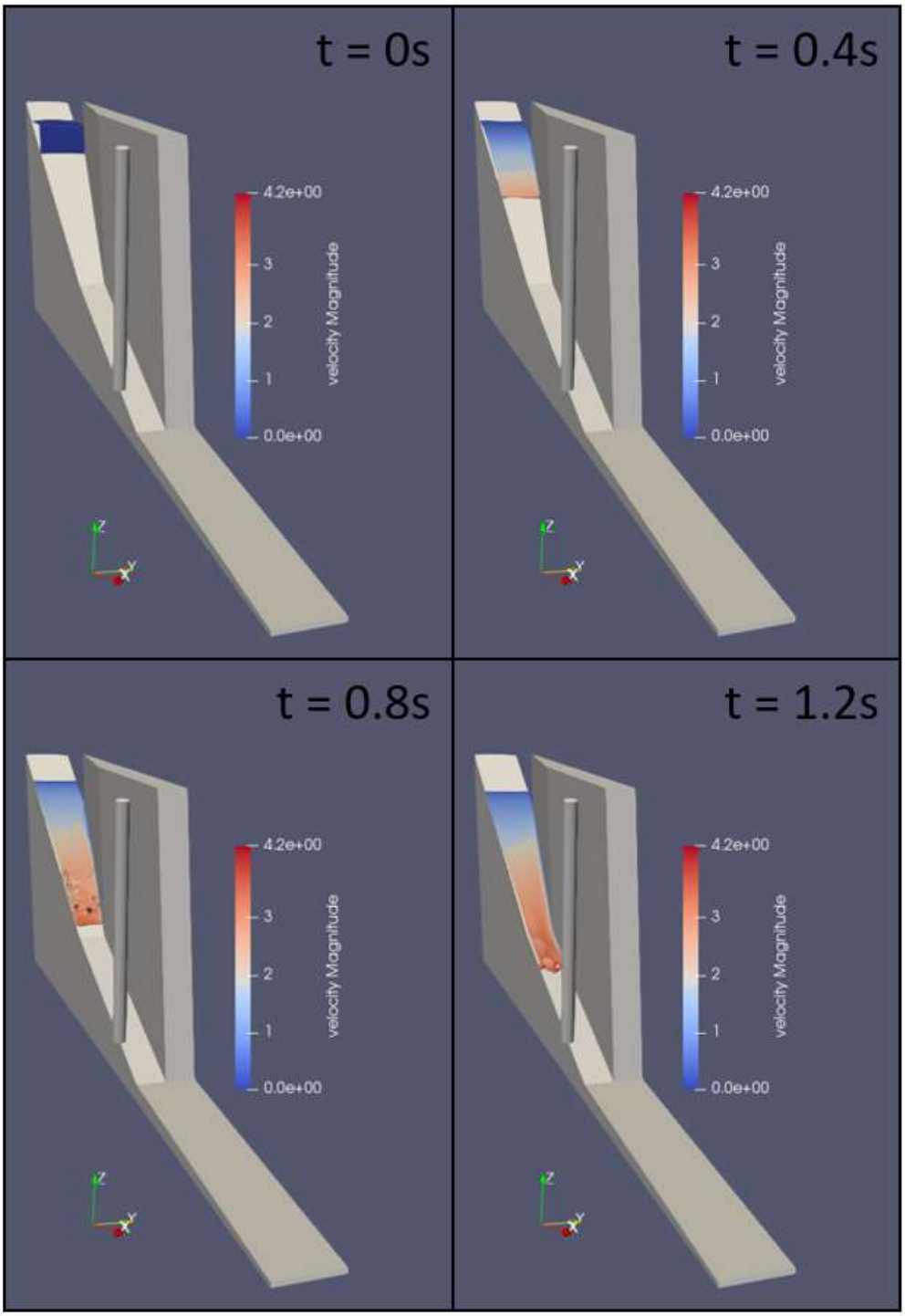
t = 0s
4.2e+00
3
2
1
0.0e+00
velocity Magnitude
t = 0.4s
4.2e+00
3
2
1
0.0e+00
velocity Magnitude
t = 0.8s
4.2e+00
3
2
1
0.0e+00
velocity Magnitude
t = 1.2s
4.2e+00
3
2
1
0.0e+00
velocity Magnitude

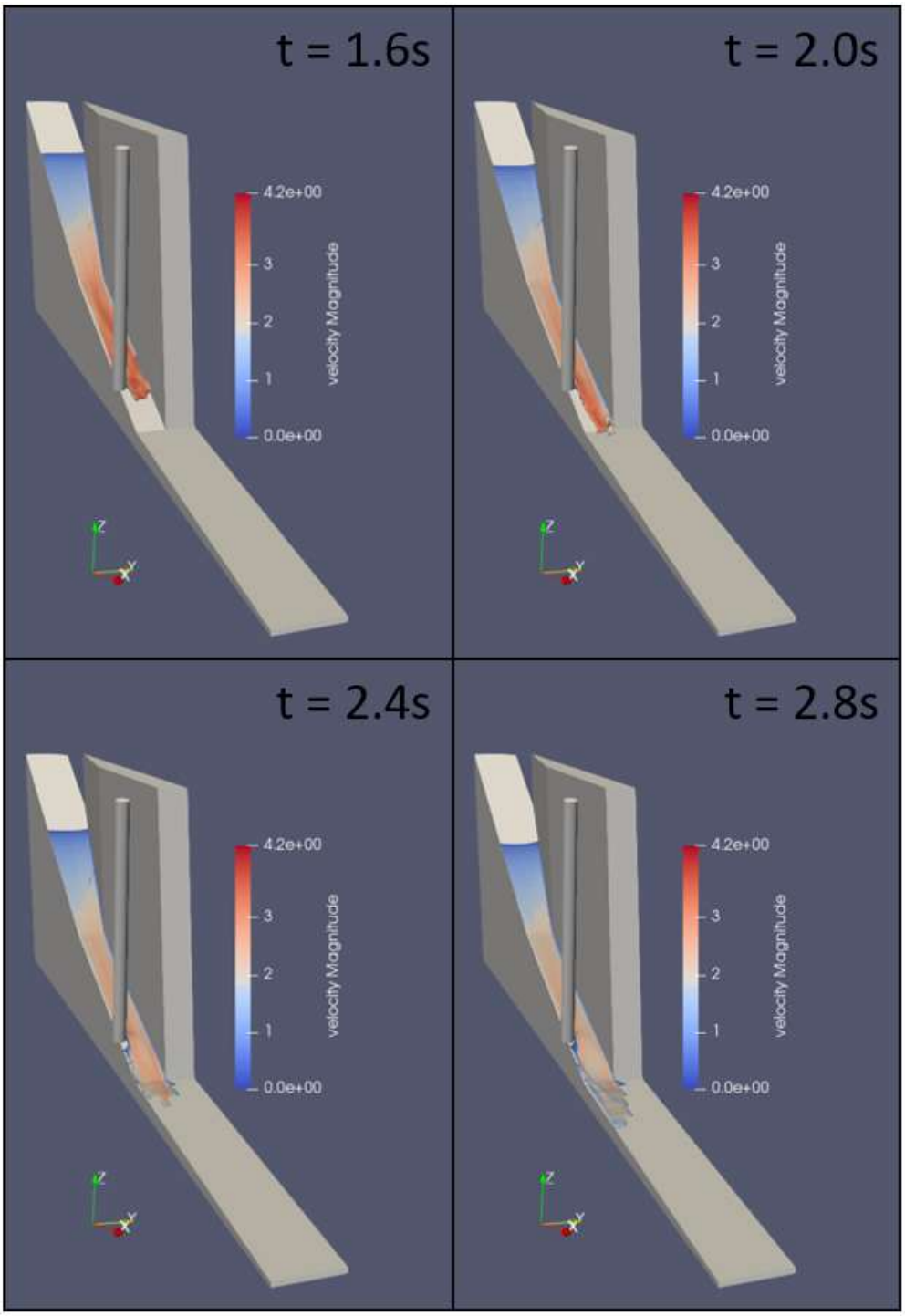
t = 1.6s
4.2e+00
3
2
1
0.0e+00
velocity Magnitude
t = 2.0s
4.2e+00
3
2
1
0.0e+00
velocity Magnitude
t = 2.4s
4.2e+00
3
2
1
0.0e+00
velocity Magnitude
t = 2.8s
4.2e+00
3
2
1
0.0e+00
velocity Magnitude

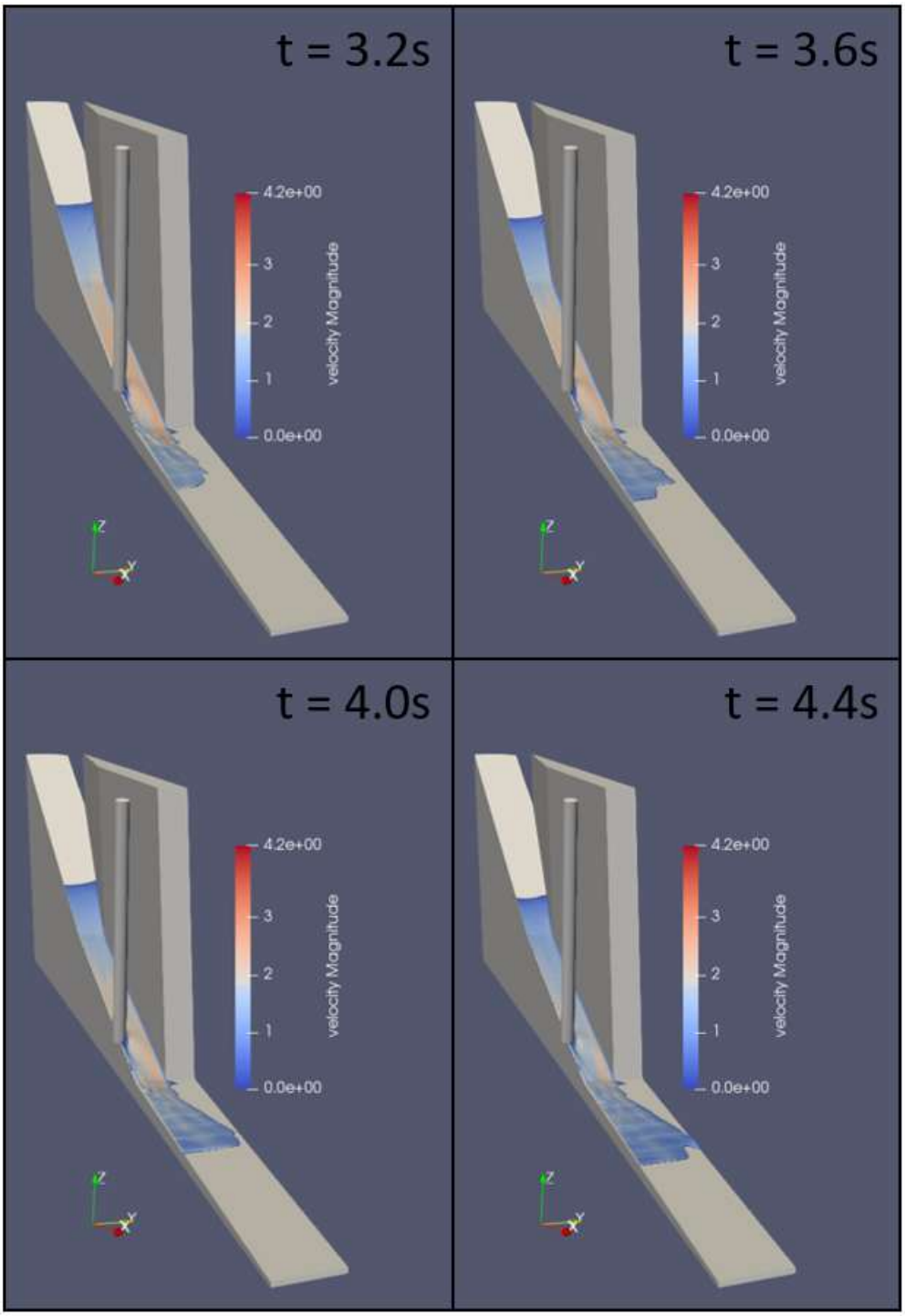
t = 3.2s
4.2e+00
3
2
1
0.0e+00
velocity Magnitude
t = 3.6s
4.2e+00
3
2
1
0.0e+00
velocity Magnitude
t = 4.0s
4.2e+00
3
2
1
0.0e+00
velocity Magnitude
t = 4.4s
4.2e+00
3
2
1
0.0e+00
velocity Magnitude

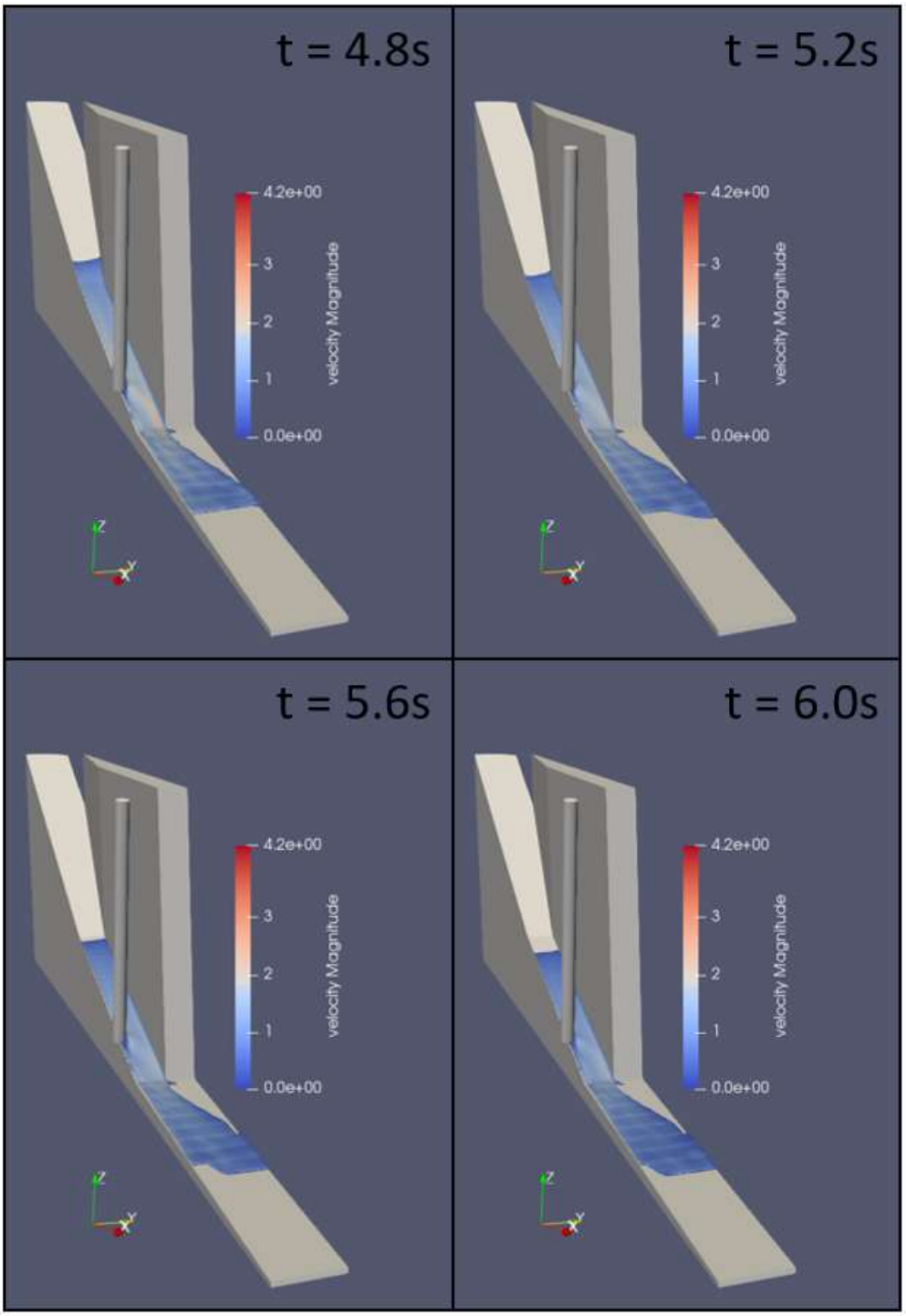
t = 4.8s
4.2e+00
3
2
1
0.0e+00
velocity Magnitude
t = 5.2s
4.2e+00
3
2
1
0.0e+00
velocity Magnitude
t = 5.6s
4.2e+00
3
2
1
0.0e+00
velocity Magnitude
t = 6.0s
4.2e+00
3
2
1
0.0e+00
velocity Magnitude

APPENDIX B: INPUT CODE FOR DIVEMESH MODELS

MODEL M1

```
C 11 21
C 12 21
C 13 3
C 14 21
C 15 21
C 16 21

B 1 0.005
B 10 0.0 8.0 0.0 0.15 0.0 1.7
S 10 0.0 2.5 0 0.15 0.0 0.60
S 10 2.5 4.4 0 0.15 0.0 0.10
S 61 0.0 2.5 0 0.15 1.65 0.60
S 61 2.5 4.4 0 0.15 0.60 0.10
S 61 4.4 8.0 0.0 0.15 0.10 0.0

M 10 256
M 20 1
```

MODEL M2

```
C 11 21
C 12 21
C 13 3
C 14 21
C 15 21
C 16 21

B 1 0.005
B 10 0.0 4.4 0.0 0.30 0.0 1.7
S 84 0.8 0.30 0.0 2.5 0.15 0.0 4.4 0.15 0.0 4.4 0.30 0.0
0.8 0.30 1.70 2.5 0.15 1.70 4.4 0.30 1.70 4.4 0.30 1.70
S 84 2.5 0.15 0.0 4.4 0.15 0.0 4.4 0.30 0.0 2.5 0.30 0.0
2.5 0.15 1.70 4.4 0.15 1.70 4.4 0.30 1.70 2.5 0.30 1.70
S 84 0.0 0.0 0.0 0.8 0.0 0.0 0.8 0.3 0.0 0.0 0.3 0.0 0.0
0.0 1.65 0.8 0.0 1.31 0.8 0.3 1.31 0.0 0.3 1.65
S 84 0.8 0.0 0.0 2.5 0.0 0.0 2.5 0.15 0.0 0.8 0.3 0.0
0.8 0.0 1.31 2.5 0.0 0.6 2.5 0.15 0.6 0.8 0.3 1.31
S 84 2.5 0.0 0.0 4.4 0.0 0.0 4.4 0.15 0.0 2.5 0.15 0.0
2.5 0.0 0.6 4.4 0.0 0.1 4.4 0.15 0.1 2.5 0.15 0.6

M 10 256
M 20 1
```

MODEL M3

```
C 11 21
C 12 21
C 13 3
C 14 21
C 15 21
C 16 21

B 1 0.005
B 10 0.0 8.0 0.0 0.15 0.0 1.7
S 10 0.0 2.5 0 0.15 0.0 0.60
S 10 2.5 4.4 0 0.15 0.0 0.10
S 37 3.9 0 0.23 0.035 4.255 0 1.625 0.035
S 61 0.0 2.5 0 0.15 1.65 0.60
S 61 2.5 4.4 0 0.15 0.60 0.10
S 61 4.4 8.0 0.0 0.15 0.10 0.0

M 10 256
M 20 1
```

MODEL M4

```
C 11 21
C 12 21
C 13 3
C 14 21
C 15 21
C 16 21

B 1 0.005
B 10 0.0 6.2 0.0 0.60 0.0 1.7
S 10 0.0 4.4 0.15 0.60 0.0 1.7
S 10 0.0 2.5 0 0.15 0.0 0.60
S 10 2.5 4.4 0 0.15 0.0 0.10
S 61 0.0 2.5 0 0.15 1.65 0.60
S 61 2.5 4.4 0 0.15 0.60 0.10
S 84 4.4 0.0 0.0 6.2 0.0 0.0 6.2 0.30 0.0 4.4 0.30 0.0
4.4 0.0 0.1 6.2 0.0 0.05 6.2 0.30 0.05 4.4 0.30 0.1

M 10 256
M 20 1
```

MODEL M5

```
C 11 21
C 12 21
C 13 3
C 14 21
C 15 21
C 16 21

B 1 0.005
B 10 0.0 7.1 0.0 0.30 0.0 1.7
S 10 2.5 4.4 0.15 0.30 0.0 1.7
S 37 3.9 0 0.23 0.035 4.255 0 1.625 0.035
S 61 4.4 7.1 0.0 0.30 0.10 0.025
S 83 0.8 0.30 0.0 2.5 0.15 0.0 2.5 0.30 0.0 0.8 0.30
1.70 2.5 0.15 1.70 2.5 0.30 1.70
S 84 0.0 0.0 0.0 0.8 0.0 0.0 0.8 0.3 0.0 0.0 0.3 0.0 0.0
0.0 1.65 0.8 0.0 1.31 0.8 0.3 1.31 0.0 0.3 1.65
S 84 0.8 0.0 0.0 2.5 0.0 0.0 2.5 0.15 0.0 0.8 0.3 0.0
0.8 0.0 1.31 2.5 0.0 0.6 2.5 0.15 0.6 0.8 0.3 1.31
S 84 2.5 0.0 0.0 4.4 0.0 0.0 4.4 0.15 0.0 2.5 0.15 0.0
2.5 0.0 0.6 4.4 0.0 0.1 4.4 0.15 0.1 2.5 0.15 0.6

M 10 256
M 20 1
```

APPENDIX C: INPUT CODE FOR REEF3D MODELS (M5 MODELS ONLY)

MODEL M5-1

```
D 10 4
D 20 2
D 30 1
F 30 3
F 40 3
F 50 4
F 52 0
F 53 1.31
F 54 0.8
F 55 0.3
F 56 1.52
I 12 1
N 10 14
N 11 11
N 40 6
N 41 8.0
N 45 90000
N 47 0.1
M 10 256
P 10 1
P 30 0.2
P 52 0.005
P 55 0.02
P 71 1
T 10 0
W 1 1957
W 2 0.001
W 22 -9.81
W 90 1
W 95 1000
W 96 0.01
W 97 0.5
W 98 1.0
```

MODEL M5-2

```
D 10 4
D 20 2
D 30 1
F 30 3
F 40 3
F 50 4
F 52 0
F 53 1.31
F 54 0.8
F 55 0.3
F 56 1.52
I 12 1
N 10 14
N 11 11
N 40 6
N 41 8.0
N 45 90000
N 47 0.1
M 10 256
P 10 1
P 30 0.2
P 52 0.005
P 55 0.02
P 71 1
T 10 0
W 1 1957
W 2 0.001
W 22 -9.81
W 90 1
W 95 1000
W 96 0.01
W 97 1.0
W 98 0.8
```

MODEL M5-3

```
D 10 4
D 20 2
D 30 1
F 30 3
F 40 3
F 50 4
F 52 0
F 53 1.31
F 54 0.8
F 55 0.3
F 56 1.52
I 12 1
N 10 14
N 11 11
N 40 6
N 41 8.0
N 45 90000
N 47 0.1
M 10 256
P 10 1
P 30 0.2
P 52 0.005
P 55 0.02
P 71 1
T 10 0
W 1 1957
W 2 0.001
W 22 -9.81
W 90 1
W 95 1000
W 96 0.01
W 97 0.3
W 98 1.0
```

MODEL M5-4

```
D 10 4
D 20 2
D 30 1
F 30 3
F 40 3
F 50 4
F 52 0
F 53 1.31
F 54 0.8
F 55 0.3
F 56 1.52
I 12 1
N 10 14
N 11 11
N 40 6
N 41 8.0
N 45 90000
N 47 0.3
M 10 256
P 10 1
P 30 0.2
P 52 0.005
P 55 0.02
P 71 1
T 10 0
W 1 1957
W 2 0.001
W 22 -9.81
W 90 1
W 95 1000
W 96 0.01
W 97 0.2
W 98 1.0
```